ABSTRACT

Title of Document: INHIBITION OF LAMINAR PREMIXED FLAMES BY HALON 1301 ALTERNATIVES

John L. Pagliaro, Doctor of Philosophy, 2015

Directed By: Associate Professor Peter Sunderland
Department of Fire Protection Engineering

Halon 1301 (CF_3Br) has been banned (by the Montreal Protocol) because of its ozone depleting potential. Even though a critical-use exemption of CF_3Br has been granted for commercial aircraft cargo bay applications, the European Union is requiring replacement in new aircraft by 2018 and in existing aircraft by 2040. As a result of the expected phase-out, the FAA tested three alternatives (C_2HF_5, $C_3H_2F_3Br$, and $C_6F_{12}O$) in a cargo bay simulator, and under certain conditions, apparent combustion enhancement was observed (even though the agents showed promise in standard tests). To understand the enhancement, experiments and numerical analysis are performed to: 1) test the concepts developed via previous numerical simulations and analysis of the FAA tests, 2) reproduce the phenomena observed in the complex full-scale FAA experiments in laboratory-scale experiments which might serve as a screening tool, 3) provide preliminary validation of recently developed kinetic

mechanisms (which are used to understand the phenomena), and 4) examine the performance of potential replacements that were not tested by the FAA.

Two spherically expanding flame experiments were built to measure laminar burning velocity, peak pressure rise, and flame response to stretch. For each experiment, developments included designing the chamber, creating the operating procedure, setting up the necessary data acquisition and operation controls, and developing data reduction and post-processing routines. Numerical modeling with detailed kinetics was performed to interpret experimental results and to validate kinetic mechanisms. The most significant findings of this study include the enhancement of lean CH_4-air flames by the proposed alternative agents, the potential of HCFC-123 as a halon replacement, and excellent agreement between burning velocity predictions (with detailed chemical mechanisms) and measurements for hydrocarbon-air flames inhibited by CF_3Br, C_2HF_5, $C_3H_2F_3Br$, $C_6F_{12}O$, and $C_2HF_3Cl_2$.

INHIBITION OF LAMINAR PREMIXED FLAMES BY HALON 1301 ALTERNATIVES

By

John L. Pagliaro

Dissertation submitted to the Faculty of the Graduate School of the
University of Maryland, College Park, in partial fulfillment
of the requirements for the degree of
Doctor of Philosophy
2015

Advisory Committee:
Associate Professor Peter Sunderland, Chair
Professor Michael Zachariah, Dean's Representative
Professor Marino diMarzo
Assistant Professor Stanislav Stoliarov
Dr. Gregory Linteris

Acknowledgements

This work was supported by a NIST-ARRA fellowship, the Boeing Company, and teaching assistantships granted by the Fire Protection Engineering and Keystone Engineering departments at the University of Maryland.

Thanks to my fiancé, family, advisors, colleagues, and friends who have provided tremendous support during the preparation of this document and during my time as a graduate student at UMD. Without them I would not have been able to start/finish the journey required to earn a Ph.D. degree in engineering.

In particular, thanks to my academic advisor, Peter Sunderland, and my research advisor, Greg Linteris. It has been the utmost privilege to work with, and learn from them. I think a student would be fortunate to have either as an advisor, and I frequently wonder how I became so lucky as to be advised by both of them. Thanks to Valeri Babushok, with whom I shared an office with, and Nicolas Bouvet, with whom I shared a lab with at NIST. They were invaluable sources of information regarding halogenated flame chemistry and laminar flame speed measurements. Lastly, thanks to everyone in the fire protection and mechanical engineering departments at UMD and in the fire research division at NIST.

Table of Contents

List of Tables

List of Figures

Nomenclature

Physical Constants

R_u – Ideal gas constant

Roman Symbols

A – Pre-exponential factor

A_f – Flame surface area

C – Capacitance

e – Specific internal energy

E – Stored energy

E_a – Activation energy

k – Kinetic rate coefficient

k_c – Coverage factor

K – Stretch rate

L_b – Markstein length

Le – Lewis number

M – Mass

P – Pressure

R – Chamber radius

R_f – Flame radius

S_u – Unburned gas velocity

S_u^0 – Unstretched burning velocity

S_b – Burned gas velocity

t – Time

T - Temperature

u_c – Standard deviation

V – Volume

v – Voltage

X_a – Agent volume fraction

y_b – Mass fraction of burned gas

Greek Symbols

ν – Specific volume

γ – Specific heat ratio

Φ – Equivalence ratio

ρ - Density

Chapter 1: Introduction

1.1 Motivation

Halon 1301 (CF_3Br) is an effective fire suppressant, but has been banned by the Montreal Protocol [1] because of its high ozone depletion potential (ODP). A critical-use exemption of recycled CF_3Br has been granted for aircraft crew compartments, engine nacelles, cargo bays, dry bays, and fuel tanks [2]. Nonetheless, the European Union is requiring replacement of CF_3Br in newly constructed aircraft by 2018 and in existing aircraft by 2040. This study aims to aid in the search for a suitable replacement.

As a result of the expected phase-out, the Federal Aviation Administration (FAA) developed a minimum performance standard [3] to screen new low ODP replacements for use in cargo bays. Four fire scenarios were established to compare the suppression effectiveness of new alternatives to that of CF_3Br: the bulk-load fire, the containerized fire, the surface burning fire, and the aerosol can explosion fire. In the bulk-load fire test, 178 single-wall corrugated cardboard boxes are stacked in two layers inside a cargo compartment. The containerized fire test uses the same type and quantity of cardboard boxes, but with shredded paper filling the boxes. In the surface burning fire test, a square pan (0.1 m^2) is filled with 1900 cm^3 of Jet A fuel and 385 cm^3 of gasoline to create a pool fire. For the bulk-load, containerized, and surface burning tests, the fuel load is ignited and a predetermined amount of suppressant is applied to the fire to determine the inerting concentration and the consequences of adding sub-inerting concentrations. In the aerosol can explosion test, the contents of a typical aerosol can are impulsively released to

simulate the worst-case scenario of an aerosol can, located in a suitcase, busting as it is heated in a pre-existing fire.

The FAA tested three potential alternatives, $C_6F_{12}O$ (Novec 1230), $C_3H_2F_3Br$ (2-BTP), and C_2HF_5 (HFC-125) with the minimum performance standard. The agents all performed well in the bulk-load, containerized, and surface burning tests; in each test, minimum extinguishing concentrations were determined for each agent and sub-inerting agent concentrations were found to have minimal impact on the fire severity. This was not the case in the aerosol can test (FAA-ACT). Minimum extinguishing concentrations were determined, but sub-inerting agent concentrations unexpectedly made the fire worse.

Figure 1.1: Cargo bay simulator used during the aerosol can explosion test [4].

Figure 1.1 shows the simulated cargo compartment in which the aerosol can tests were performed. It is an 11.4 m^3 cylindrical pressure vessel with hemispherical end caps. As shown in the schematic diagram in Figure 1.2, the chamber contains a pressure gage,

thermocouple, camera, fan, and an aerosol can simulator. During a test, air and suppressant are first premixed in the chamber. The simulated can contents (a two-phase spray of alcohol, propane, and water) are then heated in the aerosol can simulator until a pressure of 16 bar is reached. A fast-acting valve then releases the simulated can contents in the direction of a continuous high-voltage DC arc. The pressure rise in the chamber and the temperature near the ignitor are recorded for each test along with high speed video imaging for examination of fireball size.

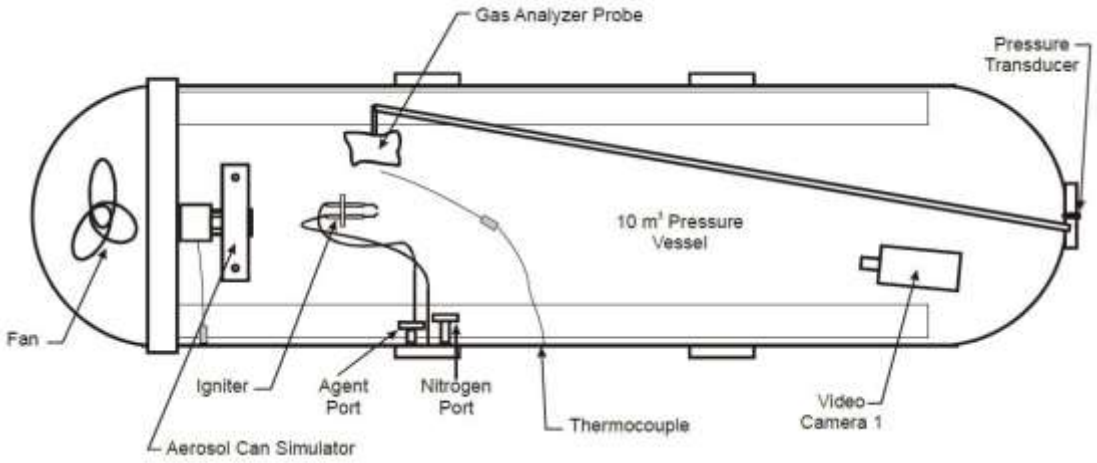

Figure 1.2: Schematic diagram (top view) of the cargo bay simulator [4].

In the absence of suppressant, the pressure rise in the chamber is roughly 1.5 bar. Through repeated tests at different agent volume fractions X_a, the inerting concentration of an agent is determined as the value of X_a required to prevent significant pressure rise. As previously mentioned, the standard also requires that an agent, when added at sub-inerting concentrations, cannot produce a higher pressure rise than the uninhibited case. Unfortunately, all of the alternative agents tested failed this element of the test, whereas Halon 1301 (CF_3Br) did not [4, 5].

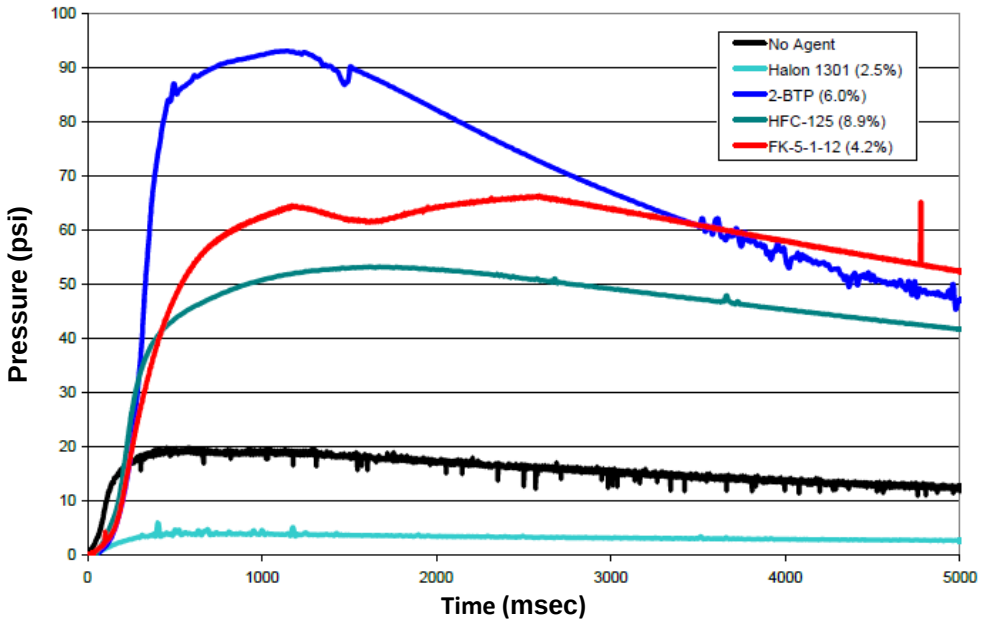

Figure 1.3: Explosion pressure versus time in the aerosol can test when sub-inerting concentrations of the different agents are added [4].

Figure 1.3 illustrates the impact of adding sub-inerting agent concentrations. The black curve shows the pressure rise of the uninhibited case. The peak pressure was 20 psig (1.38 bar) and occurred roughly 500 ms after ignition. With 2.5% by volume CF_3Br (turquoise line), the peak pressure rise was considerably lower (~0.34 bar), whereas with added sub-inerting concentrations of $C_6F_{12}O$, $C_3H_2F_3Br$, and C_2HF_5, the peak pressure rise increased substantially to 4.55, 6.41, and 3.72 bar respectively. A summary of test results provided by Reinhardt et al. [4, 5] is provided in

Table 1.1, which specifies the agent considered, the agent concentration, and the initial temperature during each test. The measured peak pressure and temperature are given along with whether the video footage captured a fire event.

Table 1.1: Summary of the FAA aerosol can test results [4, 5].

Agent	Agent Volume Fraction (%)	Initial Temperature (°C)	Fire Event	Peak Temperature (°C)	Peak Pressure Rise (bar)
None	0	18.3	Yes	197	1.75
None	0	20	Yes	164	1.61
None	0	34.6	Yes	N/A	1.38
Halon 1301	2.5	11.8	Yes	18	0.28
2-BTP	3	21.1	Yes	569	4.34
2-BTP	4	18.3	Yes	591	4.34
2-BTP	5	18.9	Yes	677	6.89
2-BTP	6	17.2	Yes	797	6.41
HFC-125	6.2	10	Yes	552	3.59
HFC-125	8.9	N/A	Yes	664	3.65
HFC-125	11	N/A	Yes	575	3.59
HFC-125	13.5	9.8	No	N/A	N/A
Novec 1230	1	36.5	Yes	N/A	2.28
Novec 1230	2	36.5	Yes	N/A	2.34
Novec 1230	4.2	36.5	Yes	N/A	4.55
Novec 1230	4.2	36.5	No	N/A	N/A
Novec 1230	8.1	36.5	No	N/A	N/A

1.2 Objectives

This study aims to help understand why unwanted combustion enhancement occurred when adding CF_3Br alternatives in the FAA aerosol can test. By studying the agents that failed, we can provide insight into the chemicals to consider during the next round of testing by the FAA. A better understanding of how the chemical structure of an agent influences performance in the specific test could also help guide the potential development of a new molecule that may be successful. In addition to civilian aircraft fire suppression systems, other critical-use applications are facing Halon 1301 phase-out dates in the near future including nuclear power facilities, petrochemical facilities, and

telecommunications facilities [6]. The replacement effort in these areas will also benefit from an improved understanding of why the alternative failed the aerosol can test. The approach of the present study is summarized below:

1) Develop experimental facilities and post-processing methods to determine the burning velocity, peak pressure rise, and flammability limits of spherically propagating flames.
2) Experimentally test the concepts developed via previous numerical simulations and analysis of the FAA aerosol can tests (concepts summarized in the background section).
3) Reproduce the phenomena observed in the complex full-scale FAA experiments to explore the potential of small-scale experiments as tools for screening CF_3Br replacements for aircraft cargo compartments.
4) Examine the performance of potential replacements that were not tested by the FAA.
5) Provide preliminary validation of recently developed and updated kinetic mechanisms.

1.3 Background

A review of the National Institute of Standards and Technology (NIST) aerosol can test analysis is first provided as the present study is directly related to, and motivated by, the previous findings. Kinetic flame inhibition by halogenated compounds is then discussed to familiarize the reader with the inhibition mechanisms and kinetic model development pertaining to the suppressants considered herein. Lastly, model validation

techniques and premixed laminar flame fundamentals are discussed, with a focus on laminar burning velocity.

1.3.1 NIST Analysis of the FAA Tests

The Fire Research Laboratory at NIST helped to interpret the aerosol can test results and provide insight into the causes of enhanced overpressures. Linteris et al. [7] began their analysis with a phenomenological interpretation of the physical nature of the aerosol can explosion test (which is summarized here for clarity and illustrated in Figure 1.4). A two phase mixture of propane, ethanol, and water vapor is released in the chamber, which is filled with premixed air and suppressant at known volume fractions. The high pressure impulsive release of fuel creates turbulent flow conditions and turbulent combustion. With sub-inerting suppressant concentrations, a fireball ensues, which is made up of different regimes that can be adequately described by different reacting systems. As Figure 1.4 illustrates, the fireball likely has a partially premixed fuel-rich core. Near the perimeter, diffusion limited combustion occurs as the can contents which are not contained in the fuel-rich core spread throughout the chamber. Complicating the analysis further, the flow strain varies spatially, with high levels of strain directly downstream of the high pressure fuel release and lower levels of strain present in the end-gases of the chamber. In addition to the complex physical nature of the test, the inhibited reactant mixtures are chemically complex because of the added halogens. Thus, the approach adopted at NIST was to model certain regions of the flame with simplified flame types while incorporating comprehensive chemistry models necessary to understand the inhibition/promotion mechanisms of the tested alternatives.

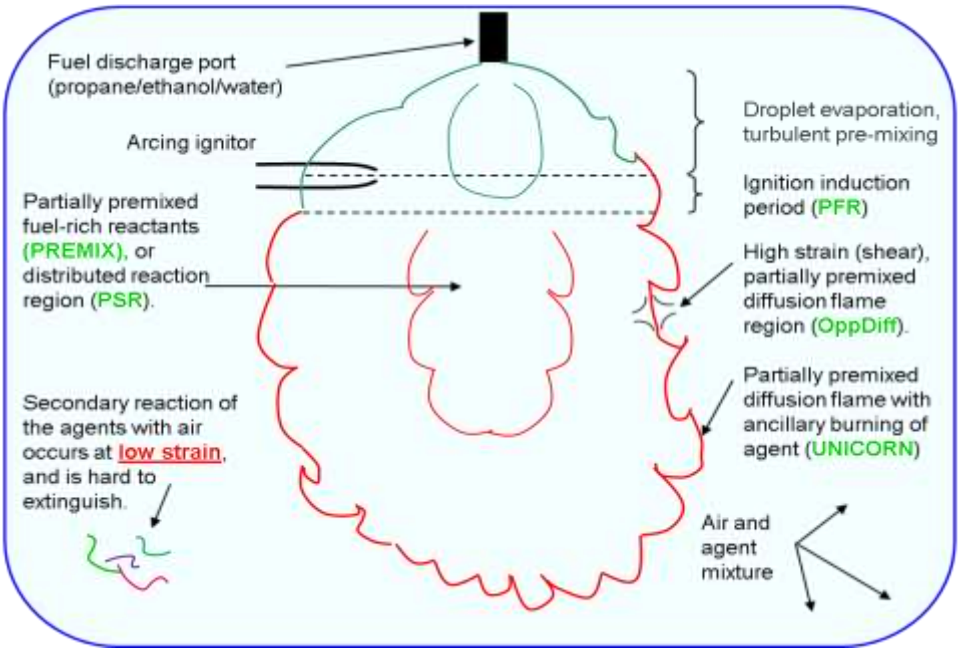

Figure 1.4: Interpretation of the aerosol can test showing regions with local behavior that can be modeled with simplified flame systems [7].

As a first step in understanding the FAA-ACT results, the thermodynamics of the reacting system were examined. In the FAA-ACT, the level of mixing between fuel (aerosol can contents) and oxidizer (premixed air and suppressant) is unknown and potentially controlled by turbulent mixing resulting from the high pressure release of fuel. Therefore, Linteris et al. [8, 9] calculated the equilibrium heat release as a function of the level of mixing between the fuel and oxidizer. In addition, the amount of agent was varied up to the minimum extinguishing concentration observed in the full-sale experiment. Based on the heat release for a given level of mixing, the resulting pressure rise was estimated using the following approach. The volume of the gases involved in reaction (i.e., considered in the equilibrium calculation) are at a new equilibrium volume and the volume of the gases that do not react remain unchanged. The two volumes are

added together and the ideal gas law is used to convert the change in volume of the entire system to a change in pressure if the volume were constant ($V_f/V_i=P_f/P_i$).

Comparison of predicted and actual chamber pressure rise showed that the mixing was likely controlled by diffusion. In a laminar diffusion flame, the flame typically finds the location where stoichiometric proportions of fuel and oxidizer are present. In the FAA-ACT, the expanding/reacting fuel cloud can be considered a diffusion flame that finds the level of mixing resulting in peak temperature (i.e., stoichiometric proportions). While simplistic, this approach provided fairly accurate predictions of the pressure rise considering the level of chamber mixing is unknown.

The equilibrium pressure rise predictions provided insight into the level of mixing and conditions for which combustion was occurring. Among other findings, the calculations showed that with near-inerting concentrations of added C_2HF_5 and $C_3H_2F_3Br$, complete reaction of the fuel and agent is required to produce peak pressure rise observed in the FAA-ACT. That is, the entire contents of the chamber must react, including the agent itself, which provides additional heat release. In contrast, sub-inerting concentrations of CF_3Br were found to not cause overpressures because CF_3Br does not increase the oxygen demand of the system (partly because of the high carbon to halogen ratio and the low concentrations required for extinction).

The thermodynamic calculations provided reasonable estimates of the peak pressure rise when sub-inerting concentrations of the alternative agent were added. However, with sub-inerting concentrations of CF_3Br and with near-inerting concentrations of the alternatives, the calculations over-predicted the pressure rise because kinetic inhibition is not taken into account. To explore the inhibition

performance of the agents tested in the FAA-ACT, Linteris et al. [9, 10] performed modeling with detailed chemistry to obtain a measure of the overall reactivity of the system. Because of the turbulence induced mixing resulting from the high pressure release of fuel, the reaction zone was modeled as a perfectly stirred reactor (PSR). The characteristic reaction time of the system was determined by progressively lowering the reactor residence time until blow-out occurred (i.e., the residence time for which mass exits the reactor at the same temperature it enters). Since reaction rate is an exponential function of temperature, an abrupt change occurs with a small change in residence time resulting in ~1500 K change in the outlet temperature. The overall reaction rate is then taken as the inverse of the reactor blow-off time.

PSR calculations were performed for a range of fuel/oxidizer mixing and agent loading, as done in the equilibrium calculations. To enable modeling with detailed chemistry, comprehensive kinetic models were assembled to describe the decomposition of CF_3Br, C_2HF_5, $C_6F_{12}O$, and $C_3H_2F_3Br$ in hydrocarbon-air systems. A key result of the modeling was that the alternative agents not only increased the heat release when the fuel contents were mixed with a large fraction of chamber (i.e., the fuel/air mixture was lean), they also increased the overall reaction rate. From the equilibrium calculations, the high levels of mixing for which enhanced reactivity occurred were required to reach the pressures observed in the full-scale test. Conversely, the overall reaction rate with added CF_3Br always decreased as more agent was added, no matter the level of mixing.

The equilibrium and PSR modeling showed that reaction was occurring at very lean conditions (near pure suppressant-air flames) and that competition exists between higher heat release from agent reaction (and consequent higher temperature) and slower

reactivity of the halogen-inhibited, hydrocarbon-air system. To explore the potential of pure agent-air mixtures burning in the end gases of the FAA-ACT, Babushok et al [11] calculated 1-D planar burning velocities at initial temperatures and pressures typical of compressed conditions in the constant-volume FAA-ACT chamber (i.e., after reaction of the premixed core containing the majority of the fuel). Simulations showed that at 400 K, pure C_2HF_5- and $C_6F_{12}O$-air at stoichiometric conditions had a burning velocity of 1.56 cm/s and 0.37 cm/s respectively. Adiabatic flame temperatures of roughly 1800 K were also observed for the two agents, which is slightly lower than that of typical hydrocarbon-air flames.

To interpret agent performance when added to diffusion flames, Takahashi et al. [12, 13] modeled inhibited cup-burner flames with a two-dimensional, time-dependent code incorporating full chemistry, diffusive transport, and a gray-gas radiation model. Simulations were performed with the FAA-AACT fuel and with increasing concentrations of CF_3Br, C_2HF_5, $C_2HF_3Cl_2$, and $C_3H_2F_3Br$ added to the air stream. Simulations were first performed in microgravity [12] to reveal the governing physical and chemical processes occurring in the absence of buoyant flow. Additional simulations were performed in earth gravity and with additional agents not considered in the earlier work ($C_2HF_3Cl_2$ and $C_3H_2F_3Br$) [13].

In the microgravity cup-burner simulations, CF_3Br successfully inhibited the main reaction kernel and reduced the overall heat release while C_2HF_5 enhanced the heat release. A unique two-zone flame structure was observed in which the premixed-like reaction kernel (zone 1) formed H_2O from hydrocarbon-air combustion. Farther downstream in the trailing diffusion flame (zone 2) the H_2O was converted further to HF

and COF_2 by exothermic reaction with C_2HF_5 contained in the air. In the earth-gravity simulations, similar trends were observed when adding CF_3Br and C_2HF_5. In addition, the two-zone flame structure was observed when adding $C_3H_2F_3Br$ or $C_2HF_3Cl_2$ to the air, with additional heat release occurring in the outer zone as HF and COF_2 were formed.

1.3.2 Halogenated Flame Inhibition

Halogenated methanes (CF_3Br, CF_2Br_2, CF_2ClBr, etc.) were first used in military aircraft suppression systems during the 1950's. Although the superior performance of halons on a per mole basis (compared to other gaseous agents such as N_2 or CO_2) was recognized around this time, the mechanisms responsible for improved suppression were not fully understood. Much of the early flame inhibition studies focused on determining the minimum inerting concentration (MIC) required to prevent flame propagation and did not attempt to explain the improved performance compared to chemically passive suppressants.

During the late 1950's, researchers began measuring the burning velocity of inhibited hydrocarbon-air systems to better understand the potential chemical inhibition effect of halogenated methanes. Garner et al. [14] added CH_3Cl, CH_2Cl_2, CCl_4, CH_3Br, and CH_2ClBr to premixed C_3H_8-air in a nozzle burner and found the inhibition effectiveness of chlorinated methanes to increase with the number of chlorine atoms. Moreover, the brominated methanes showed a significantly higher inhibiting effect over the chlorinated compounds. Using the Bunsen burner method, Rosser et al. [15] measured the burning velocities of CH_4-air flames with added CCl_4, Br_2, CH_2Br_2, CH_2BrCl, CH_3I, i-C_3H_7I, and CH_3Br. Similar to the findings of Garner et al. [14], a

direct relationship was observed between the magnitude of reduction in burning velocity and the number of halogen atoms in the inhibitor. In addition to measuring burning velocity, Rosser et al. [15] showed that inhibitor addition had little impact on measured peak temperature. Based on the observations of reduced burning velocity and nearly unaffected flame temperatures, Rosser et al. [15] concluded that the agents did not act as diluents (which slow reactivity by lowering the flame temperature). They proposed halogenated compounds inhibit reactivity by reducing the number of radicals (O, OH, and O) that participate in chain initiation reactions, and that inhibition is the result of substitution of less reactive halogen atoms for chain-carrier radicals (H, OH, and O) through the following reactions,

$$H\alpha + X = HX + \alpha \quad (1.1)$$

$$\beta + HX = X + H\beta \quad (1.2)$$

where X is a halogen, HX is a halogen acid, Hα is either the fuel or another hydrogen-containing species, and β is an active chain-carrier radical (H, OH, O, etc.). Additionally, inhibition occurred from the reaction,

$$CH_4 + X = CH_3 + HX \quad (1.3)$$

which inhibits the early stage of methane oxidation. Thus, chain-terminating reactions involving halogens provide alternative paths for H atoms, which reduces the rate of the key chain-branching reaction,

$$H + O_2 = O + OH \quad (1.4)$$

To develop a more complete interpretation of the mechanism of inhibition by halogenated compounds, Levy et al. [16] used a Bunsen burner and mass-spectrometric flame-sampling to measure the burning velocity and major product species concentrations

(H_2O, CO_2, and CO) of premixed CH_4-air flames with added HBr. They hypothesized that if the proposed reaction mechanism in ref. [15] were accurate, addition of inhibitor should result in an almost constant HX concentration with the likelihood of some change in the intermediate concentration of CO and CO_2. Through comparison of CO and CO_2 concentrations in uninhibited and inhibited flames, Levy et al. [16] verified the inhibition mechanism proposed by Rosser et al. [15] and suggested that HBr reduces burning velocity primarily because it inhibits the first stage of methane oxidation.

Before the 1970's, the majority of halogenated inhibition studies were experimental. Thus, several mechanisms of halogenated flame inhibition were proposed based on different experimental observations. The work of Day et al. [17] was among the first to compliment experimental findings with numerical modeling of inhibited flames. The effect of CH_3Br and HBr on the burning velocity of H_2-air and H_2-N_2O flames was measured using an Egerton-Powling burner and modeled by solving the flame conservation equations with detailed kinetics, thermodynamics, and transport. As a first approach, the following brominated reactions were considered in the numerical model,

$$H + HBr = H_2 + Br \quad (1.5)$$

$$H + Br_2 = Br + HBr \quad (1.6)$$

$$Br + Br + M = Br_2 + M \quad (1.7)$$

$$H + Br + M = HBr + M \quad (1.8)$$

$$Br + HO_2 = HBr + O_2 \quad (1.9)$$

with reaction rate coefficients taken from previous studies. Modeling showed that the reduction in H from $H+HBr=H_2+Br$ was not sufficient to provide the observed reduction

in measured burning velocity, and that the remaining four reactions play an important role in the inhibition mechanism of bromine.

The work of Day et al. [17] was extended by Dixon-Lewis et al. [18] to consider the inhibition of HBr and HCl on the flammability limits of upwardly propagating H_2-air mixtures. Moreover, a kinetic mechanism for inhibition by HCl was proposed, consisting of the analog chlorinated reactions of the brominated reactions presented above. The comprehensive modeling effort showed that the efficiency of HBr decreases progressively with higher temperatures and that HBr is less effective when added to lean H_2-air as opposed to rich because of the reduced number of H atoms present. Additionally, HBr was found to be considerably more effective than HCl, and the difference in equilibrium concentrations of Br and Cl was hypothesized to be the cause. The rates of chain terminating reactions depend on the equilibrium concentration of the halogen and since for a given temperature, the concentration of Cl is lower than Br, lower levels of inhibition occur with HCl. The works of Day et al. [17] and Dixon-Lewis et al. [18] were mainly responsible for establishing the general features of flame inhibition mechanism of halogens.

Around the time Day et al. [17] studied inhibition by HBr, Biordi et al. [19-22] comprehensively examined the detailed flame structure of CF_3Br inhibited CH_4-air flames using experimental and numerical techniques. Spatial reactant and product species profiles were measured and compared for CH_4-O_2-Ar and CH_4-O_2-Ar-CF_3Br flames in a low pressure flat flame burner [19]. Among other findings, CF_3 was found to be an additional contributor to the effectiveness of CF_3Br when compared to HBr. CF_3Br decomposes in the preheat zone to form Br and CF_3 which both act to reduce chain-

carrier radical concentrations. The fluorine part of CF_3 eventually forms HF which is then useless as a radical scavenger as it is stable, even to the oxidizing conditions present in the flame zone. In addition to advancing the understanding the inhibition mechanism of CF_3Br, the experimental work yielded rate coefficient information for key elementary reactions required to model CF_3Br decomposition.

In later work, Biordi et al. [20] modified their molecular beam sampling method to enable detection of intermediate halogenated species concentrations in near stoichiometric CH_4-O_2-Ar flames with added CF_3Br. By comparing intermediate spatial species profiles in inhibited and uninhibited flames, Biordi et al. [20-22] deduced the important CF_3Br decomposition reactions and provided estimates for the rates at which they occur. This work helped to determine the important brominated and fluorinated decomposition pathways (particularly the decomposition of CF_3 and CF_2), laying the foundation for kinetic model developments to come.

Westbrook [23] numerically studied the inhibition performance of CH_4- and CH_3OH-air flames with added HBr. At the time, a recently developed kinetic mechanism for C_3HOH oxidation was considered along with reactions involving HBr, Br, and Br_2. The reactions initially considered by Day et al. [17] were included, along with

$$HBr + OH = H_2O + Br, \quad (1.10)$$

$$HBr + O = Br + OH, \text{ and} \quad (1.11)$$

$$Br + H_2O_2 = HBr + HO_2, \quad (1.12)$$

which provide additional radical scavenging within the flame. Westbrook found that the majority of flame inhibition was the result of the reactions $H+HBr=H_2+Br$, $H+Br_2=Br+HBr$, and $Br+Br+M=Br_2+M$. The importance of the three-body reaction that

regenerates Br_2 was elucidated; the above reaction sequence provides a catalytic recombination of H into H_2, while simultaneously reintroducing Br_2 back into the flame zone where it can re-initiate the reaction cycle to further reduce the amount of H atoms.

In subsequent work, Westbrook [24] extended the HBr kinetic mechanism to study chemical inhibition by larger halogenated compounds (up to C2 halocarbons), including CF_3Br. Furthermore, he established the necessary reactions for comprehensively modeling inhibition by HCl and HI (many more reactions than considered in ref. [17]) so that the performance of the inhibitors could be compared with HBr. In this work, the original HBr mechanism, containing 8 reactions, was extended to include 80 halogenated reactions, with each reaction accompanied by rate data taken from literature.

By examining inhibition by HBr, HI, and HCl, Westbrook [24] found I atoms to be the most effective inhibitor, followed by Br, and then Cl. The difference in performance was attributed to the concentration of halogen atom in the pre-flame zone. Cl concentrations were found to be much lower when adding HCl, resulting in a less effective cycling sequence for the removal of H atoms. Higher I and Br concentrations, when adding HI and HBr, result in higher levels of H radical scavenging in the pre-flame zone, and hence, greater reduction in reactivity. During the same study, Westbrook [24] noticed that for certain inhibitors, inhibition effectiveness was dependent on the fuel-air equivalence ratio. When an inhibitor containing a hydrocarbon radical (e.g. CH_3Br) is added to an initially lean mixture, the overall mixture is shifted toward stoichiometric conditions. Thus a halogenated suppressant can simultaneously act as additional fuel in a lean flame while acting as an inhibitor.

The flame inhibition mechanisms of halogenated compounds were more thoroughly understood as a result of the work summarized above (and numerous other studies not mentioned). Until the late 1980's, most technical research efforts were to understand inhibition by different halogenated compounds, while in industry, CF_3Br and CF_2BrCl were mainly used as fire suppressants because of their superior performance on a per mass basis. Before it was discovered that certain compounds were depleting the ozone, there was little incentive to find halon replacements because these two agents had excellent fire suppression efficacy, low toxicity, tolerable material compatibility, and desirable volatility.

The search for halon replacements began shortly after the Montreal Protocol was enacted in 1989. In 1991, the Halon Options Technical Working Conference was established, providing an avenue for researchers with a various backgrounds (fire science, chemistry, toxicology, etc.) to share ideas on what current and future molecules might work as replacements in a variety of applications. Among the many significant contributions, Tapscott et al [25] emphasized the primary processes for removal of inorganic molecules from the troposphere to help identify suitable chemical structures with low ODP. Four processes responsible for the removal of potential ozone depleting substances from the troposphere were highlighted: (1) reaction with atmospheric hydroxyl free radicals, (2) photolysis, (3) physical removal, and (4) reaction with tropospheric ozone. Compounds containing a hydrogen atom were shown to have increased decomposition rates as a result of hydrogen abstraction reactions with hydroxyl radicals. An increase in decomposition through reaction with ozone was shown for alkenes containing carbon-carbon double bonds. This work identified favorable chemical

characteristics from an environmental viewpoint, narrowing the selection field of possible chemicals to consider as halon replacements.

Shortly after the Montreal Protocol, researchers began considering Hydrofluorocarbons (HFC) as potential halon replacements. To enable detailed flame structure analysis with added HFCs, Burgess et al. [26, 27] developed a comprehensive model describing the kinetics of hydrocarbon-air flames with small concentrations of added hydrofluorocarbons. The model included C1-C2 fluorinated species (and subsequent decomposition species) accompanied by reaction rate data collected from shock tube experiments, high level quantum mechanical calculations, and transition state and RRKM theories. Numerous experimental studies followed to validate the model [28-31]. Linteris et al. [28, 29] measured the burning velocity of a premixed CH_4-air inhibited by C1-C3 HFCs. Saso et al. [30] reported stretch-corrected burning velocities of CH_4-air flames with added CHF_3. L'Esperance et al. [31] measured intermediate species profiles in premixed CH_4-O_2 flames containing fluoromethanes. Not only did the experimental studies help validate the model; they helped identify rate coefficient data that needed to be re-evaluated to improve the model.

As the HFC mechanism was being developed, researchers continued to advance the understanding of the inhibition mechanisms of halocarbons. Babushok et al. [32] developed a kinetic model for inhibition by CF_3Br and CF_3I that considered more reaction paths than previously developed models [17, 24]. A number of studies used the model to identify the main inhibition mechanisms when adding inhibitors to organic fuel-air systems [33-35]. Noto et al. [33] examined the influence of CF_3Br, CF_3I, and C1-C2 HFCs on the laminar burning velocity of mixtures of CH_4, CH_3OH, C_2H_6, and C_2H_4 with

air. The inhibition effectiveness of CF_3Br and CF_3I were found to be similar and far greater than that of the fluorinated inhibitors. An exception existed however, in which CF_3I was more effective than CF_3Br when added to the CH_3OH-air flame because of the important reaction of

$$I + HO_2 = HI + O_2. \quad (1.13)$$

Pertaining to the bromine inhibition cycle, the reactions

$$Br + CH_2O = HBr + HCO \text{ and} \quad (1.14)$$

$$Br + HCO = HBr + CO \quad (1.15)$$

were found to be the important channels for HBr formation as opposed to the reactions H+Br+M=HBr+M and $H+Br_2$=HBr+Br that were thought to be the main channels in earlier work [17, 18, 24].

1.3.2 Kinetic Mechanism Validation

As previously mentioned, chemical kinetic mechanisms can be used to incorporate detailed flame chemistry in flame structure modeling. A kinetic mechanism contains a list of elements involved (e.g. H, O, and N in a hydrogen-air system), possible species, and reactions that may occur between the species considered. Every reaction must include some description of the rate at which the reaction occurs, specifically at the conditions of interest (i.e., at typical combustion temperatures). For a bimolecular reaction,

$$A + B \rightarrow C + D \quad (1.16)$$

the rate of reaction is directly proportional to the concentrations of the two reactant species [36], as shown in Eq. 1.17,

$$\frac{dA}{dt} = -k[A][B] \tag{1.17}$$

where k is the rate coefficient, which is a function of temperature. A kinetic mechanism typically provides the rate coefficient of each reaction in the form of the modified Arrhenius equation,

$$k = AT^n \exp(^{-E_a}/_{R_u T}) \tag{1.18}$$

where A is the pre-exponential factor, E_a is the activation energy, R_u is the universal gas constant, T is the temperature, and n is an additional parameter added to increase the robustness of the equation. The pre-exponential factor A accounts for the likelihood of collision between the specified reactants, and the probability of correct orientation during collision to result in reaction (i.e. the steric factor). The exponential factor n modifies the original Arrhenius equation to more accurately fit the temperature dependence of a given reaction. The activation energy E_a describes the temperature dependence of whether a reaction will occur when two molecules collide. In general molecules must be at a certain energy level in order for reaction to occur, as opposed to a collision without reaction. In general, the reaction rate coefficient k is highly dependent on the temperature, hence the exponential relationship seen in Eq. 1.18.

Reaction rate coefficients are typically determined from experiment or estimated using ad initio methods or quantum mechanical methods. It is the potential uncertainty in these rate constants and the potential of omitting important decomposition pathways that affect the accuracy of a kinetic mechanism. Thus, mechanisms are generally developed as a first approximation, improving over time as rate constants are more accurately

determined and as experimental validation helps identify portions of the model requiring improvement.

Simplified experiments can be performed to validate kinetic mechanisms. Global combustion properties, such as shock-tube ignition delay times, laminar flame speeds, extinction strain rates, and detailed product species profiles during oxidation in flow reactors and in laminar flames can be measured and compared to numerical simulations. Flame codes, such as those in CHEMKIN, combine combustion theory and numerical methods to model flame structures with detailed chemistry. Simplified flame configurations, such as steady 1-D freely propagating flames, can be modeled with relative ease. Such models minimize aerodynamic influences and heat losses so that the impact of changing flame chemistry can be isolated. It is the simplified flame structures, incorporating detailed chemistry, that are typically compared to experimental data as a means of validation.

The CHEMKIN package provides further validation assistance by providing sensitivity and reaction pathway analysis. For instance, the laminar flame speed can be calculated for a given set of reactants and a sensitivity analysis can provide the most influential reactions governing the flame speed. If there is considerable error between the numerical and experimentally measured flame speed, then the sensitivity analysis provides a ranking of reactions for which uncertainties in the rate coefficients can be examined as possible causes of the prediction error.

1.3.4 Measuring Laminar Burning Velocity

Several techniques exist for measuring the burning velocity of laminar flames. In recent studies contained in the literature, one of the following flame configurations are often used: (1) rim stabilized conical flame, (2) counterflow flame, (3) heat flux-stabilized flat flame, (4) constant-pressure spherically propagating flame, and (5) constant-volume spherically propagating flame. Summaries describing the different techniques are available in refs. [37-39].

Regardless of the experimental technique, the laminar burning velocity (also referred to as the laminar flame speed) is defined as the speed relative to the unburned gas with which a planar one-dimensional adiabatic flame front travels along the normal to its surface [38]. It is a fundamental property of a mixture, which is controlled by the rate of reaction, diffusion, and heat transfer. While simplistic, the idealized flame configuration used to define the laminar burning velocity is rarely achievable in the laboratory. With current configurations, the upstream flow is frequently non-uniform while the flame is also either propagating and/or curved [40]. As a result, a tangential velocity gradient is present at the flame surface, causing flame stretch [41]. Stretch can cause the measured burning velocity to differ from the fundamental 1-D planar burning velocity; how flame stretch affects the burning velocity (i.e. whether it increases or decreases it) dependents on the rates of thermal diffusivity and mass diffusivity in the reactant mixture, which can be expressed in terms of the non-dimensional Lewis number Le. The Lewis number is often expressed in one of two ways; either the ratio of the reactant thermal diffusivity ($k/\rho c_p$) to the mass diffusivity of the deficient reactant (fuel in a lean system or air in a rich system) or the ratio of the mass diffusivities of the deficient

and abundant reactants. Detailed discussions on the origin and effect of flame stretch can be found in refs. [40, 42, 43].

Flame cooling through heat transfer to the surroundings can also affect the measurements. Thus experiments are carefully designed to minimize the effects of heat loss so that the reported value most closely represents the fundamental laminar burning velocity predicted by simplified numerical models. Recently. refs. [37, 44, 45] suggested modeling actual experimental flame conditions; in the case of spherically expanding flames, the stretched burning velocity, which is a function of the flame radius, can be directly compared to simulation, eliminating the potential uncertainty associated with extrapolating experimental data to zero-stretch conditions. Although this may become the standard approach in the future, simulation of spherically expanding flames with full chemistry is currently computationally expensive, especially when simulating inhibited flames that have a large number of species and reactions.

Spherically propagating flame techniques have gained popularity in recent years in part because the experiment is simple and can characterizes the flame response to stretch. In addition, minimal heat losses are present (compared to other experiments) and unstretched burning velocities can be extracted from the measured data. The spherically propagating flame technique is also advantageous for tests with halogenated hydrocarbons because only a small mass of reactants is needed for each test, as opposed to continuous flows required with other methods. Thus, less product gases are produced, which, in the presence of halogenated compounds, contain toxic acids (HF, HCl, etc.). Based on the above-mentioned reasons, the present study uses spherically propagating

flame experiments to measure peak pressure rise and burning velocity of inhibited hydrocarbon-air flames.

Chapter 2: 1.85 L Chamber Experiment

2.1 Introduction

The 1.85 L chamber experiment can provide the flammability limits, explosion pressure (constant-volume), and rate of pressure rise. Further processing of the latter can be used to obtain the laminar burning velocity (1-D spherical) as a function of initial pressure and temperature (which increase as the unburned gases are compressed). The method for determining burning velocity has been referred to in the past as the constant volume method [46] and the spherical-vessel method [47]. It is often referred to as the constant volume method because a closed vessel the increase in pressure within the closed vessel is used to determine the burning velocity.

2.2 Apparatus and Instrumentation

A schematic of the constant-volume apparatus is shown in Figure 2.1. The stainless steel (316) spherical vessel is similar to previous designs [47-50], with an inner diameter of 15.24 cm, volume of 1.85 L, wall thickness of 2.54 cm, and equipped with electrodes, an absolute pressure gauge, a dynamic pressure sensor, and a thermocouple. The 1.85 L experiment is shown in Figure 2.2.

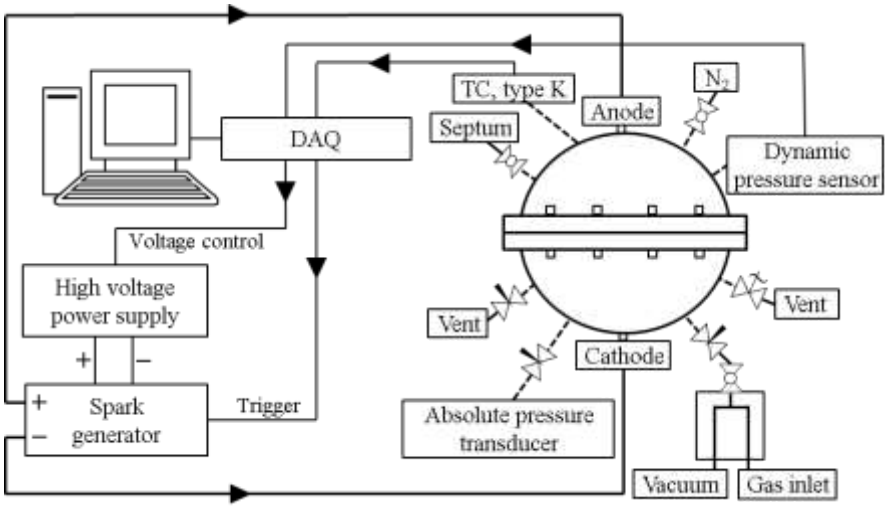

Figure 2.1: Schematic diagram of the 1.85 L experiment.

Figure 2.2: Image of the 1.85 L experiment.

A vacuum pump reduces chamber pressure below 0.1 Torr prior to reactant addition. Test mixtures are prepared in the chamber using the partial pressure method, following injection of first liquid then gaseous reactants. Component partial pressures are determined with an absolute pressure transducer (Omega, PX811; claimed accuracy of 0.1% of reading) that is periodically calibrated against a Baratron 627D (claimed accuracy of 0.12%) and a Wallace & Tiernan 1500 pressure gage (claimed accuracy of 0.066%). Liquid suppressants ($C_6F_{12}O$, $C_3H_2F_3Br$, and $C_2HF_3Cl_2$) are injected using a syringe and a gas-tight septum separated from the chamber by a ball valve (to ensure leak-free operation during the experiment).

A capacitive discharge ignition system (based on the work of Shepherd et al. [51], and shown in Figure 2.3) provides a controlled spark with an estimated energy range of 0.05-500 mJ. Two tungsten electrodes form an adjustable gap (typically 2 mm) in the center of the chamber, and thin electrodes (diameter of 0.4 mm) ensure minimal heat loss from the flame. The explosion pressure is recorded at 4000 Hz using a dynamic pressure sensor, with a claimed accuracy of 0.1% of reading.

The spark generator was designed and built in concurrence with the 1.85 L experiment. The objective was to build a system that could provide near minimum ignition energies for typical stoichiometric hydrocarbon-air mixtures (e.g., CH_4- and C_3H_8-air) as well as near-limit inhibited hydrocarbon-air mixtures. The former require ignition energies around 0.2-0.3 mJ [52] while the latter require energies several orders of magnitude higher. Therefore, the challenge was to create a system that could provide a very wide range of ignition energies.

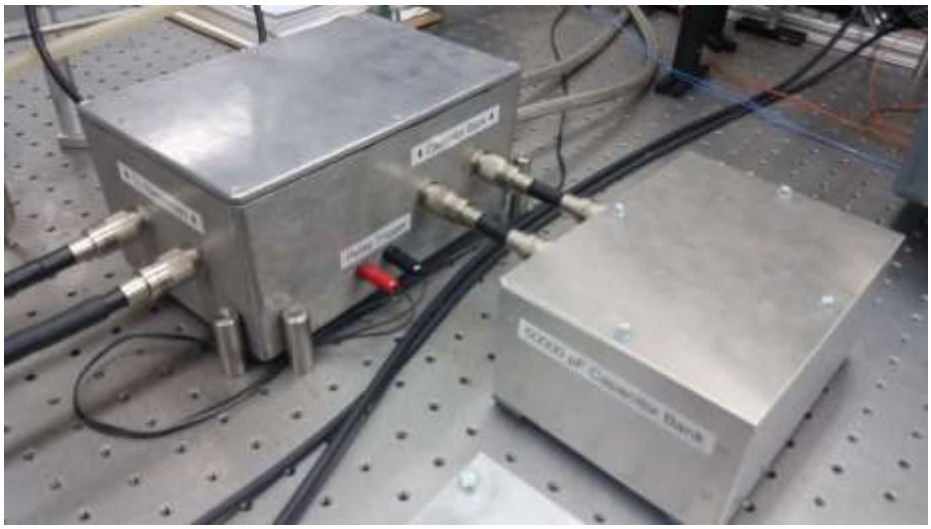

Figure 2.3: Spark generator with interchangeable capacitor banks.

The spark generator is comprised of an adjustable high voltage power supply, a high voltage relay, interchangeable capacitor banks, and resistors (shown in Figure 2.4). The high voltage power supply (model P015HP4) is made by Acopian and can provide up to 15 kV DC. The voltage is adjusted either manually using the front panel dial or by an input analog voltage signal between 0-5 V (0V and 5V input corresponding to 0kV and 15kV output). The positive terminal of the power supply is connected to the normally open terminal of the high voltage relay (Gigavac G15). A 1 GΩ resistor is placed in series between the two components to limit the current from the power supply to an acceptable limit. Connected to the common terminal of the high voltage relay is an interchangeable capacitor bank (seen in Figure 2.3 as the box on the right). Thus, when the relay is closed the high voltage power supply is connected to the capacitor bank and charging occurs. Once the desired charge is reached, the relay is switched closed by applying 5 V DC to it. When the relay is closed the charged capacitor bank becomes in series with the spark gap located at the center of the chamber. High voltage cables

extend from the spark generator to the anode and cathode electrodes. There is a built-in voltage divider (resistors R_2, R_3, and R_{meter} in Figure 2.4) in the spark generator that was included to monitor the capacitor discharge voltage; it was used for a select number of tests and the discharge voltage typically peaked early on around the charging voltage, and decayed gradually during the discharge process.

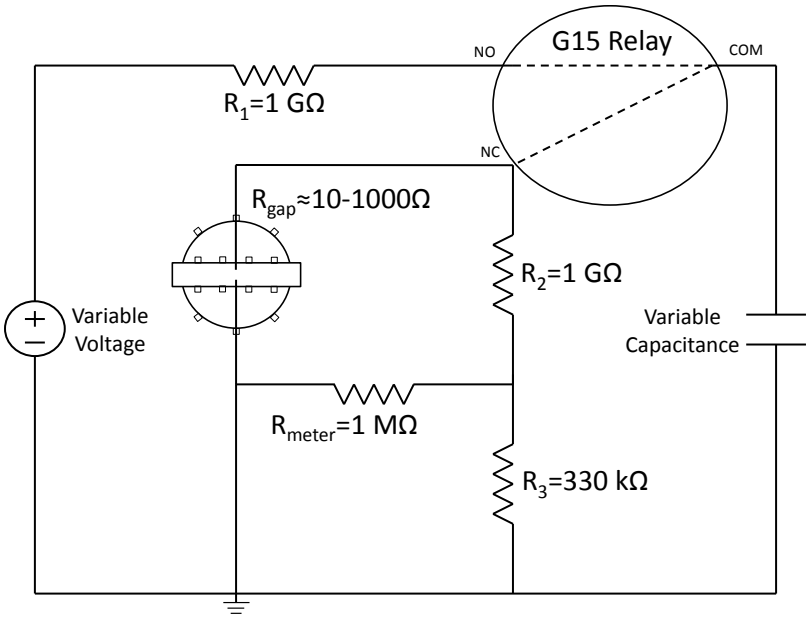

Figure 2.4: Circuit diagram of the spark ignition system.

Several capacitor banks were built to provide a wide range of spark energies with the 15kV power supply. In terms of safety, the maximum design voltage sets the spacing required to avoid internal arcing, which creates stay paths for current to flow. If we had used a higher design voltage, not only would the required spacing of all components be larger, specialty cables and connectors would have also been required for safe operation. By designing the system so that different capacitor banks could be attached, the spark generator could provide the necessary range of energy while being having an acceptable maximum design voltage.

The capacitor banks typically contained 2-6 capacitors in series or in parallel, depending on the design specifications of off-the-shelf capacitors that could be acquired. The energy stored in a capacitor is expressed in Eq. 2.1,

$$E = \frac{1}{2} C v^2 \tag{2.1}$$

where E is the stored energy, C is the capacitance, and v is the charging voltage of the capacitor. In general, as the capacitance increased, the maximum charging voltage decreased. Thus, it was difficult to find individual capacitors that could be charged to a voltage high enough to generate a spark while also storing enough energy to ignite near limit mixtures. Table 2.1 provides the total capacitance of each bank along with the minimum and maximum stored energy (based on a charging voltage of 5kV and 15kV).

Table 2.1: Estimated range of spark discharge energy for the different capacitor banks with the minimum and maximum energies based on a charging voltage of 5 kV and 15 kV.

Capacitance (nF)	Min stored energy (mJ)	Max stored energy (mJ)	Estimated min spark energy (mJ)	Estimated max spark energy (mJ)	discharge time (us)
0.94	11.8	105.8	0.06	0.53	9
1.18	14.7	132.2	0.07	0.66	12
2.35	29.4	264.4	0.15	1.32	24
5	62.5	562.5	0.31	2.8	50
7.33	91.7	825	0.46	4.1	74
10	125	1125	0.62	5.6	101
22	275	2475	1.37	12.31	221
50	625	5625	3.11	27.99	503
100	1250	11250	6.22	55.97	1005

The actual energy deposited by a spark is difficult to measure. There are several losses that make the energy stored in the capacitors much larger than the energy delivered to the electrodes. Marshall et al. [53] estimated that 25% of the energy stored in an

induction coil was delivered as spark energy across the electrodes. It was also noted that the energy delivered to the electrodes is not the same as the spark energy delivered to the reaction kernel since the electrodes have an electrical efficiency as well. Eisazadeh-Far et al. [54] estimated that only about 10-25% of the electrical energy delivered to a spark is converted to thermal energy due to cathode fall and radiation losses. In addition to the above mentioned difficulties in determining minimum ignition energies, the primary objective of the present study is to measure burning velocity and peak pressure rise. As long as the energy can be set near the minimum, burning velocity and peak pressure rise can be measured with minimal influence by the ignition process. Therefore, the actual ignition energy are not measured; instead, as done in many other studies, the stored energy and estimated spark energy are reported (Table 2.1).

The spark energy is estimated by estimating the total resistance of the circuit once the high voltage relay closes and the capacitor bank is connected to the chamber electrodes. By doing so, the power dissipated by each resistive component, including the spark gap can be determined as the fraction of individual resistance to the total circuit resistance. By assuming that the gap resistance is on the order of 100 Ω, the correct order of magnitude for the minimum ignition energy of stoichiometric CH_4-air was estimated based on the stored energy in the capacitor. The estimate of the total circuit resistance was used to estimate the spark discharge times as well, which are included in Table 2.1.

The sample gases used during experiments are CH_4 (Matheson Tri-Gas, 99.97% purity), C_3H_8 (Scott Specialty Gases, 99.0% purity), CF_3Br (Great Lakes Chemical Corp., 99.6% purity), $C_6F_{12}O$ (3M, > 99% purity), $C_3H_2F_3Br$ (American Pacific Corp., > 99% purity), C_2HF_5 (Allied Signal Chemicals, 99.5% purity), and $C_2HF_3Cl_2$ (American Pacific

Corp., > 99% purity). The air is house compressed air (filtered and dried) that is additionally conditioned with a 0.01 μm filter, carbon filter, and a desiccant bed to remove small aerosols, organic vapors, and water vapor before use. The relative humidity of the air, measured with a humidity gage (TSI VELOCICALC, 8386), is less than 2% for all tests. A schematic of the gas handling system is shown in Figure 2.5.

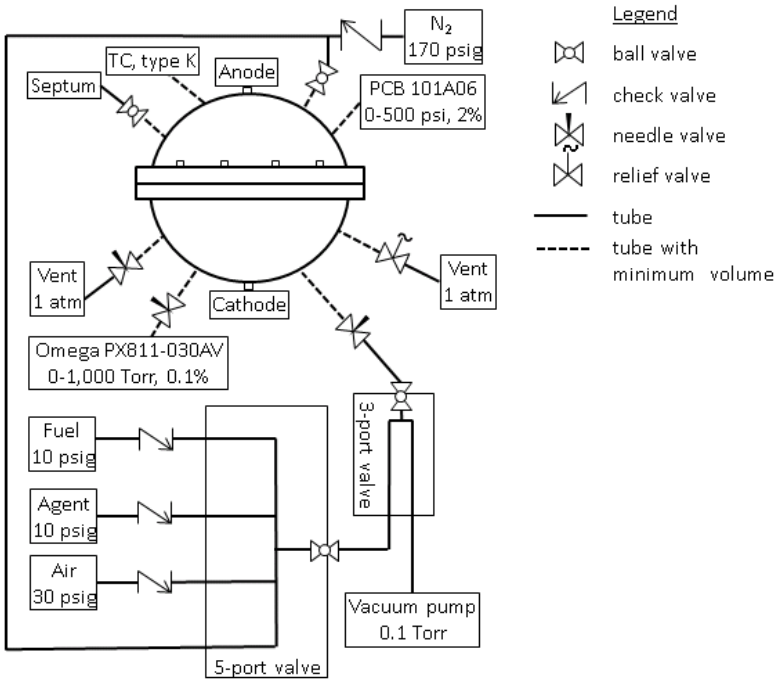

Figure 2.5: Diagram of the 1.85 L experiment showing the gas handling system.

For a test, the reactants are added, followed by a five minute mixing and settling time [48]. Ignition is attempted several times, while gradually increasing the capacitor charging voltage, until ignition occurs. This ensures the ignition energy is within an order of magnitude of the minimum value. (Note that for stoichiometric iso-octane–air mixtures, Marshall et al. [53] found that the burning velocity was insensitive to the ignition energy for values up to 1000 times the minimum ignition energy.) The explosion

pressure is recorded at 4000 Hz with a dynamic pressure sensor (PCB Piezotronics, 101A06; claimed accuracy of 0.1% of reading). The product gases are immediately purged to vacuum via a large flow of N_2 (to minimize acid gas exposure to, and heating of, the experiment), and the chamber is allowed to cool for 20 minutes before the next experiment.

A LabView VI aids in operation of the experiment. The VI controls the capacitor bank charging voltage and the triggering of the data acquisition and the ignition. Once the capacitor bank is charged to the desired level an analog dc voltage is sent to the high voltage relay (within the spark generator) causing it to close and connect the charged capacitor bank to the electrodes (producing the spark). The data acquisition is triggered by the same analog voltage signal sent to the high voltage relay. There is a 15 μs delay from when the high voltage relay receives the signal and when it closes, causing the spark to occur 15 μs after the data acquisition begins. For each test, the instantaneous temperature and pressure are displayed graphically by the VI and saved to a .csv file.

2.3 Burning Velocity from the Pressure Trace

The initial development of the spherically propagating constant-volume method for measuring burning velocity can be found in the works of Lewis and von Elbe [55-57]. In the present study, laminar burning velocity is determined from the pressure trace using a thermodynamic model similar to that developed later by Metghalchi and Keck [48, 58] and further refined by others [47, 59]. The contents of the chamber are divided into burned and unburned zones separated by a reaction sheet, assumed to be of zero thickness, spherical, and smooth (no instabilities). Initially, the unburned gas is

considered mixed and at rest. As the unburned gases react, the pressure increases in a spatially uniform manner. The burned gas is in chemical equilibrium and both the burned and unburned gases are considered as ideal, semi-perfect gases. Both zones are adiabatic, and the unburned gas is isentropically compressed as the mixture reacts in the flame sheet.

With these assumptions, the instantaneous flame radius and burning velocity can be determined from the pressure trace. The volume of the chamber is first expressed as the volume of burned and unburned gases (Eq. 2.2),

$$V = V_b + V_u = y_b M v_b + (1 - y_b) M v_u \tag{2.2}$$

where V is the chamber volume, M is the total mass, y_b is the fraction of mass burned, v_b is the specific volume of the burned gas, and v_u is the specific volume of the unburned gas. Assuming the unburned gas is ideal and compression occurs isentropically, v_u is related to P by Eq. 2.3.

$$v_u = v_{u0} \left(\frac{P_0}{P}\right)^{1/\gamma_u} = \frac{V}{M} \left(\frac{P_0}{P}\right)^{1/\gamma_u} \tag{2.3}$$

where v_{u0} is the initial specific volume (which is equal to the chamber volume divided by the total mass V/M), P_0 is the initial pressure, P is the instantaneous pressure, and γ_u is the specific heat ratio of the unburned gas. The unburned gas is considered to be semi-perfect with a specific heat ratio that varies with temperature $\gamma_u(T_u)$. Next, the chamber volume V is expressed in terms of the chamber radius R in Eq. 2.4,

$$V = \frac{4}{3}\pi R^3 \tag{2.4}$$

and the burned gas volume V_b in terms of the flame radius R_f in Eq. 2.5.

$$V_b = y_b M v_b = \frac{4}{3}\pi R_f^3 \tag{2.5}$$

Inserting Eqs. 2.3, 2.4, and 2.5 into Eq. 2.2 yields Eq. 2.6,

$$\frac{R_f}{R} = \left[1 - (1 - y_b)\left({P_0}/{P}\right)^{1/\gamma_u}\right]^{1/3} \tag{2.6}$$

which gives the normalized flame radius R_f/R in terms of the initial conditions, the instantaneous pressure, and the burned gas mass fraction.

The mass burning rate, expressed in terms of ρ_u and S_u, is equal to the time rate of change of burned gas passing through the flame front surface area (Eq. 2.7),

$$\rho_u S_u = \frac{1}{A_f}\frac{dm_b}{dt} \tag{2.7}$$

where A_f is the surface area of the flame front and m_b is the mass of burned gas. The mass of burned gas can be expressed alternatively using Eq. 2.8.

$$m_b = y_b M = y_b \frac{V}{v_{u0}} = y_b \frac{{4}/{3}\pi R^3}{v_{u0}} \tag{2.8}$$

By expressing ρ_u in terms of specific volume and the flame front area A_f in terms of the flame radius ($A_f = 4\pi R_f^2$), Eqs. 2.3, 2.7, and 2.8 are combined to form Eq. 2.9.

$$S_u = \frac{R}{3}\left(\frac{R}{R_f}\right)^2 \left(\frac{P_0}{P}\right)^{1/\gamma_u} \frac{dy_b}{dt} \tag{2.9}$$

Substituting the previous relationship for R_f/R (Eq. 2.6) into Eq. 2.9 yields the final expression for burning velocity,

$$S_u = \frac{R}{3}\left[1 - (1 - y_b)\left(\frac{P_0}{P}\right)^{1/\gamma_u}\right]^{-2/3} \left(\frac{P_0}{P}\right)^{1/\gamma_u} \frac{dy_b}{dt} \tag{2.10}$$

in which S_u is the laminar burning velocity.

To determine burning velocity, the mass fraction of burned gas y_b must be related to the chamber pressure. A linear model relating the two was first proposed by Lewis

and von Elbe [56], and is shown in Eq. 2.11. It is a simple linear relationship between the chamber pressure and the mass fraction of burned gas and has been used recently to determine burning velocity [49] and to validate more complex models [60, 61].

$$y_b = \frac{P-P_0}{P_e-P_0} \tag{2.11}$$

Where P is the instantaneous pressure, P_o is the initial pressure, and P_e is the final pressure. Assuming a linear relationship between P and y_b greatly simplifies the application of Eq. 2.10 and results in the modified version shown by Eq. 2.12.

$$S_u = \frac{R}{3}\left[1 - \left(\frac{P_e-P}{P_e-P_0}\right)\left(\frac{P_0}{P}\right)^{1/\gamma_u}\right]^{-2/3}\left(\frac{P_0}{P}\right)^{1/\gamma_u}\frac{\frac{dP}{dt}}{(P_e-P_0)} \tag{2.12}$$

It should be noted that the experimental final pressure cannot be used in this equation because it is always lower than the theoretical maximum because of heat loss as the flame approaches the chamber walls. To properly apply Eq. 2.12, the final pressure must come from an equilibrium calculation of an adiabatic, constant-energy, constant-volume (UV) process. The calculation provides the theoretical pressure rise occurring in the chamber with zero heat loss. Application of the linear model requires only knowledge of the initial temperature, initial pressure, equilibrium pressure, and the instantaneous pressure during a test (all of which are easily obtained).

As previously mentioned, one can perform a thermodynamic control volume analysis on the contents within the chamber to more accurately relate y_b to P [48]. A two-zone thermodynamic model is used in the present work. This method introduces the concept of shells of a given mass, radius, or time increment burning subsequently as the flame front propagates through the unburned mixture. With a two zone model, the temporal evolution is considered to proceed as illustrated in Figure 2.6. The contents of

the chamber are centrally ignited. The change in pressure from the initial pressure P_0 to the first measured increase in pressure P_1 corresponds to the flame front consuming the first "shell". The chamber then consists of a burned and unburned gas region, each at a uniform pressure P_1. After the first shell burns, the temperature of the unburned gas increases as a result of compressive heating. The flame front then consumes the second shell (which is at a new unburned gas temperature) and the burned contents of the shell mix with the contents of the first shell to form the new burned gas region. The entire flame propagation is modeled in this way until the flame front reaches the chamber walls and all contents of the chamber are burned.

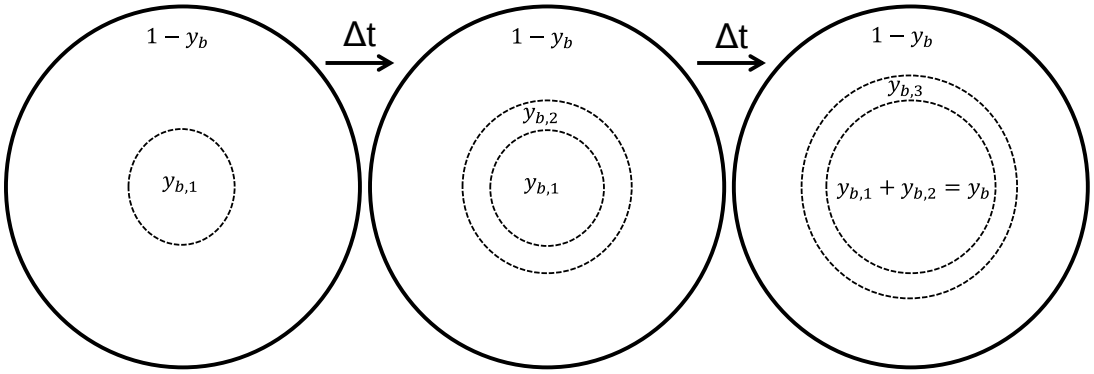

Figure 2.6: Illustration of the two-zone thermodynamic model.

The quantity of gas considered to burn as the flame consumes each shell can be treated in a number of ways. Saeed et al. [62] modeled flame propagation using shells of equal radius and shells of equal mass and found that the two methods gave similar results for burning velocity. An alternative approach is to consider each shell to contain the volume which burns as a result of each recorded pressure rise increment [63-65]. The volume of each shell is then given as the change in flame radius occurring over some time period. Therefore, the size of each shell is related to the frequency at which the

pressure data is collected. The advantage of this method is that post processing of Eq. 2.10 does not require interpolation of y_b and dy_b/dt between the values calculated for shells of equal mass or radius. For simplicity, the present study incorporates the latter method because the method used during post-processing has minimal impact on the calculated burning velocity.

In the two-zone thermodynamic model, the fraction of mass burned x_b is found from simultaneous solution of the conservation of mass and energy equations. Heat transfer is ignored, simplifying the conservation of energy equation. The conservation of mass is expressed in Eq. 2.13,

$$\frac{V}{M} = \int_0^{y_b} v_b dy + \int_{y_b}^1 v_u dy \tag{2.13}$$

With the integrated form shown in Eq. 2.14,

$$\frac{V}{M} = v_{u0} = y_b v_b + (1 - y_b) v_u \tag{2.14}$$

where V is the volume of the chamber, M is the mass of the initial gas in the chamber, v_{u0} is the initial specific volume of the reactants in the chamber, v_u is the specific volume of the unburned gas, y_b is the mass fraction of burned gas, and v_b is the specific volume of the burned gas. The specific volume of unburned gas v_u is determined using Eq. 2.15 which is the isentropic relationship with a variable specific heat ratio that is a function of temperature, $\gamma_u(T)$.

$$v_u(t) = v_{u0} \left(\frac{P_0}{P(t)}\right)^{1/\gamma_u} \tag{2.15}$$

where P_0 is the initial pressure in the chamber, $P(t)$ is the instantaneous pressure, γ_u is the specific heat ratio, and v_{u0} is the initial specific volume of unburned gas. The

specific volume of the burned gas is a function of the burned gas temperature and composition, as illustrated in Eq. 2.16.

$$v_b(t) = v_b(T_b(t), comp_b(t)) \tag{2.16}$$

The conservation of energy is

$$\frac{E}{M} = \int_0^{y_b} e_b dy + \int_{y_b}^1 e_u dy \tag{2.17}$$

with the integrated form shown in Eq. 2.17.

$$\frac{E}{M} = e_{u0} = y_b e_b + (1 - y_b) e_u \tag{2.18}$$

where E is the total energy during adiabatic combustion, e_{u0} is the initial specific energy of the reactants within the chamber, e_b is the specific energy of the burned gas, and e_u is the specific energy of the unburned gas. The unburned gas is assumed ideal; hence the specific internal energy is a function of temperature and composition. The unburned gas composition is considered frozen as the unburned gas temperature T_u increases. The specific internal energy of the unburned gas e_u is then a function of the original reactant composition and the unburned gas temperature T_u. The unburned gas temperature is determined using the isentropic relationship shown in Eq. 2.19, which is valid for ideal gases under uniform pressure.

$$T_u(t) = T_{u0} \left(\frac{P(t)}{P_0}\right)^{(\gamma_u - 1)/\gamma_u} \tag{2.19}$$

where P_0 is the initial pressure in the chamber, $P(t)$ is the instantaneous pressure, γ_u is the specific heat ratio, and T_{u0} is the initial temperature of unburned gas. The specific energy of the unburned gas is a function of the unburned gas temperature and original composition, as seen in Eq. 2.20.

$$e_u(t) = e_u(T_u(t), comp) \tag{2.20}$$

The specific energy of the burned gas, shown in Eq. 2.21, is also a function of temperature and composition.

$$e_b(t) = e_b(T_b(t), comp(t)) \tag{2.21}$$

A single equilibrium calculation is performed at the initial pressure and temperature to provide the equilibrium products and corresponding volume fractions. In the two-zone model, the burned gas is assumed to be the product composition given by an equilibrium calculation at the initial conditions. In this manner, the change in temperature and pressure does not affect the product species and the products of each burned shell are identical, resulting in a uniform burned gas composition. (A more complex handling of the burned gas region is described later by the multi-zone model approach.) For the two-zone model, the temperature of the entire burned gas region is taken as the burned gas temperature of the last shell since compression of the previously burned gases are ignored. Thus, no temperature or density gradients exist in the burned gas region, which is equivalent to assuming infinitely fast conduction within the entire region [59]. By treating the burned gas in such a way, a single specific volume and internal energy can describe the entire zone since the composition and temperature are assumed to be uniform.

Thermodynamic data for the unburned and burned gases are required for model implementation. Data for hydrocarbon-air species (CH_4, O_2, N_2, CO_2, H_2O, CO, NO, OH, H_2, and O) are taken from GRI-mech 3.0 [66], fluorinated species ($C_6F_{12}O$, C_2HF_5, F, HF, CF_4, and CF_2O) from the NIST HFC mechanism [26, 27], brominated species (CF_3Br, $C_3H_2F_3Br$, Br, HBr, and Br_2) from Babushok et al. [32, 67], and chlorinated species (Cl and HCl) from Burcat et al. [68]. Hydrocarbon-air product species are

included for all mixtures, along with fluorinated products when adding $C_6F_{12}O$ or C_2HF_5. Additional brominated products are included for tests with CF_3Br or $C_3H_2F_3Br$ and chlorinated products for tests with $C_2HF_3Cl_2$.

Because γ_u is a function of the unburned gas temperature T_u and the initial mixture composition, T_u and γ_u are solved iteratively at each pressure increment. The properties of the unburned gas mixture, v_u and e_u, are determined from the mixture composition and temperature. The remaining unknowns in the conservation equations (v_b, e_b, and y_b) are found through iteration of T_b (v_b and e_b are functions of temperature) and y_b at each pressure increment, until the proper values of T_b and y_b are obtained. The built-in Matlab nonlinear optimization routine FSOLVE minimizes the residuals of the conservation equations to determine T_b and $y_{b.}$ Burned gas species concentrations, required for the determination of v_b and e_b, are estimated for each value of T and P using a constant volume equilibrium calculation performed via the CEA2 routine of Gordon and McBride [69]. The enthalpies of formation of $C_6F_{12}O$, C_2HF_5, $C_3H_2F_3Br$, and $C_2HF_3Cl_2$ (required for CEA2 calculation) are from refs. [10, 26, 70, 71]. Once $y_b(P)$ is known, the burning velocity $S_u(P, T_u)$ is calculated over the experimental range of pressure and temperature using Eq. 2.10.

Although not used in this study, an overview of the multi-zone model is provided for clarity. It is an extension of the two-zone model which includes temperature, density, and composition gradients in the burned gas region. Hopkinson [72] proposed that the burned gas composition varies radially due to the increase in pressure and temperature of the unburned gas before it is burned. One of the earlier models to incorporate these gradients was that of O'Donovan et al. [73]. The multi-zone models of Saeed et al. [74]

and Eisazadeh-Far et al. [64] are recent examples in which gradients in temperature and gas composition are considered when determining the instantaneous burning velocity.

As the contents in the chamber react, the pressure increases and the temperature of the unburned gas increases as a result of compressive heating. Subsequently, as the flame propagates through the mixture, the burned gas products and temperature change because of the change in temperature before they burn. In addition, the increase in pressure as the reaction progresses compresses the burned gases behind the flame sheet. These two effects result in temperature, density, and composition gradients in the burned gas (varying radially). In previous work, a temperature difference of roughly 500 K was calculated between the burned gases at the center and near the edges of the chamber [62, 75]. The gases at the core end up at the highest temperature as the effect of compression on the initial burned gas is greater than the effect of increased unburned gas temperature on the temperature of the final gases to burn.

The conservation of mass and energy equations are modified to account for burned gas shells with variable temperature and composition. Eqs. 2.14 and 2.18 from the two-zone model are replaced by Eq. 2.22 and Eq. 2.23 in the multi-zone model [76]. The subscript i represents the previously burned shells and n represents the most recent shell to burn.

$$\frac{V}{M} = \sum_{i=0}^{n-1} y_{b,i} v_{b,i} + y_{b,n} v_{b,n} + \left(1 - \sum_{i=0}^{n-1} y_{b,i} - y_{b,n}\right) v_u \tag{2.22}$$

$$\frac{E}{M} = \sum_{i=0}^{n-1} y_{b,i} e_{b,i} + y_{b,n} e_{b,n} + \left(1 - \sum_{i=0}^{n-1} y_{b,i} - y_{b,n}\right) e_u \tag{2.23}$$

where $\sum_{i=0}^{n-1} y_{b,i} v_{b,i}$ is the summation of the product of mass fraction burned and specific volume of each previously burned shell, $y_{b,n} v_{b,n}$ is the product of the mass fraction

burned and specific volume of the most recently burned shell, $\sum_{i=0}^{n-1} y_{b,i}$ is the summation of mass fraction of burned gas in all of previously burned shells, and $y_{b,n}$ is the mass fraction on burned gas contained in the most recently burned shell. A similar description holds for Eq. 2.21, with the specific volume replaced by internal energy.

Figure 2.7 illustrates the multi-zone model concept. The burning of shell 1 is handled the same as in the two-zone model. As shell two is consumed, the reactants are at a higher initial temperature before they burn (compared to the reactants in shell 1), changing the product composition and final temperature. In the model, the shells do not mix and no conduction occurs between them resulting in temperature and density gradients. The composition of each burned gas shell is estimated by assuming a certain volume of gas is burned at every time step, corresponding to each pressure measurement (as done in the two-zone model). As each shell reacts, the volume of gas is assumed to be small enough so that constant pressure expansion occurs. The burned gas products of each shell are assumed to be the equilibrium products corresponding to a calculation incorporating the unburned gas temperature and pressure of the shell. Thus, constant-enthalpy, constant-pressure (HP) equilibrium calculations are carried out for each shell to establish the composition gradient. The conservation equations are solved to give the burned gas temperature of the outmost reacting shell. The burned gas temperature of the previously burned shells is revised to account for the effects of compression. The burned gas temperature is then known as a function of position and time as the flame progresses through the chamber.

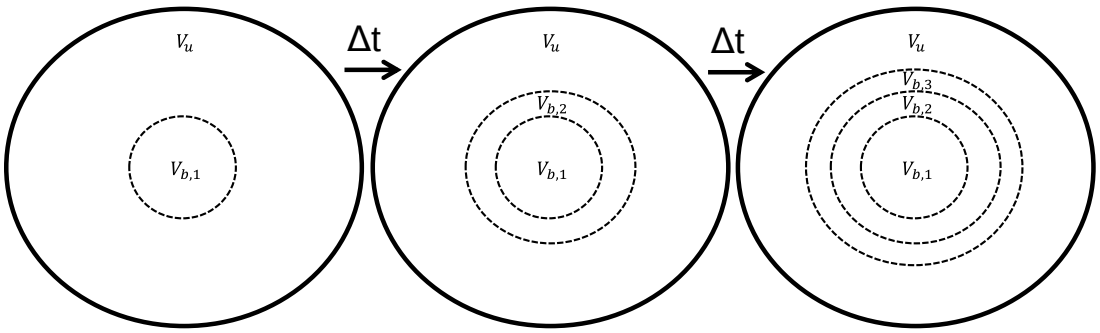

Figure 2.7: Illustration of the multi-zone thermodynamic model.

The linear, two-zone, and multi-zone models vary in complexity and require different amounts of time to run. There then exists a tradeoff between accuracy and computation time. To understand the tradeoffs, the present results are compared to results in literature to understand the impact of model selection on the accuracy of burning velocity calculations.

The linear model has been compared to more complex models with conflicting conclusions. Clarke [77] compared burning velocities derived from the linear model of Lewis and von Elbe [56] to those from the two-zone model of Metghalchi and Keck [48] and concluded that the linear model introduced minimal error, so long as the final pressure used was taken from a constant volume equilibrium calculation using the STANJAN package [78]. The error in the mass fraction of burned gas was found to be less than 1.6% when using the linear model. In contrast, Luitjen et al. [79] found that the linear model produced burning velocities that were up to 8% higher during early stages of combustion and up to 4% lower in during later stages when compared to results using the two-zone model. This finding was later suggested to be the cause of the differences in the measured CH_4-air burning velocities between the work of Dahoe et al. [60] (who used the linear model) and data in the literature (burning velocity values presented by Dahoe et

al. were 5-10% higher). Huzayyin et al. [61] found that the linear model produced burning velocities that were 7-10% higher than the values given by the two-zone model of Metghalchi and Keck [48]. The comparison performed in the present work, between the linear model and the two-zone model, showed similar findings to what was reported in refs. [61, 79]. The burning velocities of stoichiometric CH_4- and C_3H_8-air were found to be 12.9% and 10.4% higher when calculated with the linear model as opposed to the two-zone model.

Previous comparisons of a two-zone model and a multi-zone model are also available in literature. Early comparisons were done by Metghalchi and Keck [58], who showed that the incorporation of variable burned gas properties changed the calculated burned gas mass fraction by roughly 1%. Hill and Hung [59] performed a similar analysis and found that neglecting the burned gas temperature gradient had a negligible effect on burning velocity. Saeed et al. [74] developed a multi-zone model and compared methanol-air burning velocities to the results of Metghalchi and Keck [58]. The results at lean conditions were in good agreement but for rich flames, the burning velocities in ref. [48] were about 20% lower. The differences were not attributed to the model selection for post-processing; they were instead attributed mainly to the inclusion of cellular data [74]. Two-zone and multi-zone model results were compared in the present study and the difference in burning velocities given by the two methods was minimal for CH_4- and C_3H_8-air flames over a range of equivalence ratios.

Although the linear model required the least amount of computation time, it produced unsatisfactory results that were consistent with the higher values observed in previous publications using the same method. The two-zone and multi-zone models were

found to give similar results over the entire range of unburned gas temperature and pressure. Thus, the two-zone model was selected based on our findings, and the findings of previous studies [58, 59], which showed the inclusion of gradients to have a negligible effect on the burning velocity.

2.4 Data Reduction

Figure 2.8 shows a typical pressure trace (solid line) from an experiment (CH_4-air, Φ=1.0), along with T_b, T_u, and r_f, which are outputs of the two-zone model calculation. Only a portion of the pressure data is used for obtaining burning velocity, as denoted by the thick line on the pressure trace. For small R_f, the flame behavior is affected by flame stretch and the ignition process, and for large R_f, by heat losses to the walls and cellular instabilities; hence, typically only the central 75 % of the pressure data are used in the present study. Spherically propagating flames are subject to stretch rates inversely proportional to the flame radius [80],

$$K = \frac{2}{R_f}\frac{dR_f}{dt} \tag{2.24}$$

where K is the stretch rate and dR_f/dt is the flame front velocity Figure 2.8 also shows the stretch rate for this experiment. To reduce stretch effects (as well as the transient caused by the ignition), data are neglected for small flame radii, R_f<3.8 cm (i.e., R_f<R/2, as proposed by Elia et al. [76], and adopted by others [53, 65, 74]). For R_f/R=0.5, stretch rates range between 110 s^{-1} for uninhibited stoichiometric CH_4-air and 20 s^{-1} for inhibited cases with burning velocities near 5 cm/s. To avoid the effects of heat losses to the walls, only data up to dP/dt_{max} (i.e., the inflection point in the $P(t)$ curve in Figure 2.8) are used, following the recommendations in refs. [61, 81].

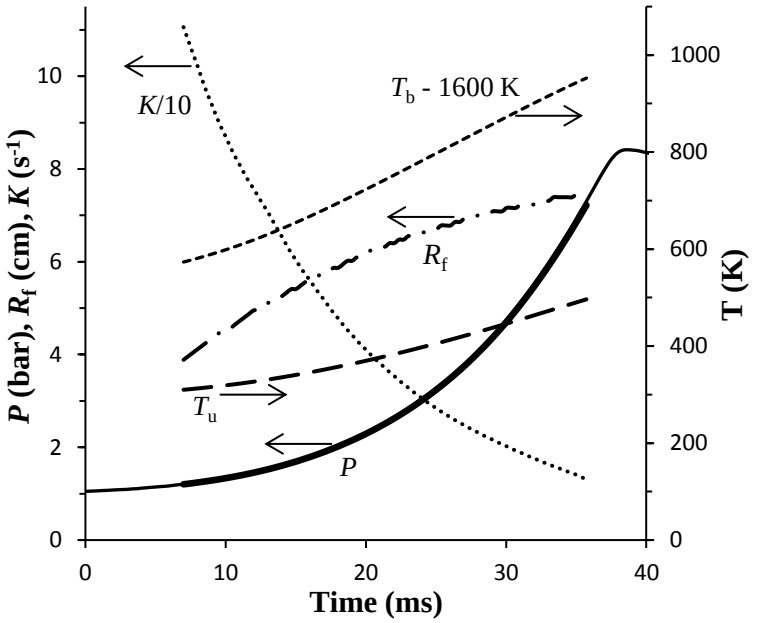

Figure 2.8: Experimental pressure trace (*P*), flame radius R_f, and gas temperature (unburned T_u and unburned T_b) as a function of time.

A single experiment provides burning velocity data for a range of pressure and temperature of the unburned gas, and these data are fit to the equation [33]:

$$S_u = S_{u,0}\left(\frac{T}{T_0}\right)^{\alpha}\left(\frac{P}{P_0}\right)^{\beta} \tag{2.25}$$

in which S_u is the laminar burning velocity, P_0 is the initial pressure, T_0 is the initial temperature, $S_{u,0}$ is the laminar burning velocity at the initial conditions; α, β, and $S_{u,0}$ are the fitting parameters. In the experiments performed, T_0 is 296 ±2 K, and P_0 is 0.87 bar, 1 bar, and 1.13 bar, (to provide more data for the curve fit). Individual tests were repeated twice for each initial pressure and the raw data from each test was included in the fitting to Eq. 2.25.

Figure 2.9 shows the burning velocity of stoichiometric CH_4-air as a function of unburned gas temperature and chamber pressure. The surface is the fit following Eq.

2.25, and the blue data points (and lines through them) are the S_u values at each combination of unburned gas pressure and temperature for a specific run, to which Eq. 2.25 is fit. In discussions following, S_u is presented at ambient conditions and under compressive heating, as obtained from Eq. 2.25 (and shown as red dots in Figure 2.9). Note that the presented results are interpolations, or small extrapolations, from the experimental data in Figure 2.9.

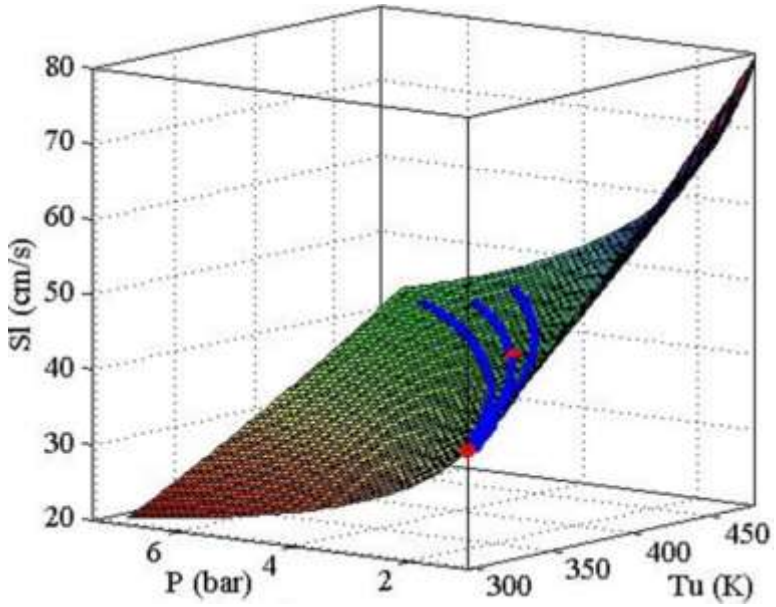

Figure 2.9: Three dimensional plot of burning velocity as a function of pressure and unburned gas temperature. The blue dots represent the data from six experiments, two of which are performed at each initial pressure. The surface represents the fitted results using Eq. 3.25 and the red dots are the reported S_u at ambient (T_0=298 K, P_0=1 bar) and compressed (T_0=400 K, P_0=3 bar) conditions.

In the present method, spherical flame propagation is a critical condition for accurate determination of S_u from the pressure trace. Buoyancy can distort the shape of the flame, especially for slow burning mixtures (which are of particular interest in the

present work). Takizawa et al. [47] estimated the minimum burning velocity measurable without error associated with buoyancy. Experiments were carried out in a spherical chamber using the pressure rise to determine burning velocity. Separate experiments were performed in a cylindrical chamber with visual access. The shape of the flame front was recorded with high speed video and the burning velocity was calculated using the constant-pressure method [82, 83]. As recommended by Pfahl et al. [84], to minimize the effects of buoyancy, the rate of change of the flame radius with respect to time was traced in the two horizontal directions. Results [47] showed that burning velocities as low as 6 cm/s could be measured with the constant-volume method.

In the present work, cellular instabilities, which also invalidate the smooth spherical flame assumption, are monitored through inspection of the S_u data of individual test runs. When cellular instabilities form, the flame surface becomes wrinkled and increases in area. The flame no longer propagates in the direction normal to a sphere at every location and the consumption rate of unburned gas increases due to the larger flame area. The faster mass burning rate creates a faster pressure rise which can lead to overestimations in S_u from the pressure trace [74]. The onset of cellular instabilities is typically detected via a distinct acceleration by the flame front as the pressure continues to increase [53, 74], and these data (if occurring) are omitted during the experimental data fitting.

2.5 Uncertainties

Individual uncertainty components and root-sum-of-squares (RSS) components are determined based on the procedure outlined in ref. [85]. Uncertainties in the measured

parameters are presented as expanded uncertainties $k_c u_c$ from a combined standard uncertainty (estimated standard deviation) u_c, and a coverage factor k_c=2 (level of confidence approximately 95%). Relative uncertainties $k_c u_c/X$ are reported, with X being the measured value of the parameter under consideration.

With the constant-volume method, the experimentally reported burning velocity is not measured directly. Instead, it is determined from the instantaneous pressure measurement and the initial temperature and pressure. With the root-sum-of-squares method (also known as the law of propagation uncertainty), individual measurement uncertainties are considered along with the sensitivity of the burning velocity to changes in the measured parameters. The combined standard uncertainty, taken as the estimated standard deviation of the result y (S_u), is determined from,

$$u_c(S_u) = \left[\sum_{i=1}^{N} \left(\frac{\delta S_u}{\delta x_i}\right)^2 u^2(x_i)\right]^{1/2} \tag{2.26}$$

where $u(x_i)$ is the uncertainty of each input estimate x_i and $\delta S_u/\delta x_i$ is the change in the burning velocity associated with a change in an input estimate value.

Uncertainties in initial temperature and pressure, dynamic pressure rise, agent volume fraction, equivalence ratio, and burning velocity calculation and fitting to Eq. 2.25 are considered. The expanded relative uncertainties related to reactant mixture preparation are 1.0% for the equivalence ratio, 0.3% for the volume fraction of air, and 0.8% for the volume fraction of CH_4. Uncertainty in the volume fraction of inhibitor ranged from 4% at low concentrations (X_a=0.01) to <1% at higher concentrations (X_a=0.05). Relative uncertainties for the dynamic pressure rise, initial pressure, and initial temperature are 1.3%, 0.7%, and 1.0% respectively.

With the individual measurement uncertainties specified, the next step is to estimate how perturbations in the measured parameters influence the burning velocity (i.e., estimate the sensitivity coefficients $\delta S_u/\delta x_i$). To examine the uncertainty in the dynamic pressure rise, the thermodynamic model that is used to determine S_u was run again, for a select number of tests, with the pressure trace shifted higher/lower by the measurement uncertainty. The shift was found to have minimal influence on the reported burning velocity. The uncertainty in S_u from the empirical fit was examined by considering the R-squared values of each fit and by re-fitting with modified fitting parameters. The change in the fitting parameters within the fitting uncertainty was also found to have minimal impact. The main parameters influencing the reported burning velocity are the initial temperature and pressure, the mixture equivalence ratio, and the inhibitor concentration, with the latter determined from pressure measurements (i.e. the partial pressure method).

With the present experiment, numerous tests are performed for a given reactant mixture and Eq. 2.25 is fit to the resulting dataset to provide a relationship between S_u and T_i and P_i. Therefore for each reactant mixture, the empirical fit can be used to estimate the change in S_u as the initial conditions change. The same approach is used to estimate the change in S_u as the initial equivalence ratio changes. In this case, the empirical relationship is taken from the work of Takizawa et al. [47] who performed burning velocity measurements of CH_4-air mixtures using the same experimental technique. In ref. [47] the data was fit with an additional parameter so that S_u could be found as a function of Φ, T_i, and P_i. Several other researchers have fit experimental data with similar equations, but as seen in the next section, the burning velocity results of ref.

[47] are most similar to the present results, influencing our selection. The empirical equations used in ref. [47] to show the dependency of S_u on Φ, T_i, and P_i are:

$$S_u = S_{u,0}\left(\frac{T}{T_0}\right)^{\alpha}\left(\frac{P}{P_0}\right)^{\beta} \tag{2.27}$$

$$S_{u0} = S_{u0,max} + s_1(\Phi - \Phi_{max})^2 + s_2(\Phi - \Phi_{max})^3 \tag{2.28}$$

$$\alpha = a_1 + a_2(\Phi - 1) \tag{2.29}$$

$$\beta = b_1 + b_2(\Phi - 1) \tag{2.30}$$

where, $S_{uo,max}$, s_1, s_2, a_1, a_2, b_1, and b_2 were determined by fitting the equation to the experimental data (note that Eq. 2.27 is identical to Eq. 2.25 used in the present study to fit the experimental data). The fitting parameters for CH_4-air, given in ref. [47], are shown in Table 2.2.

Table 2.2: Fit parameters for the burning velocity of CH_4-air at different Φ, T_i, and P_i [47].

Composition	S_{u0} (cm/s)				α		β	
	$S_{u0,\,max}$	s1	s2	Φ_{max}	a_1	a_2	b_1	b_2
CH_4	36.5	-217	-180	1.07	1.88	-0.095	-0.36	-0.13

Lastly, the sensitivity of S_u to the inhibitor concentration is estimated from the experimental data as done for T_i or P_i. For a given initial equivalence ratio, tests are typically performed with increasing inhibitor concentration until $S_u \leq 6$ cm/s. The data is then fit with a third order polynomial to estimate S_u resulting in changes in X_a on the order of the measurement uncertainty (note that we are not interpolating far from the measured data). A standard empirical relationship cannot be used (as is done for changes in Φ, Ti, and Pi) because added agent influences burning velocity in a number of ways depending on the concentration and the initial stoichiometry. Through consideration of

the above-mentioned sources of uncertainty, the maximum expanded relative uncertainty (ku_c/X) for the reported experimental burning velocities is 12%.

2.6 Experimental Validation

To validate the accuracy of the experimental facility and the post-processing procedure, the burning velocity of CH_4-air flames was determined over a range of equivalence ratios (0.6 to 1.3). Figure 2.10 compares the present results to published data at standard (298 K, 1 bar; lower curve) and compressed (400 K, 3 bar; upper curve) conditions. The solid black squares show the present data, other black symbols show data from researchers using the same experimental technique [47, 49], blue symbols show stretch corrected data using spherical flames [86-88], and red symbols show stretch-corrected data from counter-flow flames [89, 90].

For the initially ambient mixtures, the burning velocities are in excellent agreement with previous results using the constant-volume method with a similarly sized chamber and a two-zone model [47]. Values are within 1% at all equivalence ratios except for Φ=0.7 and Φ=1.2 where S_u is 5% higher and 3% lower, respectively (The symbols in Figure 2.10 representing the data of ref. [47], are not visible because they are so closely aligned with the larger square symbols showing the present data). Results are within 5% of ref. [49], except at Φ=1.2 where S_u is 8.5% lower. Burning velocities are also in satisfactory agreement with stretched-corrected spherically propagating [86-88] and counterflow [89, 90] flame data, within the scatter of reported values for the entire range of Φ.

The upper set of symbols in Figure 2.10 compares burning velocities at the compressed conditions with previous results using the same constant-volume method. The present burning velocities are in excellent agreement with the results of Stone et al. [49] and in satisfactory (±9%) agreement with Takizawa et al. [47, 49]. Overall, the CH_4-air validation results show that the present experimental approach provides burning velocities in agreement with those of other investigations at standard and compressed (400 K, 3 bar) conditions.

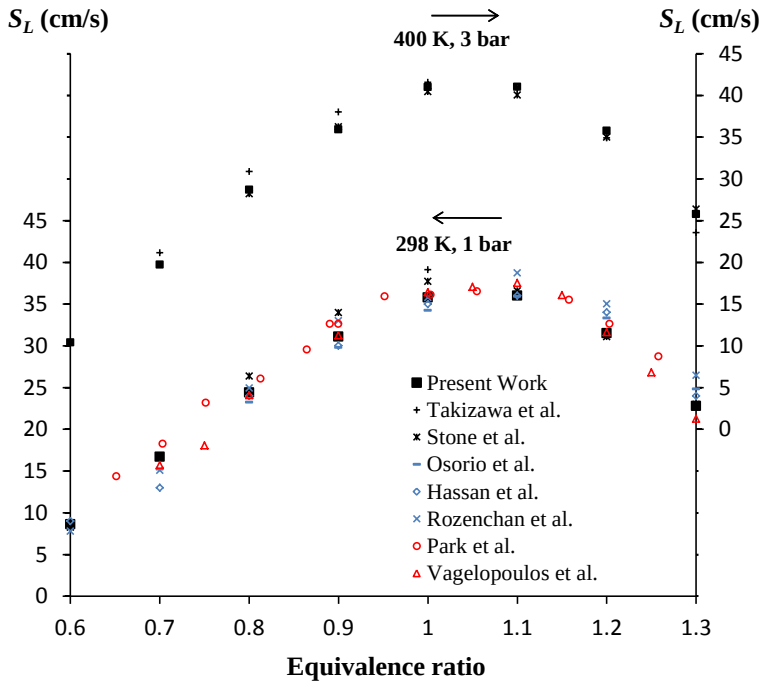

Figure 2.10: Burning velocity of premixed CH_4-air flames at 298 K and 1 bar (lower) and 400 K and 3 bar (upper) as a function of equivalence ratio, together with previously published results.

For additional validation, the burning velocity of C_3H_8-air flames was determined over a range of equivalence ratios (0.7-1.4). Figure 2.11 compares the present results to published data at standard (298 K, 1 bar; lower curve) and compressed (400 K, 3 bar;

upper curve) conditions. Like the CH_4-air validation figure, solid black squares show the present data, other black symbols show data from studies using the same experimental technique [47, 48], blue symbols show stretch corrected data using spherical flames [88, 91], and red symbols show stretch-corrected data from counter-flow flames [90, 92].

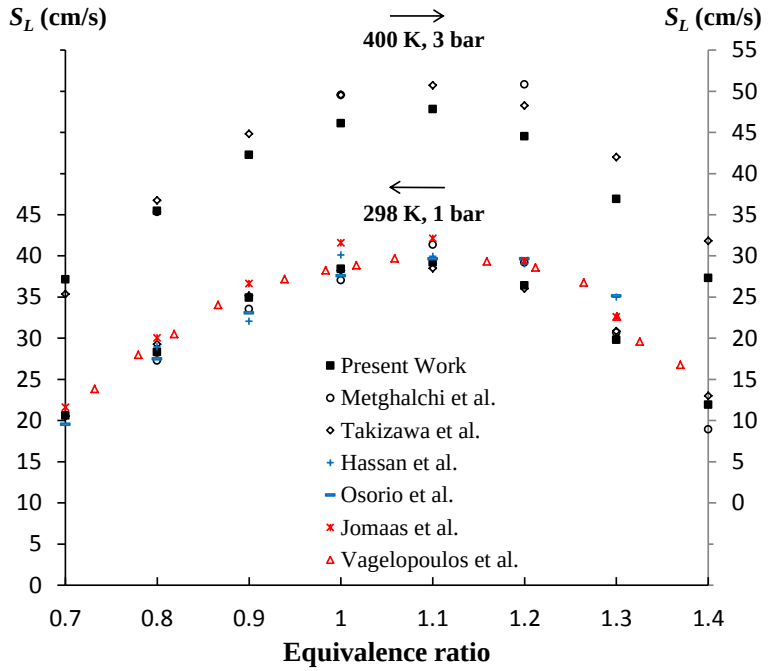

Figure 2.11: Burning velocity of premixed C_3H_8-air flames at 298 K and 1 bar (lower) and 400 K and 3 bar (upper) as a function of equivalence ratio, together with previously published results.

The C_3H_8-air burning velocities are within the scatter of previously reported data in the literature, as observed for the CH_4-air burning velocities. At lean conditions, the present data are near the center of the scatter. At stoichiometric conditions, data are most similar to the measurements of Takizawa et al. [47] and Vagelopoulos et al. [90] but lower than the reported values of Jomaas et al. [92] by 7.5%. At rich conditions, the results are on the lower end of the scatter and are most similar to data measured using the

same technique. At 400 K and 3 bar the burning velocity results for C_3H_8-air are in lesser agreement with the previously reported date using the same technique. At lean conditions, agreement is better, but at richer conditions the present data is roughly 10% lower than the other reported burning velocities.

Chapter 3: 30 L Chamber Experiment and Numerical Methods

3.1 Introduction

A larger 30 L spherical chamber experiment was built as an alternative method for measuring the laminar burning velocity of premixed flames. The experimental method is most often referred to as the spherically expanding constant pressure method (as opposed to the constant volume method performed in the 1.85 L experiment). It is called the constant pressure method because flame propagation is studied during the early stages when the chamber pressure is nearly constant, thus the need for a larger chamber. Therefore, the flame propagation rate is not affected by changes in the unburned gas pressure and temperature. Instead, the propagation rate is solely a function of the flame stretch rate, which varies as the flame radius changes, and extrapolation to zero-stretch conditions can be performed for improved comparison with 1-D flame model predictions. In this chapter an overview is also provided for the numerical methods used to predict equilibrium conditions and planar flame burning velocities.

3.2 30 L Chamber Experiment

3.1.1 Apparatus and Instrumentation

Experiments are performed in a 30 L stainless steel spherical vessel (shown in Figure 3.1) that is similar to the design used in previous studies [91, 93-95]. The chamber has an inner diameter of 38 cm, wall thickness of 0.635 cm, and is equipped with vertical electrodes, an absolute pressure gauge, a dynamic pressure sensor, a

thermocouple, and a mixing pump. The chamber has two polycarbonate windows (10.2 cm in diameter and 2.54 cm thick) diametrically opposed along the centerline of the chamber, allowing visual access.

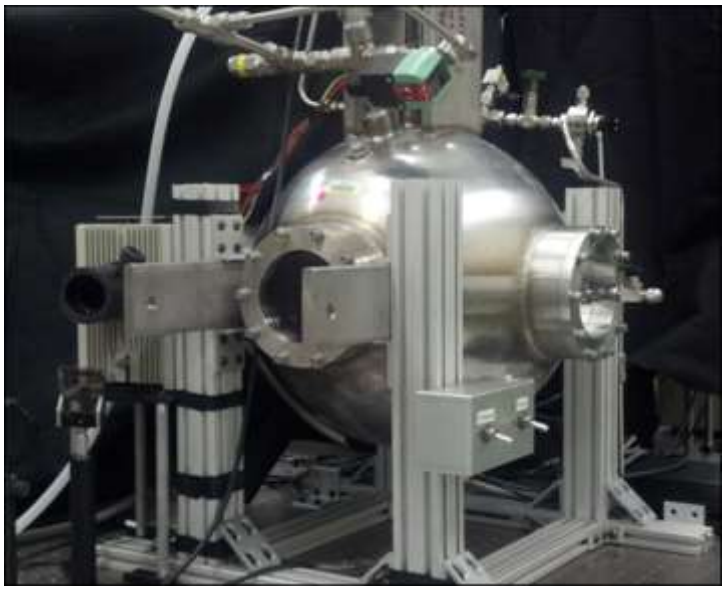

Figure 3.1: Image of the 30 L experiment.

Reactant mixtures are prepared in the chamber by first reducing the pressure below 100 Pa with a vacuum pump (Alcatel rotary vane). Reactants are then added in order of smallest to largest concentration using the method of partial pressures; reactant partial pressures are monitored with an Omega PX409 absolute pressure transducer that is periodically calibrated against a Baratron 627D pressure gage (claimed accuracy of 0.12% of reading). Liquid suppressants ($C_3H_2F_3Br$) are added using a syringe and leak free septum that is separated from the chamber by a ball valve. The mass of each liquid is checked with a Mettler PE 360 digital scale (0.001g resolution) to ensure the desired partial pressure is met. The entire mixture is circulated for 3 minutes with a Parker Hannifin metal bellows pump (~8 volume changes), then given 10 minutes to settle. The

sample reactants are CH_4 (Matheson Tri-Gas, 99.97% purity), C_3H_8 (Scott Specialty Gases, 99.0% purity), CF_3Br (Great Lakes Chemical Corp., 99.6% purity), and $C_3H_2F_3Br$ (American Pacific Corp., > 99% purity). The in-house compressed air is filtered, dried, and conditioned with a 0.01 μm filter, a carbon filter, and a desiccant bed to remove small aerosols, organic vapors, and water vapor. The relative humidity of the air is less than 2% for all tests according to measurements with a humidity gage (TSI Velocicalc 8386), and the same reactant gases as outline in the experimental section for the 1.85 L chamber are used. A schematic diagram illustrating the 30 L chamber gas handling system is shown in Figure 3.2.

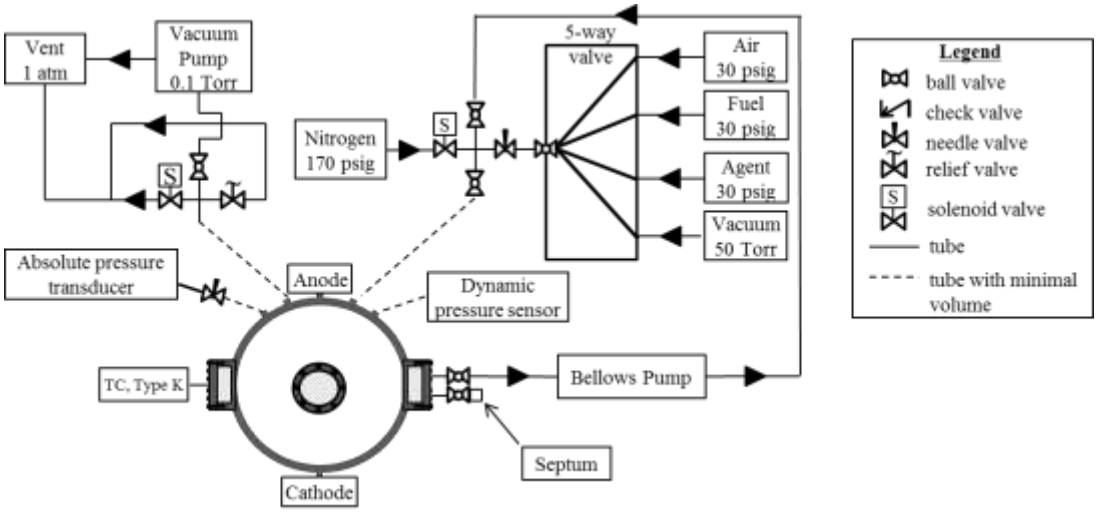

Figure 3.2: Schematic diagram of the 30 L experiment showing the gas handling system.

Vertically oriented tungsten electrodes with a diameter of 0.8 mm (recommended in ref. [96]) form a 2 mm gap in the center of the chamber. Combustion is initiated via an electrical spark generated by a capacitive discharge circuit similar to that of ref. [51]. An Acopian power supply (1-15 kV) charges interchangeable capacitor banks (1-100 nF), providing variable ignition energies estimated to range from 0.05 mJ to 500 mJ. For most

tests, the ignition energy is gradually increased until propagation occurs, ensuring the deposited energy is within an order of magnitude of the minimum value. For certain test mixtures containing suppressant, higher ignition energies are required for the flame to propagate through the entire viewing window because of the competing effects of stretch and the energy supplied during ignition [97] (further discussion is provided in the results section). When applying near-minimum ignition energies, a well-established flame forms and quickly extinguishes. Thus, for certain mixtures, multiple tests are performed with increasing ignition energy until the critical radius, such as defined in [97], is reached, hence ensuring sustained flame propagation.

During each test, a dynamic pressure sensor (PCB Piezotronics, 101A06; claimed accuracy of 0.1% of reading) records the instantaneous pressure. Once a test is finished, the chamber is quickly vented and purged with nitrogen to reduce heat transfer from the products gases to the chamber. External fans cool the chamber to ambient temperature (296±3 K) while it is purged with air and subject to vacuum repeatedly to ensure all products are removed before the next run.

A z-type shadowgraph system, illustrated in Figure 3.3 and based on the recommendations of Settles [98], creates a shadow image of the flame, highlighting variations in the second derivative of the index of refraction. A 100 W mercury lamp creates a diverging beam that reflects off a parabolic mirror (f = 940 mm) creating a collimated beam that passes through the chamber. The beam then reflects off an identical parabolic mirror toward a Phantom v7.0 high-speed camera equipped with a Nikkor lens (f = 135 mm). Flame propagation is recorded at a maximum frame rate of 7200 frames/s

and with a spatial resolution of 143 μm. For illustration, Figure 3.4 shows the recorded shadowgraph images of a stoichiometric CH_4-air flame with CF_3Br added at X_a=0.01.

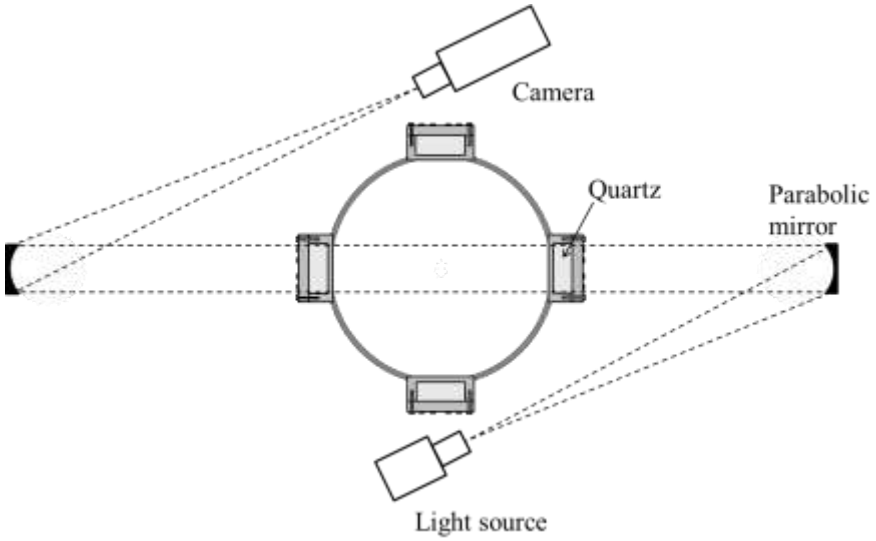

Figure 3.3: Z-type shadowgraph setup.

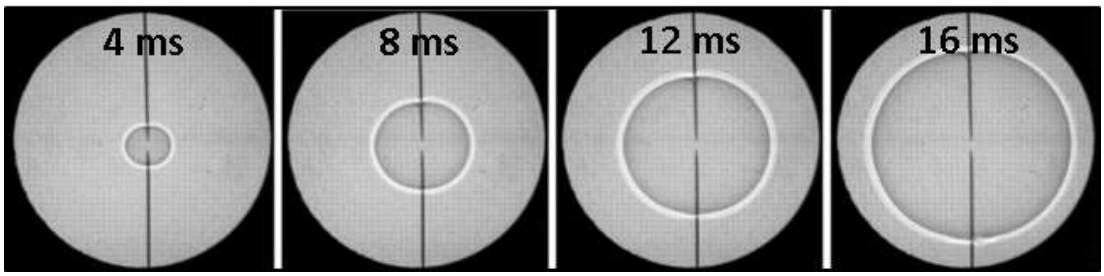

Figure 3.4: Shadowgraph images of stoichiometric CH_4-air flame propagation.

The experiment is controlled with LabView, and the high-speed camera interfaces with standalone software provided by the manufacturer. The triggering is provided using a DAQ to ensure proper timing between the ignition, camera initiation, and pressure measurement.

3.2.2 Data Reduction

Image analysis software (developed in-house) tracks the flame positon as the location of maximum positive gradient in light intensity when approaching the outer edge from the center (i.e. the hot gas boundary of the flame sheet [82]). For slow burning flames, which are of interest in the present study, the influence of buoyancy is reduced by tracking the flame propagation in the horizontal direction only, like done in previous studies measuring burning velocity of NH_3-air-N_2O flames [84], near limit H_2-air flames diluted with passive fire suppressants [99, 100], and flames of halogenated hydrocarbon refrigerants in air [47]. The image analysis software reads in the .cine video file and tabulates radius location on the right and left side as a function of time.

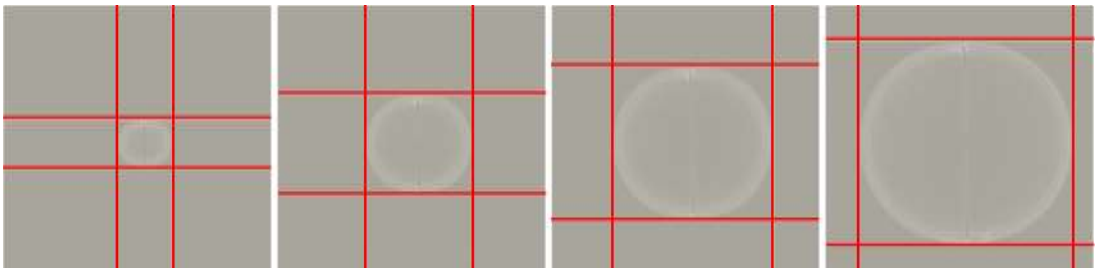

Figure 3.5: Illustration of flame front tracking.

Using recommendations provided in literature, the range of data considered during extrapolation is carefully selected to reduce measurement uncertainty. An upper bound on the flame radius R_{fU} for which data is considered during post-processing is required to reduce the influences of confinement, radiation, and flame instabilities. Numerical simulations of spherically propagating flames performed in ref. [46] showed that a maximum flame radius of up to 25% of the chamber radius results in a confinement-induced reduction in S_u^0 of less than 3%. With the present experimental

apparatus, 25% of the chamber radius corresponds to a flame radius of 4.75 cm. In addition to confinement effects, previous studies have shown radiation to be most influential at large flame radii, especially for slow burning flames [100-102]. In the present study, inhibited mixtures burn slowly and create product gases with high levels of emissivity [103]. Therefore, only data up to a flame radius of 3 cm are considered to minimize confinement *and* radiation effects. Moreover, omitting data above 3 cm ensured the extraction of S_u^0 was unaffected by preferential diffusion and hydrodynamic instabilities for all test mixtures considered.

A lower bound on the flame radius R_{fL} is also considered to reduce the influence of ignition and nonlinear stretch effects during the early stages of propagation. In the present study, R_{fL} varied between 0.5-1.5 mm for all tests, and was dependent on the reactant mixture. Data at small flame radii (R_{fL}=0.5 mm) were considered for mixtures with near unity Lewis numbers and with moderate flame speeds (20-40 cm/s) which were ignitable and capable of propagating throughout the entire viewing window when subject to near-minimum ignition energies. For inhibited, near-limit cases requiring additional ignition energy for sustained propagation (above the amount that lead to early propagation and extinction), a larger minimum flame radius was considered to reduce inaccuracies caused by overdriven ignition. The flame radius for which ignition disturbances are negligible was found to range between 0.6-1.1 mm in previous investigations [102, 104-106]. A range exists because the radius depends on the specific reactants and ignition energy range considered. In the present study, the highly inhibited mixtures often required ignition energies that were several orders of magnitude above what was required to ignite the uninhibited mixtures, hence a more conservative

minimum R_f of 1.5 mm was considered. Furthermore, inhibited mixtures can have Lewis numbers that are far from unity (as discussed in the results section). For mixtures with large *Le* (large L_b), the nonlinear stretch behavior that occurs at small flame radii should not be included during extrapolation [102, 106]. By using 1.5 mm as the lower radius bound, data affected by the extreme non-linearity during the early stage of propagation are omitted during extrapolation.

The burned gas velocity of a spherically propagating flame corresponds to the observed flame velocity by assuming the product gases are motionless because of symmetry. The burned gas velocity is therefore the temporal derivative of the flame radius, $S_b = dR_f / dt$ and is solely a function of the stretch rate during the constant pressure portion of flame propagation. Stretch is defined as the temporal derivative of a flame surface element; the general and configuration specific forms are as follows,

$$\boldsymbol{K = \frac{1}{A_f}\frac{dA_f}{dt} = \frac{2}{R_f}\frac{dR_f}{dt}} \tag{3.1}$$

where K is the stretch rate (s^{-1}) and A_f is the flame surface area and t is time. As seen in Eq. 3.1, the stretch rate decreases as the flame radius increases (the curved flame surface asymptotically approaches the planar, one-dimensional flame configuration). From conservation of mass across the flame sheet, the unburned gas velocity is given in Eq. 3.2,

$$\boldsymbol{S_u = \frac{\rho_b}{\rho_u} S_b} \tag{3.2}$$

where the burned gas is assumed to be in chemical equilibrium and the density is taken from a constant-pressure, constant-enthalpy calculation using the CEA2 routine of Gordon and McBride [69].

Figure 3.6 presents the experimentally determined burned gas velocity versus stretch rate for a stoichiometric CH4-air test. Data points on the right experience high stretch rates during the early stages of propagation when the flame radius is small. For this case, the burned gas velocity increases as the stretch rate decreases (flame radius increases) until the trend suddenly reverses at a stretch rate of about 200 s^{-1}. The reverse is caused by an increase in pressure within the chamber and is not a consequence of the further reduction in stretch rate. Thus these points are not considered during extrapolation and the points that are included are bracketed by the dotted vertical lines in Figure 3.6.

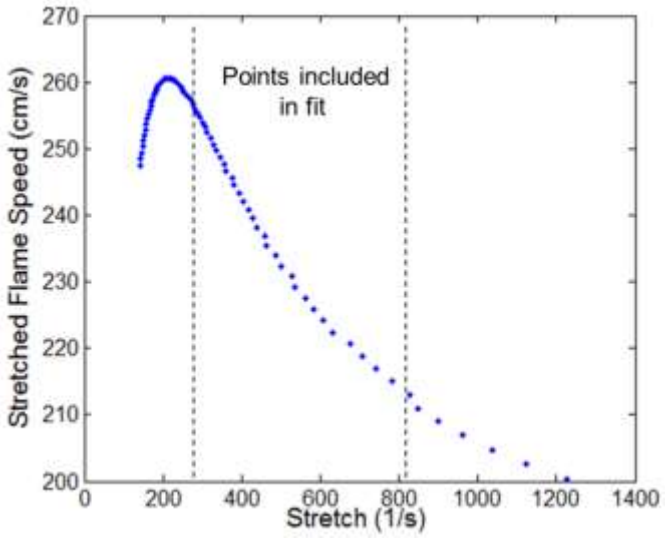

Figure 3.6: Burned gas velocity versus stretch rate for stoichiometric CH4-air.

3.2.3 Extrapolation Methods

The present experiment provides the burned gas velocity over a range of stretch rates. For model validation purposes, the unstretched burning velocity is of interest and can be compared to numerical simulations of planar 1-D flame speeds. Therefore, the

measured burning velocities are extrapolated to unstretched conditions (i.e., infinitely large flame radius) corresponding to the planar conditions. We use the linear relationship between burning velocity and stretch rate first reported by Markstein [107] and later expressed in the present form by Clavin [108],

$$S_b = S_b^o - L_b K \tag{3.3}$$

where $S_b^{\,0}$ is the unstretched burned gas velocity and L_b is the burned gas Markstein length. The model was derived for weakly stretched flames with near unity Lewis number *Le*, and has been used extensively in the literature. For the present inhibited mixtures, there is no current method for estimating *Le*. Correlations exist for bi-component fuel mixtures [109], but none can be reliably applied to a fuel-suppressant-air mixture because a major assumption in each correlation is that the two fuels only react with the oxidizer and not each other [109]. This is clearly not the case for the chemically active suppressants which react with the decomposition products of the fuel to reduce radicals; additionally, suppressants can act as a both a fuel and/or an oxidizer [71]. Nonetheless, we assume that *Le* will change considerably when large molecule suppressants are added to fuel-oxidizer mixtures. Therefore, non-linear extrapolation is also performed using the relationship derived by Ronney and Sivashinsky [110] (for highly stretched flames with large *Le*) and later proposed for use by Kelley et al. [111],

$$\left(\frac{S_b}{S_b^0}\right)^2 ln\left(\frac{S_b}{S_b^0}\right)^2 = -2\frac{L_b K}{S_b^0} - 2\frac{L_b}{S_b^0}\frac{dS_b}{dR_f} \tag{3.4}$$

Eq. 3.4 is similar to the most commonly used non-linear extrapolation equation suggested during earlier work by Kelley et al. [112],

$$\left(\frac{S_b}{S_b^0}\right)^2 \ln\left(\frac{S_b}{S_b^0}\right)^2 = -2\frac{L_b K}{S_b^0} \tag{3.5}$$

differing only by the inclusion of an acceleration term that appears when the quasi-steady approximation is lifted. Using direct numerical simulation of spherically propagating fames, Chen [113] showed that extrapolating with Eq. 3.5 results in significant error in the unstretched laminar burning velocity when the mixture *Le* is large. Kelley et al. [111] later suggested that the error was the result of using the quasi-steady approximation, which is applicable only for flames with large radii. Therefore, including the acceleration term (last term on the right in Eq. 3.4) is necessary when extrapolating unstretched data from mixtures with large *Le*. It should be noted that while the non-linear methods generally provide more accurate results compared to the linear method, Wu et al. [114] recently showed that none of the existing extrapolation methods capture the true non-linear relationship between flame speed and stretch rate when *Le* is considerably lower than unity (L_b is negative). Thus, we use the non-linear method in Eq. 3.4 and provide the raw experimental data of flame radius versus time in the supplementary material so that the data may be either re-examined (if a more accurate non-linear correlation is determined) or compared to direct numerical simulation of spherically expanding flames (as suggested by ref. [37]).

Eq. 3.6 presents the expanded form of Eq. 3.4.

$$\frac{S_b}{S_b^0}\left[1 + \frac{2L_b}{R_f} + \frac{4{L_b}^2}{{R_f}^2} + \frac{16{L_b}^3}{3{R_f}^3} + o^4\left(\frac{L_b}{R_f}\right)\right] = 1 \tag{3.6}$$

The expanded form is used (as suggested in ref. [111]) to eliminated the difficulties associated with applying Eq. 3.4, which is numerically unstable. The final step to reduce

uncertainty is to use the integrated forms (Eq. 3.7 and Eq. 3.8) to eliminate the numerical differentiation, as done in [82, 111, 115],

$$R_f = S_b^0 t - 2L_b \ln R_f + c \tag{3.7}$$

$$S_b^0 t + c = R_f + 2L_b \ln R_f - 4\frac{L_b^2}{R_f^2} - \frac{8}{3}\frac{L_b^3}{R_f^3} \tag{3.8}$$

where the variable c in both equations is an integration constant. The variables S_b^0, L_b, and c are determined using a non-linear least squares optimization routine that fits Eq. 3.7 and Eq. 3.8 to the experimentally measured flame radius versus time $R_f(t)$. Figure 3.7 shows the linear and nonlinear fits applied to the stoichiometric CH_4-air case. The y-intercept provides the unstretched burned gas velocity, which is always less when using the nonlinear fit.

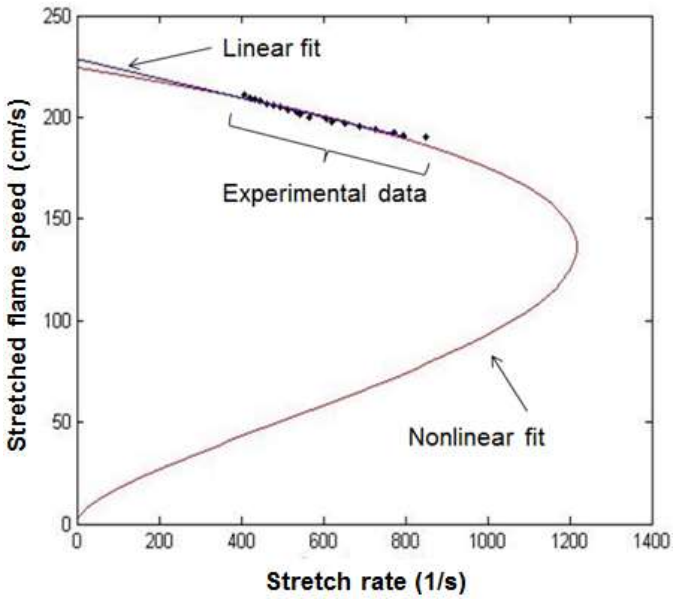

Figure 3.7: Linear and nonlinear extrapolation fits applied to the burned gas velocity of a stoichiometric CH_4-air flame.

Tests are performed at 296±2 K and 760 Torr and are repeated 2 times for each mixture. For each test, the extrapolation equations are fit to the *Rf* vs. *t* data from the left and right side flame tracking locations. The fitting parameters (S_b^0, L_b, and c) from the two sides are then averaged. Lastly, the results of the multiple tests are averaged to produce the burning velocities and burned gas Markstein lengths reported in the present study.

3.2.4 Uncertainties

The uncertainties in experimental burning velocity is reported as expanded uncertainties $U=k_c u_c$ determined from a combined standard uncertainty u_c and a coverage factor $k_c=2$ corresponding to a level of confidence of 95%. The combined standard uncertainty is determined using the root-sum-of-squares (RSS) method of combining individual uncertainty components, as outlined in ref. [85]. The uncertainty in the reported data is caused by uncertainties in the measured flame radius versus time, initial temperature, initial pressure, mixture equivalence ratio, and the inhibitor concentration. Considering the 70 pixels/cm resolution and the high clock accuracy of 50 ppm, the uncertainty in the flame front tracking causes negligible uncertainty in the reported data. The uncertainty in initial temperature and the initial pressure are 3 K and 10 Torr; based on the findings in ref. [102], we estimate these uncertainties result in a 3% uncertainty in the reported burning velocity. By using a high accuracy transducer (claimed accuracy of 0.12% of reading) the uncertainties in equivalence ratio and agent volume fraction are 1.0% and 0.3%, resulting in an estimated uncertainty in burning velocity of 8%. Thus, the maximum expanded relative uncertainty ($k_c u_c/X$) in the reported burning velocity is

estimated to be 13%, occurring at lean conditions when the uncertainty in the equivalence ratio has the largest effect on the reported data.

Measurement uncertainty is not the only cause of inaccuracy in the reported data. Buoyancy, radiation, and non-linear stretch effects can cause the measured result to differ from the speed of a 1-D planar adiabatic flame or even the true speed of a spherically propagating flame (this is particularly important when comparing experimental data to numerical predictions). Higher inaccuracy exists for slow burning flames most affected by buoyancy and radiation. In addition, higher uncertainty is expected for mixtures with Lewis numbers far from unity (i.e. Le<<1 and Le>>1) because, for these highly non-equidiffusion mixtures, the extrapolation methods fail to capture the non-linearity between the burning velocity and stretch rate. While these influences cannot be eliminated in the present study, data was carefully selected during post-processing to reduce the effects, as detailed above.

In addition to estimating the measurement uncertainty using the root-sum-of-squares method, the two times the standard deviation of the reported S_u^0 and L_b from repeated tests is provided in Figure 3.8 and Figure 3.9 for CH_4-air and C_3H_8-air flames over a range of equivalence ratios. In each figure, the top frames give the linearly (right) and non-linearly (right) extracted Markstein lengths L_b along with the twice the standard deviation shown by the vertical bars. The bottom frames provide the same information for the linearly (left) and non-linearly (right) extrapolated S_u^0. In the present study, the standard deviation in S_u^0 and L_b is much lower when using the non-linear method. As shown by Chen [102], using different start and end radii can result in up to a 20%

difference in S_u^0 when using the linear method whereas the change in S_u^0 with radius range was much less with the non-linear method.

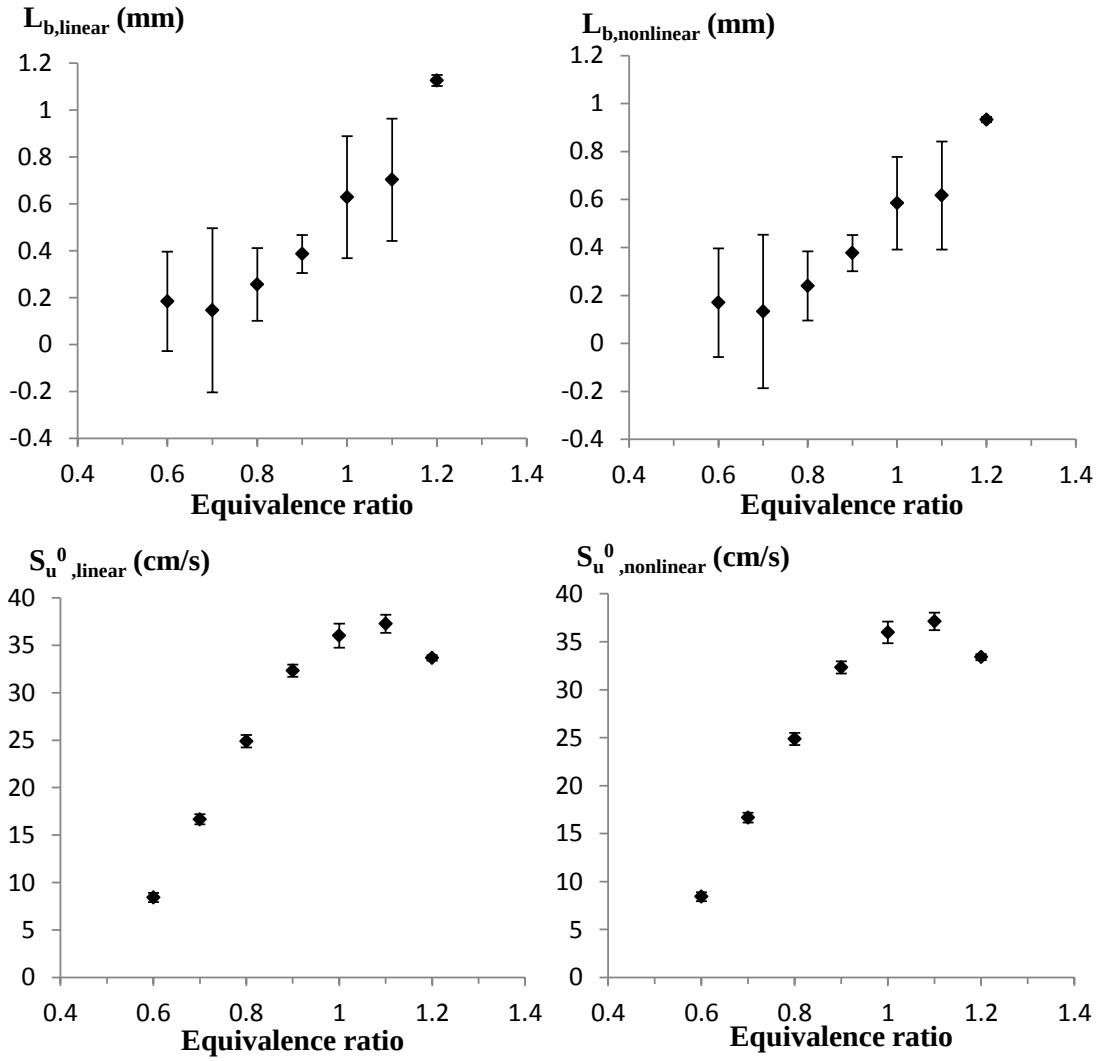

Figure 3.8: Uncertainty in S_u^0 and L_b for CH_4-air flames presented as two times the standard deviation.

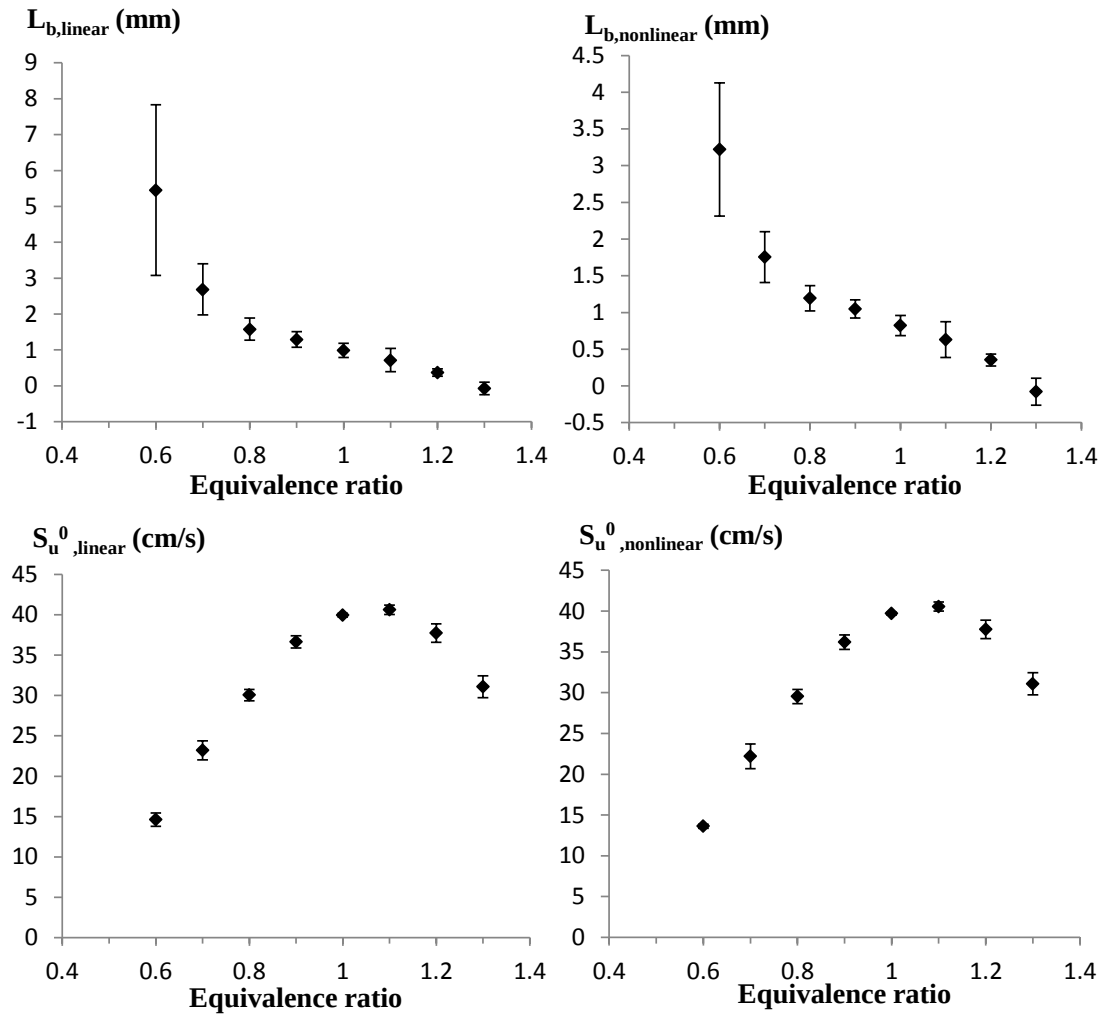

Figure 3.9: Uncertainty in S_u^0 and L_b for C_3H_8-air flames presented as two times the standard deviation.

3.2.5 Experimental Validation

To validate the new experiment, non-linearly extrapolated unstretched burning velocities S_u^0 of CH_4- and C_3H_8-air flames are determined over a range of fuel-air equivalence ratios and compared with data in the literature. (In the remaining sections, all reported unstretched burning velocities are non-linearly extrapolated, unless otherwise noted.) For illustration, the linear and non-linear fits to the calculated *dRf*/*dt* versus

stretch rate are shown in Figure 3.10 and Figure 3.11 respectively. Figure 3.12 compares the present CH_4-air ($0.6 \leq \Phi \leq 1.3$) measurements to spherically propagating flame data [86, 87, 105, 116], counterflow flame data [89, 90], and numerical predictions using the Wang mechanism [117]. Burning velocities are in excellent agreement with the previous results and agree well with predictions, except at $\Phi \leq 0.8$, where predictions are higher by about 10-25%. At lean conditions, previously determined experimental burning velocities are in general lower than the predictions, with the exception refs. [89, 116]. Subsequently, the discrepancy between S_u^0 from spherically propagating flames and numerical simulations was shown to be the result of radiative heat losses and confinement effects [118]. Thus, the agreement between the present data and previously published data show that the new experiment provides accurate burning velocity measurements for CH_4-air mixtures.

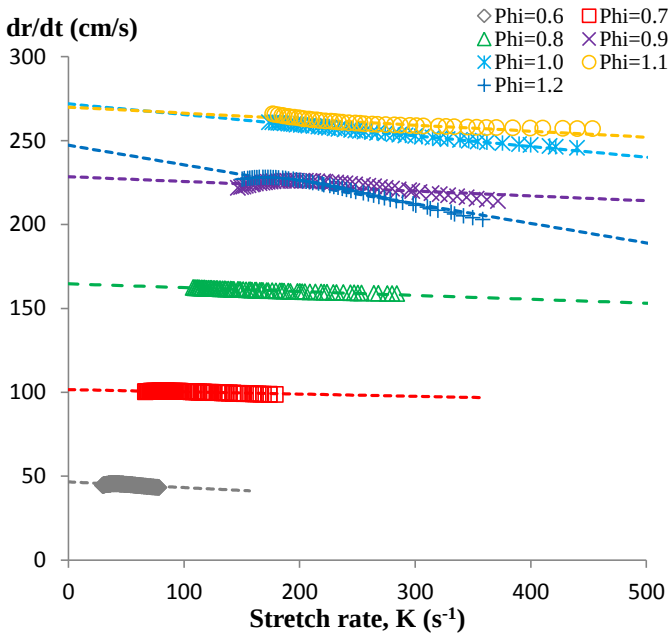

Figure 3.10: Burned gas velocity (S_b) of CH_4-air fit with the linear method.

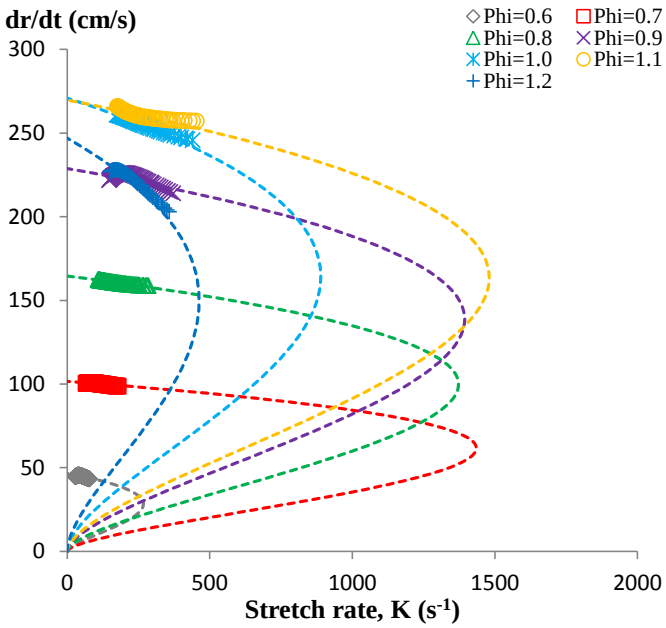

Figure 3.11: Burned gas velocity (S_b) of CH_4-air fit with the non-linear method.

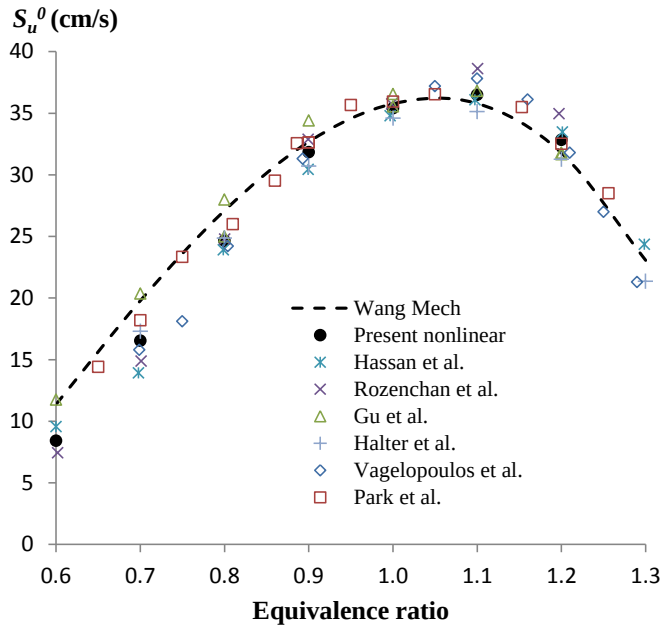

Figure 3.12: Burning velocity of premixed CH_4-air flames at 298 K and 1 bar (collected in 30 L chamber) as a function of equivalence ratio, together with previously published results and numerical predictions.

For reference, the linear and non-linear fits to the C_3H_8-air data are shown in Figure 3.13 and Figure 3.14. Figure 3.15 compares unstretched burning velocities for C_3H_8-air flames (over a similar range of Φ) with spherically propagating flame data [91, 92], counterflow flame data [90, 119], and heat flux method data [120], along with numerical predictions with the Wang mechanism [117]. At lean conditions, the present S_u^0 results are in excellent agreement with the previous experiments and with the numerical predictions. For rich conditions (Φ>1.0), the present data is on the lower end of experimental scatter, but most similar to the model predictions.

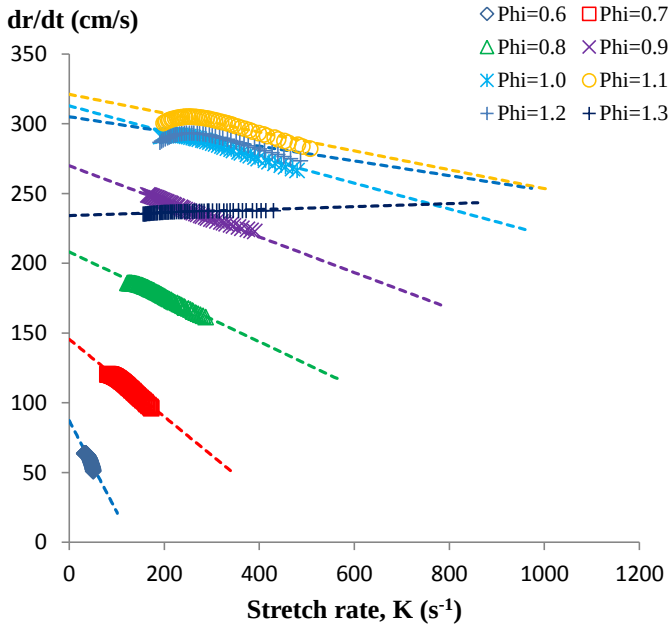

Figure 3.13: Burned gas velocity (S_b) of C_3H_8-air fit with the non-linear method.

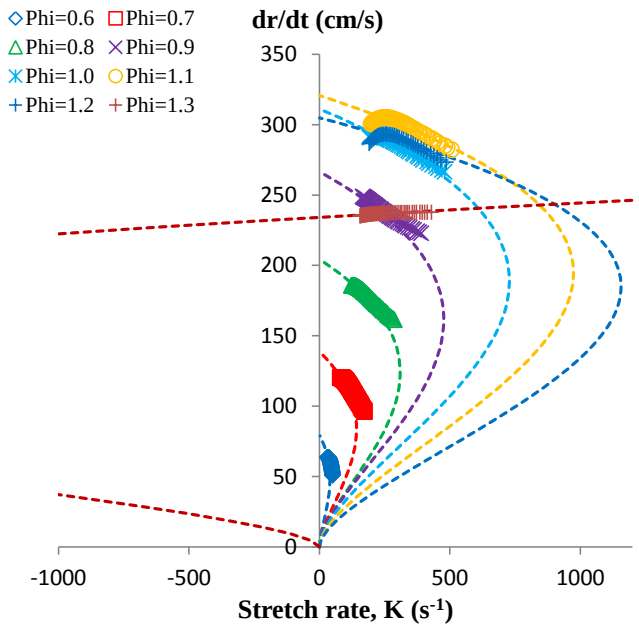

Figure 3.14: Burned gas velocity (S_b) of C_3H_8-air fit with the linear method.

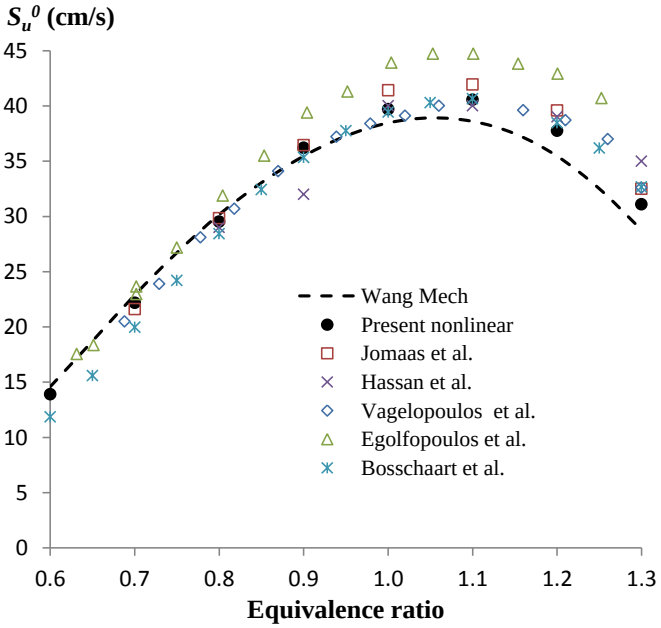

Figure 3.15: Burning velocity of premixed C_3H_8-air flames at 298 K and 1 bar (collected in 30 L chamber) as a function of equivalence ratio, together with previously published results and numerical predictions.

We further validate the new experiment by comparing burned gas Markstein lengths L_b for CH_4-air flames to results in literature. The present linearly and nonlinearly extracted results are shown in Figure 3.16 and Figure 3.17 , along with previous experimental results [86, 87, 105, 116, 121] and computational results of ref. [104]. Similar to what was seen in the above S_u^0 comparison, the present L_b values fall within the scatter of previously published data for the entire range of Φ. Nonlinearly extracted L_b values are in excellent agreement with the results of refs. [105, 121]. Moreover, at lean conditions the L_b values obtained by the linear and nonlinear method are similar, whereas at rich conditions the linear method yields L_b values that are considerably larger. Chen [102] showed the larger scatter in linearly extracted L_b (compared to nonlinearly extracted L_b) to be the result of higher sensitivity to the lower and upper radius bounds considered during extrapolation.

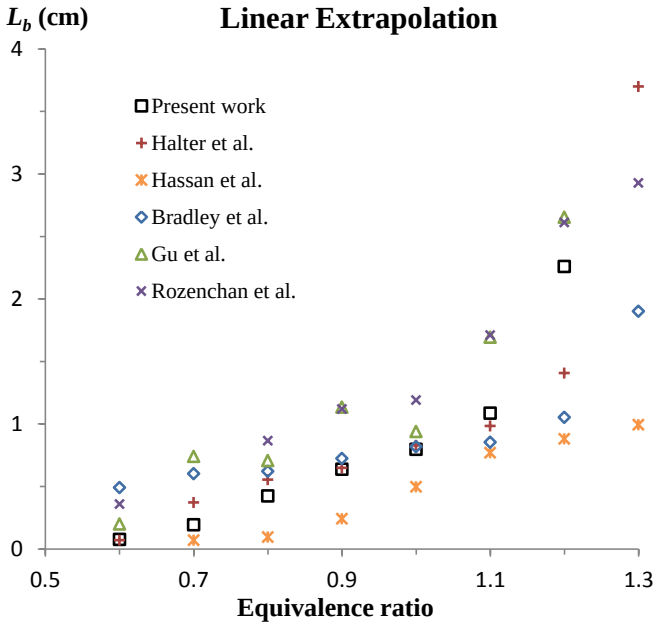

Figure 3.16: Linearly extracted burned gas Markstein lengths (solid squares) for CH_4-air flames ($0.6 \leq \Phi \leq 1.3$) compared with previously published experimental results (symbols).

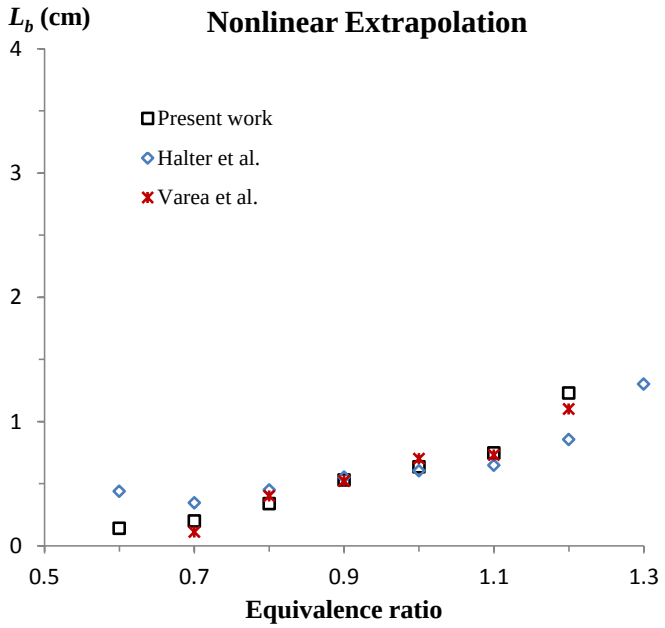

Figure 3.17: Non-linearly extracted burned gas Markstein lengths (solid squares) for CH_4-air flames ($0.6 \leq \Phi \leq 1.3$) compared with previously published experimental results (symbols).

Figure 3.18 provides Markstein lengths of C_3H_8-air flames as a function of equivalence ratio. Linearly and non-linear extracted results are plotted together (because less dataset are available in the literature) and compared to previous experimental [122-124] and numerical [125] datasets derived from spherically expanding flames. For rich conditions, present and previously reported Markstein lengths are all in good agreement and are relatively insensitive to the method of. At leaner conditions, the scatter in L_b becomes larger with the linearly extracted Markstein lengths generally higher (with the exception of ref. [125]). As observed for the CH_4-air flames, the present non-linear L_b values are in excellent agreement with the data reported by Varea [124].

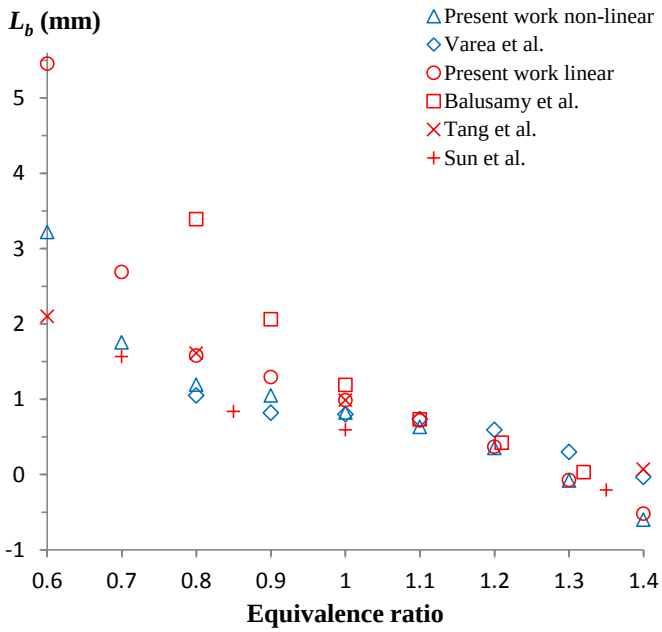

Figure 3.18: Burned gas Markstein lengths of premixed C_3H_8-air flames as a function of equivalence ratio, together with previously published results.

In addition to comparing the 30 L chamber burning velocities with data in literature, the results are compared to the 1.85 L chamber results in Figure 3.19 and Figure 3.20 for CH_4-air and C_3H_8-air flames respectively. Numerical predictions are included, with the GRI 3.0 and Wang mechanisms used to simulate CH_4-air burning velocities and the Wang mechanism used to simulate C_3H_8-air burning velocities. The two experiments provide nearly the same burning velocity for the CH_4-air mixtures, with measurements in the 30 L chamber slightly higher at Φ=0.9 and 1.2. Both experiments provide burning velocities that are similar to the predictions with the Wang mechanism and generally lower than the GRI 3.0 predictions. For the C_3H_8-air flames, the 30 L chamber consistently provides higher burning velocities than the 1.85 L chamber. At each equivalence ratio, the burning velocity given by the 30 L chamber is about 1.5 cm/s higher. At lean conditions, the 30 L chamber measurements are closer to the predictions

using the Wang mechanism; at rich conditions, the measurements for the 1.85 L chamber are closer. Overall, the two experiments give very similar burning velocities for the CH_4-air and C_3H_8-air flames ranging in equivalence ratio.

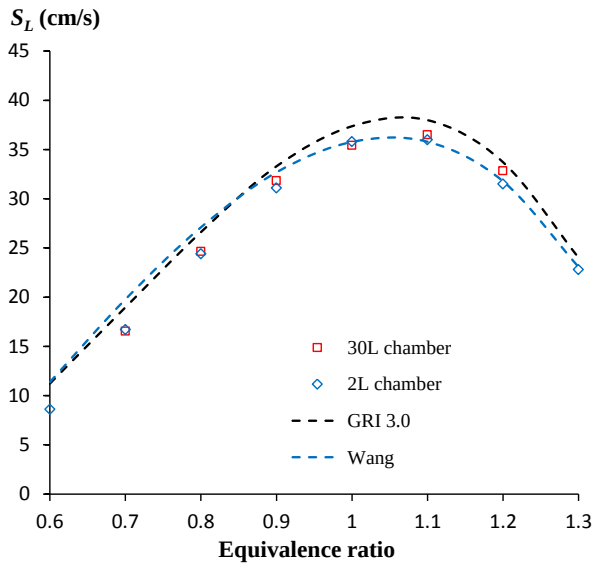

Figure 3.19: Comparison of CH_4-air burning velocities measured in the 1.85 L and 30 L, along with numerical predictions.

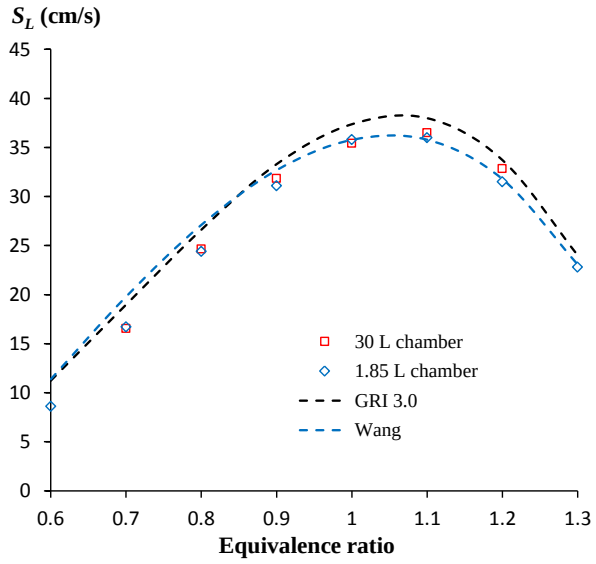

Figure 3.20: Comparison of C_3H_8-air burning velocities measured in the 1.85 L and 30 L, along with numerical predictions.

3.3 Numerical Methods

3.3.1 Description of Solvers

Thermodynamic equilibrium calculations are carried out using the EQUIL subroutine [78]. The equilibrium product species and their thermodynamic state are determined for a either a constant-pressure, constant-enthalpy process (minimization of Gibbs free energy) or a constant-volume, constant-energy process (minimization of Helmholtz free energy), depending on the nature of the problem under consideration.

The Sandia PREMIX code is used to calculate planar adiabatic premixed flame structure [126-128]. The equations of mass, species, and energy conservation are solved numerically for the initial temperature, pressure, and gas composition. The solution assumes steady, planar, one-dimensional, laminar flow. The process is isobaric and adiabatic, assuming constant pressure and no heat transfer. The boundary conditions include the mass flux fractions at the cold boundary. At the hot boundary all gradients vanish. An additional boundary condition is required for freely propagating flames in which the temperature is specified at one point between the cold and hot boundary. A modified damped Newton's method routine is then used to solve the boundary value problem.

Thermal diffusion is considered and molecular diffusion is modeled using mixture-averaged coefficients. The mixture-averaged diffusion model significantly reduces computational time while producing less than a 1.5% relative error in calculated burning velocities (when compared to the multicomponent model) for n-heptane-air over a range of equivalence ratios and at 1 atm [129]. We performed a similar analysis for

CH_4-air and C_3H_8-air burning velocities and found the relative error to increase with decreasing fuel molecule size (up to 3% for CH_4-air). Therefore, the largest error associated with the mixture-averaged model should occur at uninhibited conditions and decrease as the large molecule agents are added.

Computations are carried out on a 100 cm domain with gradient (GRAD) and curvature (CURV) values of 0.05. During simulation, the number of grid points ranged from 330 to 450, with the final 100 point grid refinement (GRAD and CURV from 0.1 to 0.05) resulting in less than a 2% change in calculated burning velocities (the change is typically much less, with the exception of slow burning mixtures with S_u^0~6cm/s). This level of convergence is acceptable considering the uncertainty in the measured S_u values.

3.3.2 Kinetic Mechanisms

Kinetic sub-models are assembled to study the detailed chemistry of inhibited (CF_3Br, C_2HF_5, $C_2HF_3Cl_2$, $C_3H_2F_3Br$, and $C_6F_{12}O$) hydrocarbon/air systems. The required sub-models for simulation are dependent on the chemical makeup of the inhibitor. All models contain a sub-model for hydrocarbon decomposition in air and hydrofluorocarbon decomposition in hydrocarbon-air systems. Agents CF_3Br and $C_3H_2F_3Br$ require additional reactions involving brominated species, $C_2HF_3Cl_2$ requires additional chlorinated and chlorofluorinated reactions, and $C_6F_{12}O$ requires additional reactions describing decomposition down to the species contained in the previously mention HFC sub-mechanism. The following section describes the different kinetic models used during detailed flame structure simulations.

The following sub-models are considered for CH_4- and C_3H_8-air flames with added C_2HF_5, $C_6F_{12}O$, or $C_2HF_3Cl_2$. Hydrocarbon-air reactions are modeled with the C1-C4 mechanism of Wang et al. [117] (111 species and 784 reactions). Reactions involving C1-C2 hydrofluorocarbons are modeled with an updated NIST HFC mechanism [26, 27] (62 species and 600 reactions). Recent updates to the original NIST HFC mechanism are summarized in refs. [9, 71]. C3 hydrofluorocarbon reactions related to C_3F_7H (FM-200) were taken from Williams et al. [130]. Reactions of larger fluorinated species necessary for $C_6F_{12}O$ decomposition are described with the model development work by Linteris et al. [10] (3 species and 14 reactions). The C1-C2 chlorocarbon chemistry is described using the mechanism of Leylegian et al. [131, 132] (50 species and 333 reactions), which was built off of the work of Wang et al. [133]. Reactions involving chlorofluorinated C1-C2 species are modeled using the newly developed mechanism of Babushok et al. [70] (14 species and 127 reactions).

The following sub-models, previously assembled in ref. [71], are considered to model CH_4 and C_3H_8-air flames with added CF_3Br or $C_3H_2F_3Br$. Hydrocarbon-air reactions are modeled with the C1-C4 mechanism of Wang et al. [117]. C1-C2 hydrofluorocarbon reactions are modeled with an updated version of the NIST HFC starting mechanism [26, 27], with the updates summarized in refs. [9, 71]. Decomposition reactions of brominated C1 species in the presence of hydrocarbon-air are modeled with an updated version of the original CF_3Br mechanism of Babushok et al. [32]. The updated mechanism, provided in ref. [71], includes more accurate rate coefficient data made available in literature since the original development of the mechanism in ref. [32]. Lastly, the Burgess et al. [134] model describes the reactions

involving larger brominated species formed during $C_3H_2F_3Br$ decomposition. Table 3.1 provides a summary of the sub-models used in the present study, along with the number of species and reactions contained in each model.

Table 3.1: Summary of kinetic models used in this study.

Kinetic model	Species	Reactions	References
C1-C4 hydrocarbon	111	784	[117]
Updated NIST C1-C2 HFC	52	621	[26, 27, 71]
C_3F_7H (FM-200)	10	48	[130]
$C_6F_{12}O$ (Novec 1230)	3	14	[10]
C1-C2 chlorocarbon	50	333	[131-133]
C1-C2 chlorofluorocarbon	14	127	[70]
C1 bromofluorocarbon	10	100	[32, 71]
$C_3H_2F_3Br$ (2-BTP)	7	40	[134]

Chapter 4: Lean Flame Enhancement by Halon Alternatives

4.1 Introduction

Experimental and numerical investigations of laboratory flames have described enhanced combustion with addition of halogenated suppressants, as outlined in ref. [9]. The phenomena include increased total heat release, widened lean flammability limits, decreased ignition delay, and increased pressure rise. Most of the early work documented the effects, but did not analyze the causes. In more recent work [8-13, 135], numerical combustion simulations have been applied to gain insight using recently developed (or updated) kinetic mechanisms [10, 26, 27, 32, 70, 71, 134]. The studies have concluded that exothermic reaction of the fire suppressants adds energy to the constant volume system, increasing the overpressure. To obtain the observed pressure rise in the FAA-ACT, agent reaction is shown to occur under very fuel-lean equivalence ratios (Φ, based on the aerosol can fuel only), nearly corresponding to pure agent and air. Kinetic calculations have indicated that addition of the agent to fuel-lean flames can increase not only the energy release, but the rate of reaction as well. Nonetheless, no laboratory-scale experiments have been conducted to validate the explanations or to explore the combustion enhancement observed in the FAA tests for the new agents $C_6F_{12}O$ and $C_3H_2F_3Br$ (and experiments for C_2HF_5 are limited [136, 137]). Experimental studies of the influence of halogenated suppressants on laminar burning velocity exist [28-30, 88, 131, 132, 138], but very little data are available for agent addition to very lean hydrocarbon-air mixtures (which are of most interest with regard to the FAA tests). Previous work has shown the effectiveness of the agents $C_6F_{12}O$ and $C_3H_2F_3Br$ in

standard tests for fire suppressant efficacy [139-142], but there are no data for their effect on burning velocity (a traditional method of quantifying flame inhibition effectiveness [143]).

In this chapter, the agents used in the FAA-ACT (CF_3Br, $C_6F_{12}O$, $C_3H_2F_3Br$, and C_2HF_5) are added at various sub-inerting concentrations to stoichiometric and lean CH_4-air flames in the 1.85 L constant volume combustion chamber to determine their influence on the maximum pressure rise and burning velocity. The effects of compressive heating on the burning velocity are also determined. The goals of the present work are to test the concepts developed via numerical simulations and analysis of the FAA tests [8-10], reproduce the phenomena observed in the complex full-scale FAA experiments, and explore if the laboratory-scale experiment can be used as a screening tool for cargo bay halon replacements. Although the FAA-ACT fuel is composed of propane, ethanol, and water, CH_4 was used to simplify the experimental procedure, and to reduce the potential influence of flame stretch and radiative heat loss from soot formation. Additionally, since the experimental data are among the first to examine the effect of added $C_6F_{12}O$ and $C_3H_2F_3Br$ on premixed flames, performing experiments with a simple hydrocarbon seems appropriate (previous work showed the inhibition effectiveness of halogenated suppressants to be relatively insensitive to the hydrocarbon fuel type [35]).

4.2 Results and Discussion

4.2.1 Peak Pressure Rise Considerations

The maximum pressure rise of CH_4-air explosions in a closed vessel was determined with addition of CF_3Br, $C_6F_{12}O$, $C_3H_2F_3Br$, and C_2HF_5 (T_0=298 K, P_0= 1

bar). Agents were added to stoichiometric flames and lean flames with a fuel-air equivalence ratio Φ of 0.6 (Φ based on uninhibited mixtures, i.e., when an agent is added, proportional quantities of CH_4 and air are displaced). Figure 4.1 and Figure 4.2 show the results for the stoichiometric and lean systems respectively. The peak pressure rise ΔP_{max} from experiments is shown, along with the calculated equilibrium ΔP_{max} and adiabatic temperature T_{ad} (calculated using CEA2, for a constant internal energy, constant volume system). The line style (and color) denoting the results for each agent are defined via the experimental curves, and the assignment is preserved for the two sets of equilibrium curves. For reference, the uninhibited system has T_{ad}=2599 K and ΔP_{max}=7.94 bar at equilibrium.

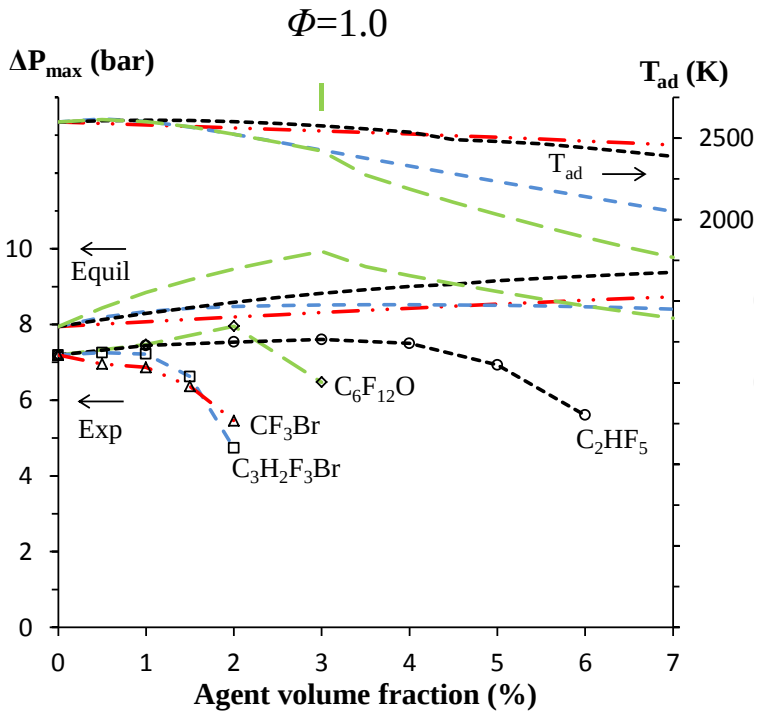

Figure 4.1: Pressure rise (left scale) and adiabatic temperature (right scale) in constant-volume combustion sphere with agents added to stoichiometric CH_4-air flames. Lines: equilibrium calculations; lines with symbols: experiments.

For the stoichiometric system, adding CF_3Br decreases T_{ad}, whereas adding any of the other agents slightly increases T_{ad} (≈2612 K) at low X_a, and then decreases it as X_a increases, with the larger inhibitor molecules decreasing T_{ad} more. The observed increases in T_{ad} are comparable to the increase that occurs from stoichiometric to slightly rich conditions in CH_4-air systems (peak T_{ad}=2615K at Φ=1.07).

For the stoichiometric case (Figure 4.1), the equilibrium pressure (lines with no symbols) increases with addition of each agent, including CF_3Br, up to a certain value of X_a, then drops for higher X_a. The value of X_a controlling this behavior is related to the halogen X to hydrogen H ratio [X]/[H] in the premixed gases, which is equal to unity for CF_3Br, $C_6F_{12}O$, $C_3H_2F_3Br$, and C_2HF_5 at X_a=0.09, 0.03, 0.16, and 0.09 (as indicted by the vertical lines at the top of the figure). Since X_a for [X]/[H]=1 is off the figure when adding CF_3Br, $C_3H_2F_3Br$, and C_2HF_5 to the stoichiometric case, the equilibrium ΔP_{max} increases continuously on the figure. The increase in ΔP_{max} is caused by the increase in the number of moles of products, which overrides the lower values of T_{ad} with agent addition. For X_a above [X]/[H]=1, the equilibrium products change (formation of COF_2 rather than HF, as a fate for F), so the number of moles of product decreases, reducing ΔP_{max}. As with T_{ad}, the equilibrium value of ΔP_{max} is higher for larger molecules (at least at low values of X_a), but they reach [X]/[H]=1 at different values of X_a, which dominates their behavior. With agent added to these stoichiometric flames, $C_6F_{12}O$, $C_3H_2F_3Br$, and C_2HF_5, have a maximum equilibrium pressures rise 2 bar, 1.5 bar, and 0.6 bar higher than with no agent, occurring at X_a=0.03, 0.07, and 0.04. Note that the equilibrium ΔP_{max} is relatively insensitive to X_a for $C_3H_2F_3Br$, and that calculations show an increase in ΔP_{max} even for addition of CF_3Br. Moreover, the equilibrium results for inhibited flames with

CH_4 as the fuel are qualitatively consistent with similar calculations as those for C_3H_8 or the aerosol can contents [5] as the fuel.

As shown in Figure 4.1 (again for Φ=1), the experimentally determined ΔP_{max} of all agents is less than the equilibrium value. For example, the uninhibited stoichiometric CH_4-air system has an experimental ΔP_{max}=7.2 bar, which is close to ΔP_{max}= 7.3 bar measured by ref. [144] and about 9% lower than the equilibrium value. To some extent, the experimental values of ΔP_{max} with added agent follow the trends in the equilibrium values, although the experimental ΔP_{max} rises more slowly than the equilibrium value, before eventually dropping rapidly. This can be caused by flame quenching (from heat losses at the wall [145] or from buoyancy [60]), by radiative heat loss, and (for these initially stoichiometric flames) by kinetic quenching of the flame reactions. While it is possible to define an extent of reaction λ based on the ratio of measured to equilibrium ΔP_{max} [145], this is of limited value in the present work since the effects interact: slower burning velocities (with inhibitor) allow more time for buoyancy to act, and buoyancy-induced quenching lowers the temperature (and hence the overall reaction rate), which can also affect the kinetic inhibition. Also, the effects are likely to depend upon the size of the sphere and degree of turbulence [146] (which are different in the FAA-ACT test). Note that while equilibrium calculations predict enhanced pressure rise with CF_3Br and $C_3H_2F_3Br$, both have none, and have much reduced pressure rise as X_a increases (likely due to kinetic inhibition by the bromine [71]). For addition to stoichiometric flames, $C_6F_{12}O$ and C_2HF_5 increase the experimental ΔP_{max} by 11% and 6%, at X_a=0.02 and X_a=0.03.

The influence of radiative heat losses in reducing the pressure rise was estimated via a calculation similar to that in ref. [59]. In the calculation, CO_2, H_2O, and HF were considered as radiating products, and the radiative heat loss of the expanding burned gas zone was estimated. Species volume fractions and burned gas temperatures were taken from equilibrium calculations using CEA2 [69]. The emissivity of CO_2 and H_2O (Hottel et al. [147]) and HF (Penner [148]) were estimated based on the burned gas temperature, partial pressures, mean equivalent beam length, and chamber pressure. The thermodynamic model (developed to calculate burning velocity) was used to estimate the flame radius r_f with respect to time to provide the mean equivalent beam length (4/3*r_f for a spherical volume). The radiative heat loss rate ($\dot{Q}_{rad} = \sigma \varepsilon A T_b^4$) was determined from the burned gas emissivity ε, burned gas temperature T_b, and flame area A. The rate was then integrated over the flame propagation time to yield the total radiative heat transfer. A chamber reflectivity of 0.25 was assumed for the stainless steel walls to account for residual buildup between cleaning. These estimates indicate that radiation ranges from 2% to 12% of the total heat release (highest for strongly inhibited lean mixtures), which is significantly higher than the 1% reported in ref. [59]. The larger values are primarily due to the lower heat release rates of the slower burning flames. Accordingly, since the experimental ΔP_{max} (i.e., heat release) is typically 30% to 60% lower than the equilibrium values (at the highest level of agent addition), as compared to the radiant losses of up to 12%, wall quenching (enhanced by buoyant flow) seems to be the primary cause for the lower experimental ΔP_{max}.

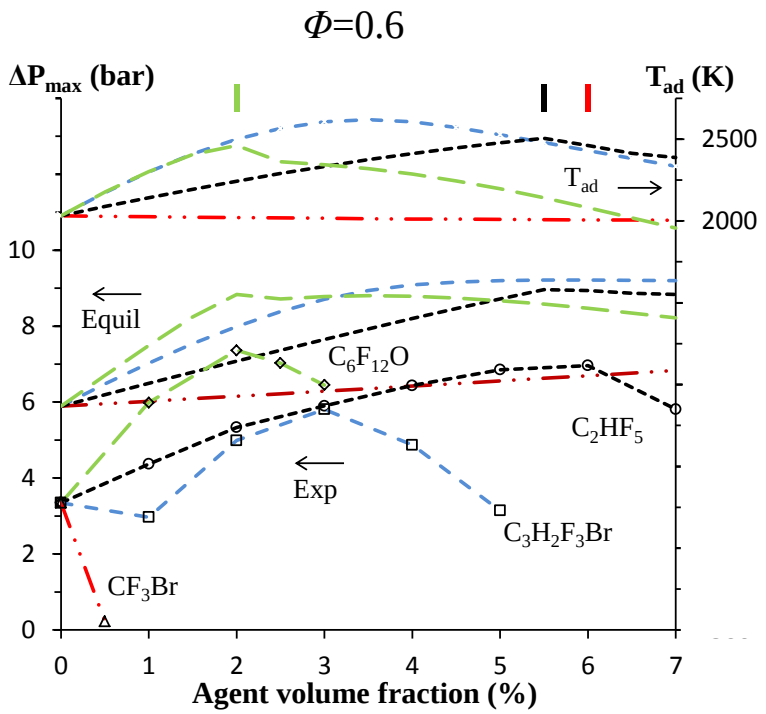

Figure 4.2: Pressure rise (left scale) and adiabatic temperature (right scale) in constant-volume combustion sphere with agents added to lean (Φ=0.6) CH_4-air flames. Lines: equilibrium calculations; lines with symbols: experiments.

Results for lean CH_4-air mixtures (Φ=0.6) are shown in Figure 4.2. For reference, the equilibrium adiabatic temperature and pressure rise for an uninhibited CH_4-air mixture at Φ=0.6 are 2031 K and 5.89 bar. With agent added to these lean flames, $C_6F_{12}O$, $C_3H_2F_3Br$, and C_2HF_5, have peak T_{ad} which are 331 K, 589 K, and 473 K higher than the uninhibited case, occurring at X_a=0.025, 0.035, and 0.055 (for $C_3H_2F_3Br$, the peak value of T_{ad} is 20 K higher than that of the uninhibited stoichiometric CH_4-air flame, while for C_2HF_5 and $C_6F_{12}O$ it's about 100 K and 140 K lower). The increase in T_{ad} is due to the higher enthalpy of formation of the reactant mixture, and the stable product species (e.g., CO_2, HF, etc.); that is, with regard to the thermodynamics, the agents have

fuel-like properties. In contrast, T_{ad} decreases by roughly 5 K for every 1% of added CF_3Br. For the pressure rise, the equilibrium results again show an increase in ΔP_{max} with addition of each agent, reaching a peak near the X_a for which [X]/[H]=1 (at $X_a \approx 0.06$, 0.02, 0.11, and 0.055 for CF_3Br, $C_6F_{12}O$, $C_3H_2F_3Br$, and C_2HF_5). For Φ=0.6, however, both the relative and absolute pressure rise are much bigger than for Φ=1, with equilibrium ΔP_{max} increasing by nearly 50% with addition of $C_6F_{12}O$, $C_3H_2F_3Br$, or C_2HF_5. In the experiments, the pressure rise was again always lower than the equilibrium value (i.e., λ<1). For example, for X_a=0, ΔP_{max} was 3.35 bar, or 43% lower than the equilibrium value, or λ=0.57, which is much lower than the case of Φ=1 and X_a=0, for which λ=0.91 (as discussed previously [60], slower flames are more strongly influenced by buoyancy-induced quenching). With addition of the agents, however, the behavior for Φ=0.6 is different from that for Φ=1. For the lean flames, λ often increases as X_a increases, as compared to the Φ=1 case for which λ decreases. With regard to the peak experimental pressure rise, addition of $C_6F_{12}O$, $C_3H_2F_3Br$, or C_2HF_5 yielded a ΔP_{max} of 7.36 bar, 5.81 bar, or 6.96 bar, at X_a of 0.02, 0.03, or 0.06. These values are 2.2, 1.7, and 2.1 times the ΔP_{max} for the uninhibited system (3.35 bar). In contrast, addition of CF_3Br at X_a=0.005 extinguished the flame just after ignition, yielding ΔP_{max}=0.22 bar.

The results for the explosion pressure in the 1.85 L chamber (for Φ=0.6) clearly illustrate the combustion enhancement of the type observed in the FAA-ACT [5], whereas results for Φ=1 do not adequately duplicate the behavior. Hence, reduced-scale explosion vessels, used to evaluate lean fuel-air systems, are a valuable tool for understanding the FAA-ACT results; for example, the measurements of ΔP_{max} highlight the increased heat release occurring with addition of the halon replacements to the lean

system. More than just the higher explosion pressure with added agent, however, the higher extent of reaction with added agent (in the Φ=0.6 case) implies a higher burning velocity with agent addition to the lean flames. To more clearly investigate this possibility, the burning velocity is calculated from the pressure rise data (as described above) to more clearly delineate the effect of the agents on the overall reactivity of the system.

4.2.2 Laminar Burning Velocity

The laminar burning velocity was measured for the stoichiometric (Φ=1) and lean (Φ=0.6) CH_4-air flames. Initial conditions were T_0=296 ±2 K, and P_0=0.868 bar, 1 bar, and 1.13 bar, (to provide more data for the curve fit). For each agent, tests were conducted up to values of X_a for which S_u≈6 cm/s (since buoyant distortion has been found to be minimal for S_u>6 cm/s). For each value of Φ and X_a, tests were conducted at the three values of P_0, providing the fitting parameters $S_{u,0}$, α, and β in Eq. 7 above. From these, the burning velocity was obtained at ambient and compressed conditions, as listed in Table 4.1. The burning velocity of the inhibited flames for each of the agents is presented in Figure 4.3 and Figure 4.4 (Φ=1 and Φ=0.6, respectively) as the normalized burning velocity (for a given Φ and agent, S_u at X_a is divided by S_u with X_a=0). Results for each agent are illustrated with different style symbols; closed and open symbols represent data at standard (298 K, 1 bar) and compressed (400 K, 3 bar) conditions.

Table 4.1: Initial conditions, fit parameters, burning velocities, adiabatic temperatures, and explosion pressures for uninhibited CH_4-air flames.

Φ	0.6	1.0
α	2.23	1.68
β	−0.42	−0.33
$S_{L,0}$	8.3	35.8
S_L (400 K, 3 bar)	10.0	44.5
T_{ad}	2031	2599
$\Delta P_{max,equil}$	5.89	7.94
$\Delta P_{max,exp}$	3.35	7.19

As Figure 4.3 shows, for stoichiometric flames, adding each agent reduces S_u at all values of X_a, with a decreasing marginal effectiveness at higher X_a, as has been discussed previously [34, 149]. The present measurements (for T_0=298 K) can be compared to results in the literature. For CF_3Br addition, the reductions in S_u are very close to the stretch-corrected, spherically propagating flame results of Osorio et al. [88]; for example, at X_a=0.01 the present result of 15.0 cm/s compares to Osorio et al.'s value of 14.9 cm/s. Linteris et al. [29, 150] measured the burning velocity of flames inhibited with CF_3Br and C_2HF_5 using a Mache-Hebra burner (for values of S_u down to about 10 cm/s). In general, the present results are lower (including the uninhibited case), by roughly 4 cm/s, although the normalized values of S_u from the present data are in good agreement with those in refs. [29, 150], generally within +-5% at $X_a \leq 0.03$ and +-15% at higher concentrations.

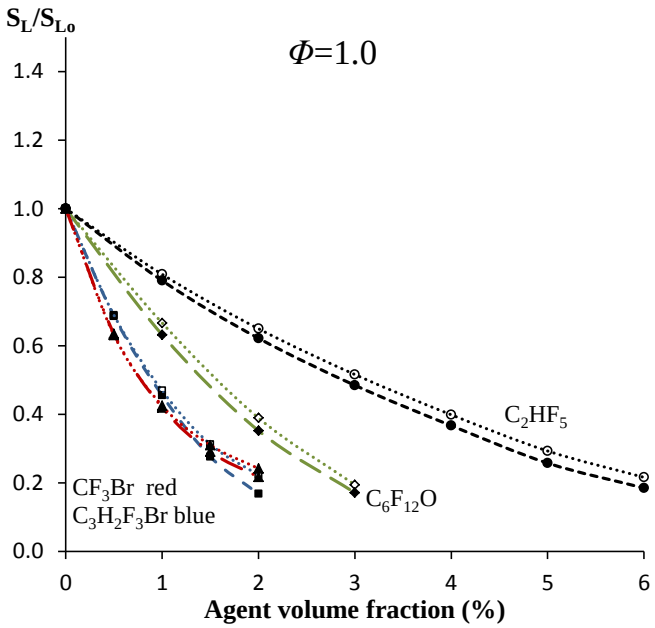

Figure 4.3: Normalized burning velocity with agents added to stoichiometric CH_4-air flames. Dashed lines: P_0=1 bar, T_0=298 K; dotted lines: P_0=3 bar, T_0=400 K.

On a molar basis, $C_6F_{12}O$ requires 1/2 as much as C_2HF_5 for a comparable reduction in S_u, and $C_3H_2F_3Br$, about 1/3 as much. The performance of $C_3H_2F_3Br$ and CF_3Br are roughly equivalent (on a molar basis), although CF_3Br is slightly more effective for X_a<0.01, and $C_3H_2F_3Br$ for X_a>0.01. This is consistent with cup burner results (heptane) [151, 152] for which $C_3H_2F_3Br$ was found to have a lower minimum extinguishing concentration (2.6%) than CF_3Br (2.9%), and $C_6F_{12}O$ required roughly 50 % more than CF_3Br (4.5%). Comparison of the results at ambient (T_0=298 K, P_0=1 bar) vs. compressed (T_0=400 K, P_0=3 bar) conditions shows that while the compressed flames have an uninhibited value of S_u about 14% higher, the reduction in normalized S_u with added agents is about 2% less for the compressed flames than for the ambient flames at low values of X_a, and 4% less at high values of X_a. This can be compared to flame inhibition by CO_2, for which the calculated normalized reduction in S_u at T_0=353 K as

compared to T_0=298 K was 8%, 4%, and 0.3% lower at X_a= 0.03, 0.07, and 0.15 [153]. That is, for these initially stoichiometric flames, these changes in the unburned gas conditions do not appear to significantly affect the inhibition kinetics of these agents.

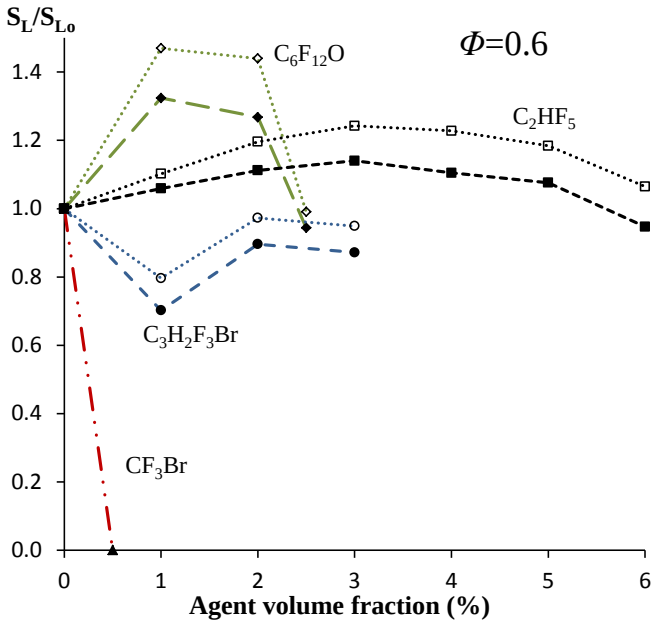

Figure 4.4: Normalized burning velocity with agents added to lean (Φ=0.6) CH_4-air flames. Dashed lines: P_0=1 bar, T_0=298 K; dotted lines: P_0=3 bar, T_0=400 K.

For the lean (Φ=0.6) flames, the effects of added agents on S_u are different than at Φ=1. For T_0=298 K, $C_6F_{12}O$ and C_2HF_5 increase S_u by 32% and 13% at X_a=0.01 and 0.03. That is, with $C_6F_{12}O$ or C_2HF_5 added to lean flames of CH_4–air, the mixture becomes more reactive, with significantly increased burning velocity: S_u is increased for all values of X_a up to about 0.025 for $C_6F_{12}O$, and 0.065 for C_2HF_5. In contrast, with CF_3Br addition to the lean flame (at X_a=0.005), the mixture was not flammable when subject to the highest available ignition energy. (The dashed line in Figure 4.2 is included to illustrate the inerting nature of CF_3Br at X_a=0.005 and is not intended to provide S_u values between those measured at X_a=0 and X_a=0.005.) The results for $C_3H_2F_3Br$ are

intermediate between those of CF_3Br and the other agents: for X_a=0.01, S_u decreases by 30%, but as X_a increases, S_u increases so that at X_a=0.02 and 0.03, S_u is only about 10% lower than the uninhibited flames. Note that with $C_3H_2F_3Br$ addition to the lean flame, the measured S_u is never higher than with no agent. Apparently, the gas-phase catalytic radical recombination cycles of brominated species have a larger inhibition effect in the present flames than the promotion effect of the agent due to the increased temperature [154]. (Nonetheless, the present oxidizer is dry. With added water vapor, typical of ambient air, the results may be different, as discussed previously [135, 154].) With $C_6F_{12}O$ addition, S_u drops rapidly above X_a=0.02, and with C_2HF_5 addition, it drops slowly above X_a=0.03. At the compressed condition, the peak enhancement in S_u with addition of $C_6F_{12}O$ and C_2HF_5 is larger by 47% and 24%, while the decrease in S_u with $C_3H_2F_3Br$ addition is less. (Note that from α and β in Table 4.1, the effect of compression is primarily caused by higher temperature, not pressure, which has a small effect for the present range of variation in T_0 and P_0.)

The present results illustrate that when added to lean premixed dry CH_4-air flames at low concentrations, the agents $C_6F_{12}O$ and C_2HF_5 actually increase the burning velocity, and for $C_3H_2F_3Br$ addition, the burning velocity is reduced slightly (about 10% at X_a=0.02 or 0.03). These results, together with the measured higher explosion pressures in the presence of these agents, are consistent with the higher overpressure in the FAA-ACT. Under lean conditions in the FAA-ACT, exothermic reaction of the agent creates higher overpressure than with no agent, and apparently the reaction rate is not sufficiently slowed (or is actually increased) with agent addition, so as to reduce the overpressure. In contrast, addition of CF_3Br both reduces the reaction rate for all stoichiometries, and

causes no increase in the explosion pressure. These principles were predicted in numerical simulations, but the present results are experimental verification of the principles previously outlined [8-10, 135], and the first to show increased flame speed of lean flames with added halon replacements.

4.3 Conclusions

Several potential halon replacements, for use in cargo-bay fire suppression, failed a mandated FAA performance test. To help understand their behavior, experiments were performed in a constant-volume combustion device (premixed CH_4-air system) to measure the peak pressure rise and burning velocity resulting from addition of the agents (CF_3Br, $C_6F_{12}O$, $C_3H_2F_3Br$, and C_2HF_5).

The influence of the agents on explosion pressure varied with agent type and concentration, as well as the initial stoichiometry of the CH_4-air mixture. For stoichiometric flames, addition of CF_3Br or $C_3H_2F_3Br$ reduced the peak pressure rise at all agent loadings; while $C_6F_{12}O$ and C_2HF_5 increased ΔP_{max} slightly at low loadings ($X_a \leq 0.02$ and 0.03), and reduced it at higher X_a. The equilibrium adiabatic temperatures initially increased (at low X_a) before dropping slightly with addition of CF_3Br or C_2HF_5 and significantly with addition of $C_3H_2F_3Br$ or $C_6F_{12}O$ to stoichiometric flames.

In lean (Φ=0.6) flames, however, addition of $C_6F_{12}O$, $C_3H_2F_3Br$, and C_2HF_5 all increased the pressure rise, with a peak pressure rise of about a factor of two above the uninhibited case, and occurring at agent loadings of 2% to 6%, depending upon the agent. In contrast, CF_3Br caused no increase in the ΔP_{max} at any condition. Pressure rises were always less than those predicted by equilibrium calculations, and the difference increased

at higher agent loadings. The equilibrium adiabatic temperatures also increased with agent addition to lean flames (to values close to those of stoichiometric CH_4-air flames), and did not drop off as rapidly at higher X_a as did the experimentally determined ΔP_{max}.

All agents were found to reduce burning velocity of stoichiometric CH_4-air flames at the concentrations tested. CF_3Br and $C_3H_2F_3Br$ caused similar flame speed reductions (about 55% at X_a=0.01), with CF_3Br slightly more effective at X_a=0.01 and below, and $C_3H_2F_3Br$ more effective above. $C_6F_{12}O$ and C_2HF_5 were about 2/3 and 1/3 as effective as CF_3Br at reducing the burning velocity of stoichiometric flames.

For lean (Φ=0.6) CH_4-air flames at ambient initial temperature and pressure, addition of $C_6F_{12}O$ and C_2HF_5 at sub-inerting concentrations increased the burning velocity by 32% and 13%. That is, when added to lean flames, not only do they increase the explosion pressure, but they can also enhance the reactivity. Addition of $C_3H_2F_3Br$ slightly decreased the burning velocity (for X_a<=0.03), while addition of CF_3Br (at X_a=0.005) inerted the mixture.

The data also provided burning velocities at compressed conditions (P_0=3 bar; T_0=400 K), for which agent addition to stoichiometric CH_4-air mixtures reduced the burning velocities slightly less than at ambient conditions (P_0=1 bar; T_0=298 K). For the lean (Φ=0.6) mixtures, addition of $C_6F_{12}O$ or C_2HF_5 increased the burning velocity (over uninhibited values) significantly (≈25% to 50%) more than for the ambient conditions. Similarly, the reduction in the burning velocity with $C_3H_2F_3Br$ addition was reduced at the compressed condition. (It should be noted that the present results are for dry mixtures. Addition of water vapor may affect the findings.) The experimental data

indicate that the stronger enhancement at compressed conditions is due almost entirely to the higher temperature, not pressure.

In practice, when used to suppress fires, clean agents are typically added at concentrations high enough to extinguish the flames. In the present tests (and as apparently occurs in the FAA Aerosol Can test), however, when some halon replacements are added to lean mixtures (in closed vessels) at sub-inerting concentrations, they can enhance both the pressure rise and rate of reaction. These properties may be relevant for other situations as well, for example when halogenated hydrocarbons (as suppressants or inadvertently released agents) premix with air and a hydrocarbon fuel from some other source. Moreover, the present results show that reduced-scale combustion spheres are useful screening tools for the potential of halon replacements to cause unwanted combustion enhancement in full-scale use.

Chapter 5: Premixed Flame Inhibition by $C_2HF_3Cl_2$ and C_2HF_5

5.1 Introduction

Previous work analyzing the FAA-ACT [8-11] showed that the overpressure phenomenon depends upon the heat release from agent reaction (and consequent higher temperature), in competition with the slower reactivity of the halogen-inhibited, hydrocarbon-air systems. This competition was most apparent for very lean hydrocarbon-air flames and for pure suppressant-air flames (with predicted burning velocities of a few cm/s), which exist in the end gases of the FAA-ACT chamber. As described below, the agent $C_2HF_3Cl_2$ (CF_3CHCl_2, HCFC-123) has been considered as a potential CF_3Br replacement [13, 70, 155] and has potential to overcome the enhanced overpressure in the FAA-ACT; hence, it is the subject of study in the present work. Because the agent C_2HF_5 has also been tested in the FAA-ACT, is the analogous HFC agent (to the HCFC $C_2HF_3Cl_2$), and is used as a halon replacement, it is analyzed in the present work for comparison.

Shebeko et al. [136] measured the flammability limits of many halogenated hydrocarbons and found the hydrochlorofluorocarbons, HCFCs, to require lower concentrations than the hydrofluorocarbons, HFCs, for inertion of H_2-air and CH_4-air flames. Moore et al. [156], using an n-heptane co-flow diffusion flame (cup-burner), found minimum extinguishing values (MECs) of 0.094 and 0.071 for C_2HF_5 and $C_2HF_3Cl_2$, again illustrating superior performance for the HCFC relative to HFC. Variable strain rate opposed flow diffusion flame experiments [157], as well as turbulent spray diffusion flame experiments [158], indicated that among various HCFCs and HFCs,

C_2HF_4Cl required the lowest mass fraction (with the exception of CF_3Br) for flame extinction. The higher suppression effectiveness of chlorinated as compared to fluorinated compounds has been discussed [18, 24, 35]. Chlorine participates in catalytic recombination cycles, so that each Cl atom recombines a larger number of radicals, whereas fluorinated species essentially trap one radical per F atom, ultimately forming HF, which, due to its high stability does not enter into catalytic cycles [18]. Hence, kinetically, the agent $C_2HF_3Cl_2$ should lower the reactivity more so than C_2HF_5, since two of the F atoms are replaced by Cl atoms.

Another benefit of HCFCs over HFCs is a potentially lower heat release with added agent. Holmstedt et al. [159] performed co-flow diffusion flame experiments with HFC, HCFC, and Halon 1301 suppressants premixed in the *fuel* stream (propane), and found that Halotron I (about 95% $C_2HF_3Cl_2$) was the only agent tested, besides CF_3Br, that did not increase the heat release rate. Takahashi et al. [13] performed simulations of co-flow diffusion flames stabilized on a cup burner, and found that at volume fractions just below those for extinguishment, C_2HF_5 increased the total heat release in the flame by 158 %, whereas $C_2HF_3Cl_2$ increased it by only 37 %. Similarly, Shebeko et al. [136] found that CHF_3 widened the lean flammability limit (of CH_4-air flames), whereas CHF_2Cl did not. Babushok et al. [70], developed a kinetic reaction mechanism for $C_2HF_3Cl_2$, and using it predicted that $C_2HF_3Cl_2$ should provide greater burning velocity reduction than C_2HF_5 when added to stoichiometric premixed CH_4-air flames. Initial tests of the performance of the mechanism were performed using experimental data available in the literature (burning velocity data for CO-H_2-O_2-Ar mixtures with the added one-carbon HCFCs: $CFCl_2$, CF_2Cl_2, and CF_3Cl) [160]; however, no experimental data exist

for the inhibition effectiveness of $C_2HF_3Cl_2$ when added to premixed hydrocarbon-air flames, and many of the previous studies do not consider $C_2HF_3Cl_2$ itself.

The present work provides initial tests of the accuracy of the newly developed HCFC kinetic model [70] for predicting burning velocity of CH_4-air flames with added $C_2HF_3Cl_2$. For comparison, experiments and simulations are also performed for the analogous HFC compound C_2HF_5. The 1.85 L chamber provides the laminar burning velocity of CH_4-air flames (for a range of stoichiometries) with added $C_2HF_3Cl_2$ and C_2HF_5, for ambient (298 K; 1.01 bar) and elevated (400 K; 3 bar) conditions. The experimental results are compared to the numerical predictions obtained using the newly-developed kinetic mechanism. The results are used to explore the advantages of chlorinated hydrocarbons over fluorinated as flame inhibitors.

While $C_2HF_3Cl_2$ itself is likely to be banned by the Montreal Protocol (due to its ozone depletion potential, ODP), the generic value of Cl substitution for F is examined here to provide a basis for exploring new low-ODP halon replacements which may be developed (e.g., halogenated ketones or alkenes). Moreover, $C_2HF_3Cl_2$ has very low ODP (0.02) and GWP (77), which might be deemed acceptable relative to other alternatives.

5.2 Results and Discussion

5.2.1 Kinetic Model Validation

To validate the kinetic model for HCFCs, the experimentally measured burning velocities of CH_4-air flames with added $C_2HF_3Cl_2$ or C_2HF_5 are compared to numerical predictions. For the HFC sub-mechanism, validations have been performed previously

[28-31, 130, 161]. The recent upgrades, mentioned in the numerical modeling section, mostly involve reactions of F atom, and are only important for mixtures of pure agent in air (not inhibited hydrocarbon-air flames, in which [F] is low) [11]; hence, the previous validation studies are still valid. Nonetheless, a comparison of measured and numerically predicted burning velocities is first made for CH_4-air flames inhibited by C_2HF_5 to illustrate performance of the HFC sub-mechanism and to test it at leaner conditions than previously considered.

Figure 5.1 shows the present experimental burning velocities for CH_4-air flames at Φ=0.6 and Φ=1.0 (Δ and □ symbols, respectively) with added C_2HF_5 ($0 \geq X_a \geq 0.07$) at ambient (298 K; 1.01 bar) conditions, together with numerical predictions (lines). Experimental burning velocities from other researchers [29, 162, 163] are also shown (X, *, and + symbols). (The reported equivalence ratios Φ are based on the uninhibited mixtures prior to agent addition: as agent is added, proportional amounts of CH_4 and air are displaced.) For Φ=1.0, the present experimental measurements compare reasonably well with published results using the stretch-corrected spherically propagating flame method [163] and the total area method [29, 162].

For the initially stoichiometric flames (Φ=1.0) the calculated burning velocities agree well with the present experimental results for the entire range of agent loading considered ($X_a \leq 0.06$). At X_a<0.04 the predicted S_u is within the experimental uncertainty (about the size of the symbols) of the data, while at higher X_a, it is up to 12% lower. For Φ=0.6, agreement is poor for uninhibited flames and at low agent loading (as discussed below), but improves as X_a increases. For example, at X_a=0, the predicted S_u (11.3 cm/s)

is 43% higher than the measured value (8.3 cm/s), while at $X_a \geq 0.05$, agreement improves to within 3%.

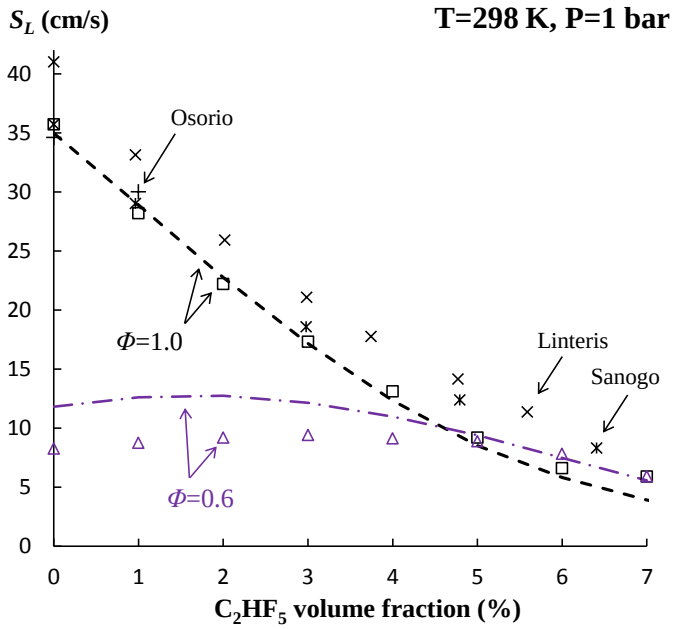

Figure 5.1: Laminar burning velocity of CH_4-air flames at equivalence ratios Φ of 0.6 and 1.0 as a function of C_2HF_5 concentration (initial condition: 298 K and 1.01 bar).

Figure 5.2 presents similar comparisons for the compressed initial conditions (400 K; 3 bar). The accuracy of the numerical predictions is again very good for stoichiometric flames (at all agent loadings), and for lean flames at high agent loading, but poor for lean flames at low C_2HF_5 loading. Reasons are discussed below.

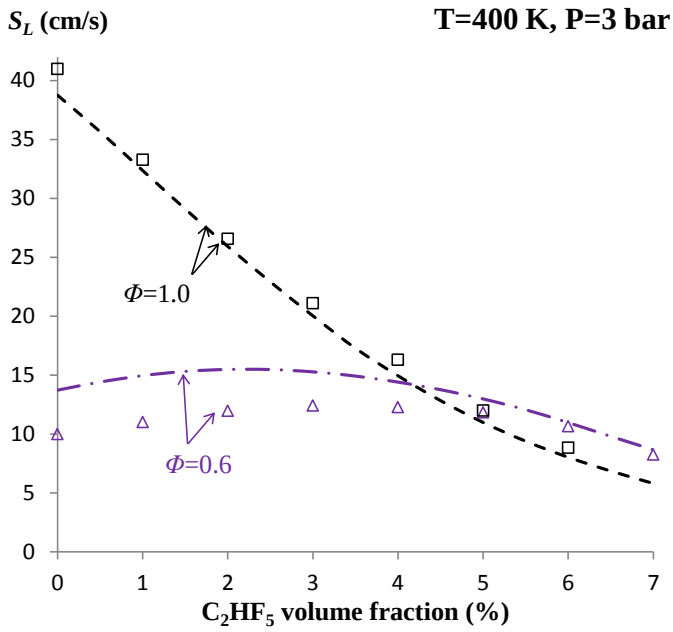

Figure 5.2: Laminar burning velocity of CH_4-air flames at equivalence ratios Φ of 0.6 and 1.0 as a function of C_2HF_5 concentration (initial condition: 400 K and 3 bar).

The largest discrepancy between measured and predicted burning velocity occurs at lean uninhibited conditions (Φ=0.6 and X_a=0.0). The hydrocarbon-air portion of the mechanism [117] has been extensively validated for a wide range of fuels and flame conditions (with the exception of very lean flames), suggesting that the disagreement between calculated and measured S_u for Φ=0.6 and low agent loading may be due to experimental considerations (such as flame stretch, buoyancy, and/or radiative heat loss). Although flame stretch effects are not fully eliminated using the present experimental method, they seem not to be the cause of discrepancy. For example, for uninhibited CH_4-air at Φ=0.6, the present results agree well with stretch-corrected spherically propagating flame results [86-88, 105]. Buoyancy is unlikely the cause of discrepancy since results obtained in microgravity for CH_4-air at Φ=0.6 [164, 165] are ~20% lower (and further from the numerical prediction) than the present experimental result. Also, in a previous

study [166] with the present experimental technique, the influence of buoyancy was found to be negligible when measuring burning velocities greater than 6 cm/s. Investigating the possible causes for the disagreement between numerical and experimental S_u of lean CH_4-air mixtures ($0.5 \leq \Phi \leq 0.65$), Chen [118] showed that radiation and compression of the unburned gases result in lower measured burning velocities when using the spherically expanding flame technique. In the present study, compression effects are not of concern because the pressure trace is used to determine S_u, not flame-front tracking (which assumes constant-pressure during the observed propagation). Chen [118] found that burning velocities of lean mixtures were more strongly affected by radiative losses because the relative reduction of flame temperature was greater for mixtures with lower adiabatic flame temperatures (or alternatively, the radiative heat loss rate is a higher fraction of the total heat release rate at the low reaction rate of the lean flames). This may explain the improved performance of the numerical prediction at higher X_a in the lean flames (adding agent to a lean CH_4-air increases the heat release; for example, adding C_2HF_5 increases the adiabatic flame temperature from 1629 K at X_a=0 to 2003 K at X_a=0.05).

To validate the chlorine-species portion of the kinetic model, measured values of S_u for CH_4-air flames with added $C_2HF_3Cl_2$ are compared with model predictions. Figure 5.3 presents the experimental S_u (symbols) with the numerical predictions (lines) for addition of $C_2HF_3Cl_2$ to flames with four different initial stoichiometries (Φ=0.6, 0.9, 1.0, 1.1), at agent volume fractions X_a of 0 to 0.05 (different symbol and line styles present data at different initial equivalence ratios). Overall, model predictions agree very well with the experimental results; predicted burning velocities are within 7% for all agent

loadings at Φ=1.0, 0.9, and 1.1 (with the exception of X_a=0.04, Φ=1.1, where the prediction is 15% higher). At leaner conditions (Φ=0.6), agreement is less satisfactory, although as with C_2HF_5, it improves as the $C_2HF_3Cl_2$ concentration increases. The discrepancy for the uninhibited lean flame (Φ=0.6) is again likely a consequence of the radiative heat loss. Nonetheless, with $C_2HF_3Cl_2$ addition ($0.01 \leq X_a \leq 0.05$), agreement at Φ=0.6 is better than with C_2HF_5 addition.

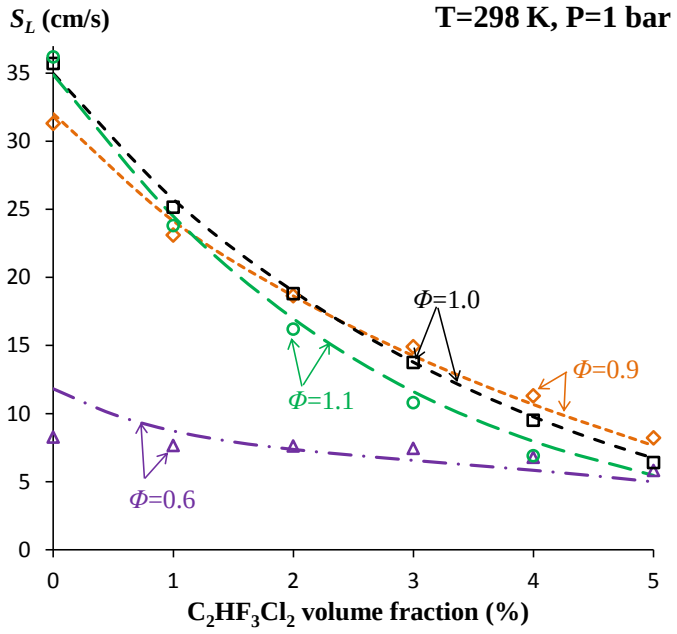

Figure 5.3: Laminar burning velocity of CH_4-air flames at equivalence ratios Φ of 0.6, 0.9, 1.0, and 1.1 as a function of CF_3CHCL_2 concentration (initial condition: 298 K and 1.01 bar).

Figure 5.4 shows the burning velocities with $C_2HF_3Cl_2$ addition to CH_4-air flames at the compressed conditions (400 K; 3 bar). The agreement is somewhat better than for the flames at the initially ambient conditions (Figure 5.3), with the largest discrepancies again occurring at the uninhibited conditions. At Φ=0.9-1.1 and Φ=0.6 S_u predictions of inhibited mixtures are within 7% and 14% of the measured values, respectively (again

with the exception of X_a=0.04, Φ=1.1, where the prediction is 12% higher). The overall agreement between numerical and experimental results is very good considering the early stage of development of the kinetic mechanism for the mixed fluorine/chlorine/hydrocarbon system.

At compressed conditions, adding $C_2HF_3Cl_2$ to lean (Φ=0.6) CH_4-air mixtures no longer reduces the experimentally measured burning velocity for all X_a. For example, at X_a=0.02, the burning velocity is 3% higher than the uninhibited case, while at higher loading ($X_a \geq 0.04$), the burning velocity is once again reduced compared to X_a=0. The lower inhibition effectiveness of $C_2HF_3Cl_2$ at 400 K and 1.01 bar is consistent with the findings reported in Chapter 4, in which reduced effectiveness was observed for C_2HF_5, $C_3H_2F_3Br$, and $C_6F_{12}O$ at compressed initial conditions.

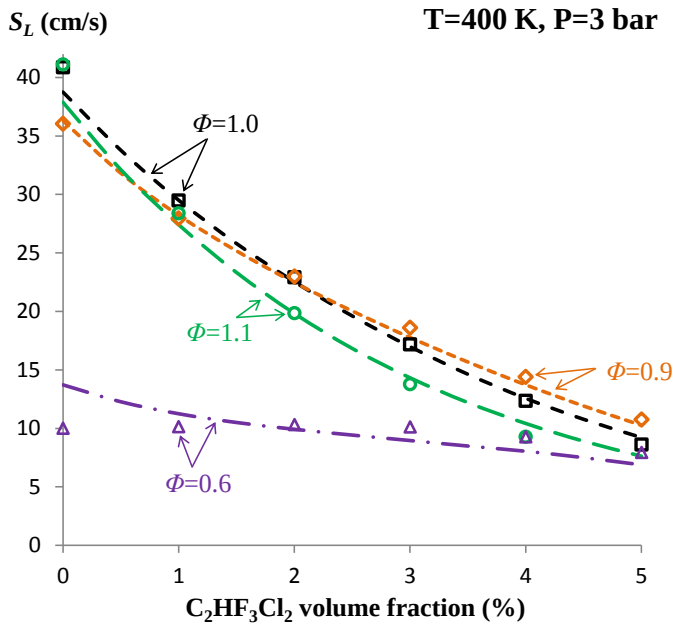

Figure 5.4: Laminar burning velocity of CH_4-air flames at equivalence ratios Φ of 0.6, 0.9, 1.0, and 1.1 as a function of CF_3CHCL_2 concentration (initial condition: 400 K and 3 bar).

5.2.2 Comparing Agent Influence on Burning Velocity

Figure 5.5 presents the burning velocities (bottom curves) for premixed CH_4-air flames with added $C_2HF_3Cl_2$ (triangles) or C_2HF_5 (circles) for stoichiometric (Φ=1.0, closed symbols) and lean (Φ=0.6, open symbols) flames at 298 K and 1.01 bar. The adiabatic flame temperatures are shown in the top curves for $C_2HF_3Cl_2$ and C_2HF_5 by solid and dashed lines. As Figure 5.5 shows, at stoichiometric conditions, $C_2HF_3Cl_2$ provides a larger reduction in S_u, than does C_2HF_5. For example, at an agent volume fraction of 1%, X_a=0.01, $C_2HF_3Cl_2$ and C_2HF_5 reduce S_u to 25.2 cm/s and 28.2 cm/s, respectively. As more agent is added, the marginal reduction of S_u is nearly the same, illustrated by similar slopes in Figure 5.5 once $X_a \geq 0.02$. As the upper curves in Figure 5.5 show, the adiabatic flame temperatures for the two agents (at Φ=1.0) are similar for the range of X_a considered, with the largest difference occurring at X_a=0.05, where T_{ad} is 24 K lower with $C_2HF_3Cl_2$ addition than with C_2HF_5 addition. The greater reduction in S_u with $C_2HF_3Cl_2$ (while T_{ad} is similar) suggests that chlorine substitution improves the inhibition performance via a kinetic mechanism rather than thermal.

At lean conditions, sub-inerting concentrations of C_2HF_5 slightly increase burning velocity (up to 6%), as described in Chapter 4, whereas similar concentrations of $C_2HF_3Cl_2$ reduce S_u by 7%-30% (at 298 K and 1.01 bar). The adiabatic flame temperatures increase with addition of either agent, and while the values are similar for addition of either agent, there is a slight difference between them that increases as X_a increases (up to a 45 K difference at X_a=0.05). Interestingly, for each agent, the burning velocity of the stoichiometric and lean systems are very close to each other (within 0.6

cm/s) at X_a=0.05 (and the adiabatic flame temperatures are also roughly equal at that agent loading).

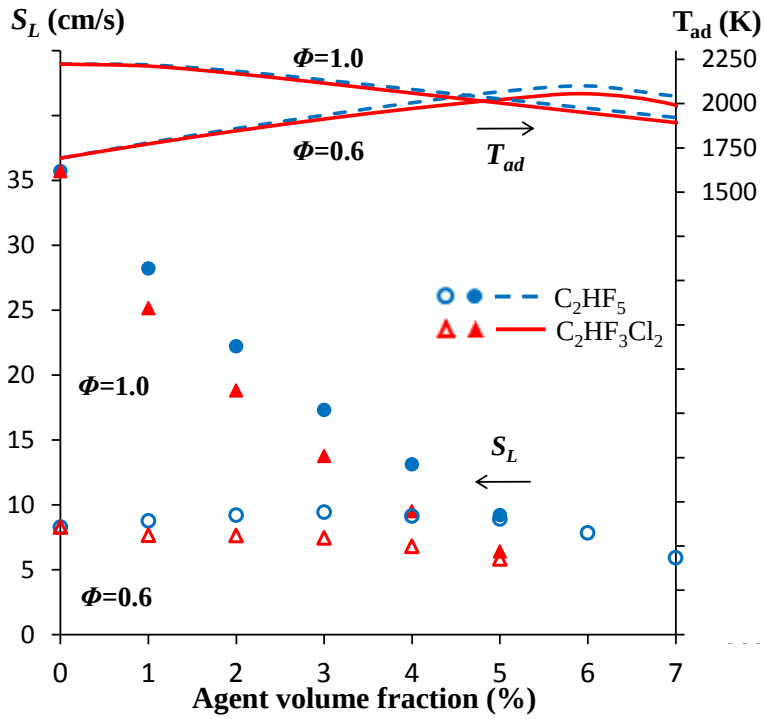

Figure 5.5: Burning velocity (lower data, left axis) and equilibrium flame temperature (upper data, right axis) for $C_2HF_3Cl_2$ (triangles) or C_2HF_5 (circles) added to stoichiometric (closed symbols) and lean (open symbols) CH_4-air. The solid and dashed lines represent the flame temperatures with added $C_2HF_3Cl_2$ or C_2HF_5.

4.2.3 Equilibrium and Peak Chain-Carrier Radical Concentrations

Burning velocity is known to be correlated with the peak radical (particularly OH) concentration in flames [23, 167, 168]. Hence, equilibrium and peak concentrations of chain-carrier radicals (H, OH, and O) are examined to compare the kinetic inhibition effectiveness of $C_2HF_3Cl_2$ and C_2HF_5. Figure 5.6 presents the chain-carrying radical volume fractions for $C_2HF_3Cl_2$ (solid lines) and C_2HF_5 (dotted lines) added to

stoichiometric (left frames) and lean (right frames) CH_4-air flames. For uninhibited flames at stoichiometric conditions, the peak values of [H], [OH], and [O] are 0.006, 0.008, and 0.003, or about 16, 3, and 14 times the equilibrium values. As either agent is added, the equilibrium radical concentrations decrease similarly as X_a increases. The peak values decrease as either agent is added, however, all peak radical volume fractions decrease less rapidly than do the equilibrium values with C_2HF_5 addition, but more rapidly with $C_2HF_3Cl_2$ addition. That is, addition of $C_2HF_3Cl_2$ causes the peak radical volume fractions to approach the equilibrium values, while addition of C_2HF_5 causes them to diverge from the equilibrium values. This is consistent with the stronger reduction in burning velocity with addition of $C_2HF_3Cl_2$ as seen in Figure 5.5 (and with the catalytic cycle described for Cl [18], which drives the radical volume fractions to equilibrium values)

At lean conditions (right frames), the uninhibited flames (X_a=0) have peak radical volume fractions somewhat lower than (but close to) those of stoichiometric flames (volume fractions of 0.0005, 0.0025, and 0.0011 for H, OH, and O, or about 12, 3, and 2.5, times lower than the stoichiometric flames). Moreover, the equilibrium radical volume fractions are much lower than the peak values in the lean flames, about 1,960, 9, and 130 times, leading to greater radical super-equilibrium for the neat lean flames at Φ=0.6 than at Φ=1.0. The effect of addition of either agent on the equilibrium radical volume fractions is very similar at low concentrations ($X_a \leq 0.05$), increasing the equilibrium value by a factor of about 15, 5, and 10 (at $0.05 \leq X_a \leq 0.06$ as compared to X_a=0) for H, OH, and OH, and then decreasing it rapidly for $X_a > 0.05$ (C_2HF_5) and $X_a > 0.06$ ($C_2HF_3Cl_2$).

For the equilibrium radical volume fractions, the behavior above X_a=0.05 is different for C_2HF_5 and $C_2HF_3Cl_2$, with [H] and [OH] dropping off earlier and faster for C_2HF_5 addition, but [O] dropping faster for $C_2HF_3Cl_2$ addition above X_a=0.06. This behavior is related to the ratio of halogen [X]=[F]+[Cl] in the system to hydrogen [H] ([X]/[H]), and the difference in equilibrium product species formed when adding the two agents. [X]/[H] is equal to 1 at the same value of X_a (0.05) for the two agents; when C2HF5 is added above X_a=0.05, there is not enough hydrogen to form the stable product HF. There is, however, some available hydrogen, in the form of H_2O, when $C_2HF_3Cl_2$ is added slightly above X_a=0.05 (for which [X]/[H] is slightly greater than 1) because a substantial amount of Cl is present in the equilibrium products (X_{Cl} = 0.015), whereas with added C_2HF_5, [F] is much lower ($X_F \approx 10^{-5}$). When adding either C_2HF_5 or $C_2HF_3Cl_2$, once hydrogen in no longer available, the resulting product species change, affecting both the final temperature and the equilibrium radical volume fractions. Thus, with added C_2HF_5, equilibrium [H] and [OH] start to drop off earlier than with added $C_2HF_3Cl_2$, because of formation of the very stable species HF. Regardless, despite the slower drop-off in equilibrium [H] and [OH] with added $C_2HF_3Cl_2$, the peak [H] and [OH] (as well as peak [O]) drop more rapidly because the chlorine catalytic radical recombination cycle drives the radical toward equilibrium more effectively than does the radical trapping mechanism of C_2HF_5. This is illustrated in the reaction flux analyses described below.

For the stoichiometric case, the unity hydrogen to halogen ratio occurs at X_a=0.08 ([X]/[H]=1 at X_a=0.08), so the radical volume fractions decrease at a relatively steady slope in Figure 5.6; i.e., because [X]/[H] is less than 1 for the entire range of X_a shown.

The peak radical volume fractions are affected differently with addition of the two agents in the lean flames as compared to addition to the stoichiometric flames. For example, in the stoichiometric flames (left frames, upper curves in each frame of Figure 5.6), both agents tend to lower peak radical volume fractions at increasing X_a, but the effect is somewhat stronger for $C_2HF_3Cl_2$ addition. For Φ=0.6 (right frame, upper curves of Figure 5.6) the peak radical volume fractions decrease mildly for X_a<0.06 and sharply at X_a>0.06 (at which [X]/[H] ≈ 1). In fact, for C_2HF_5 addition below X_a≈0.06, the peak radical volume fractions all *increase* in concentration. The reasons for this behavior become clearer after examination of the flux of reactions producing and consuming radicals, described below.

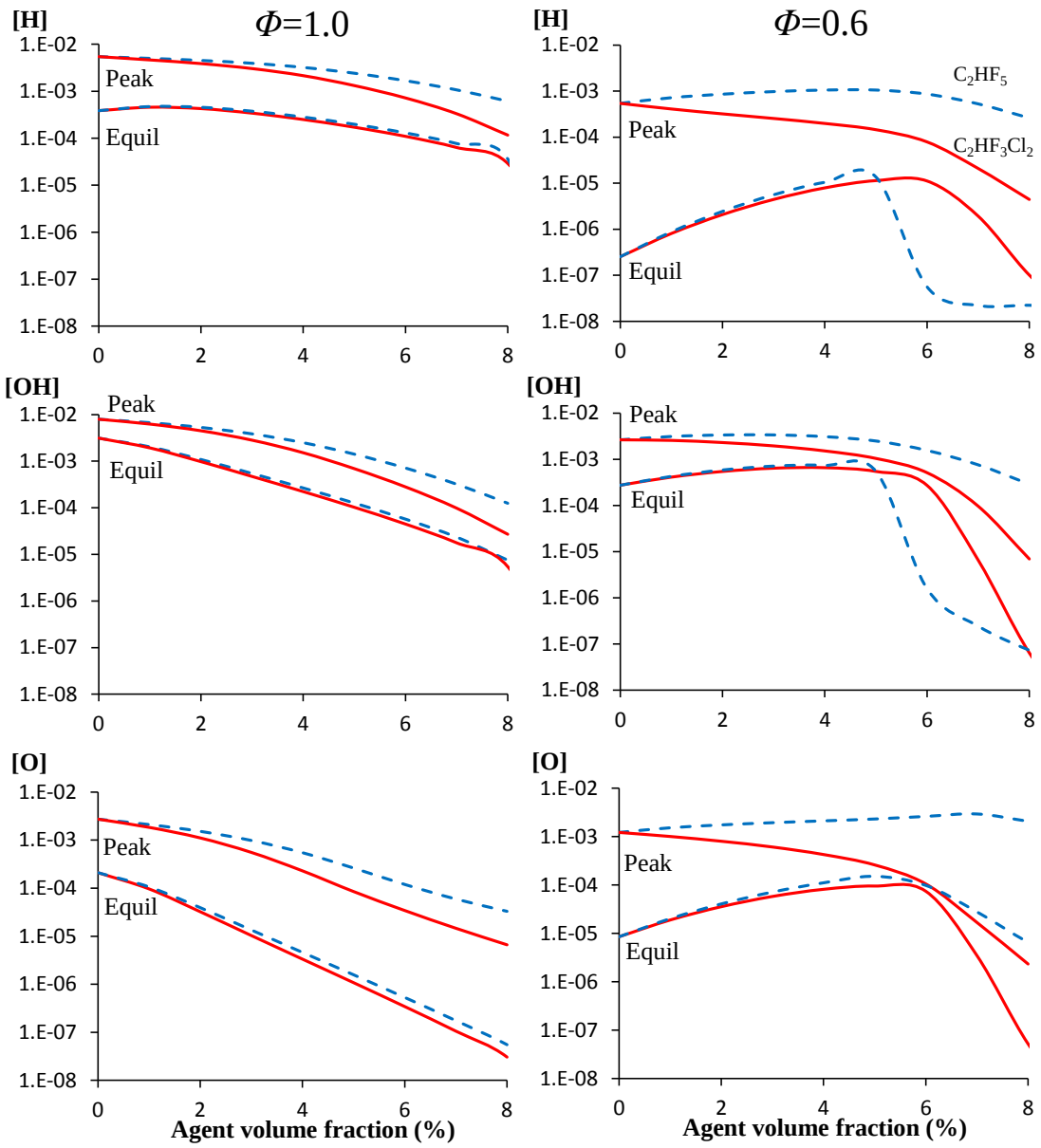

Figure 5.6: Equilibrium and peak radical concentrations ([H], top; [OH], middle; [O], bottom) in CH_4-air flames (Φ=1.0, right frames; Φ=0.6, left frames) with added $C_2HF_3Cl_2$ (solid lines) and C_2HF_5 (dotted lines).

5.2.4 Rate of Production Analysis

Figure 5.7 and Figure 5.8 present the halogenated reactions involved in the production and consumption of [H], [OH], and [O] in stoichiometric (left frame) and lean (right frame) CH_4-air with $C_2HF_3Cl_2$ (Figure 5.7) and C_2HF_5 (Figure 5.8) added at X_a=0.05. The rates of production (left axes, units: mol/cm^3-s) are shown as a function of position in the flame. Only the most important halogenated reactions are shown, with $H+O_2=O+OH$ included for reference and scaled by a factor of 2.5 to improve clarity. The overall generation rate of radicals is lower with $C_2HF_3Cl_2$ compared to C_2HF_5 (as a result of the chlorine catalytic cycle). Consequently, the peak rates of production/consumption by radical reactions with halogenated species are also lower with $C_2HF_3Cl_2$ (note the different scales in Figure 5.7 and Figure 5.8).

We consider first the stoichiometric flames. With added $C_2HF_3Cl_2$, the primary production/consumption reactions for H, OH, and O involve HCl, with smaller contributions from reactions of CF, CF_2 and CFCl, which form CF_2:O and HF and regenerate HCl. When adding either $C_2HF_3Cl_2$ or C_2HF_5, the primary reactions containing fluorinated species responsible for radical consumption are $CF_2+H=CF+HF$, $CF_2+OH+CF_2:O+HF$, and $CF_2+O=CF:O+F$. The rates of these reactions are only roughly a factor of 3 lower than the branching reaction $H+O_2=OH+O$, showing the dominant role of the halogen reactions in the flame chemistry. At this loading of either agent, F atom attacks water, abstracting an H atom to form HF and OH, with a rate similar to that of the halogenated reactions reducing chain-carrier radical concentrations.

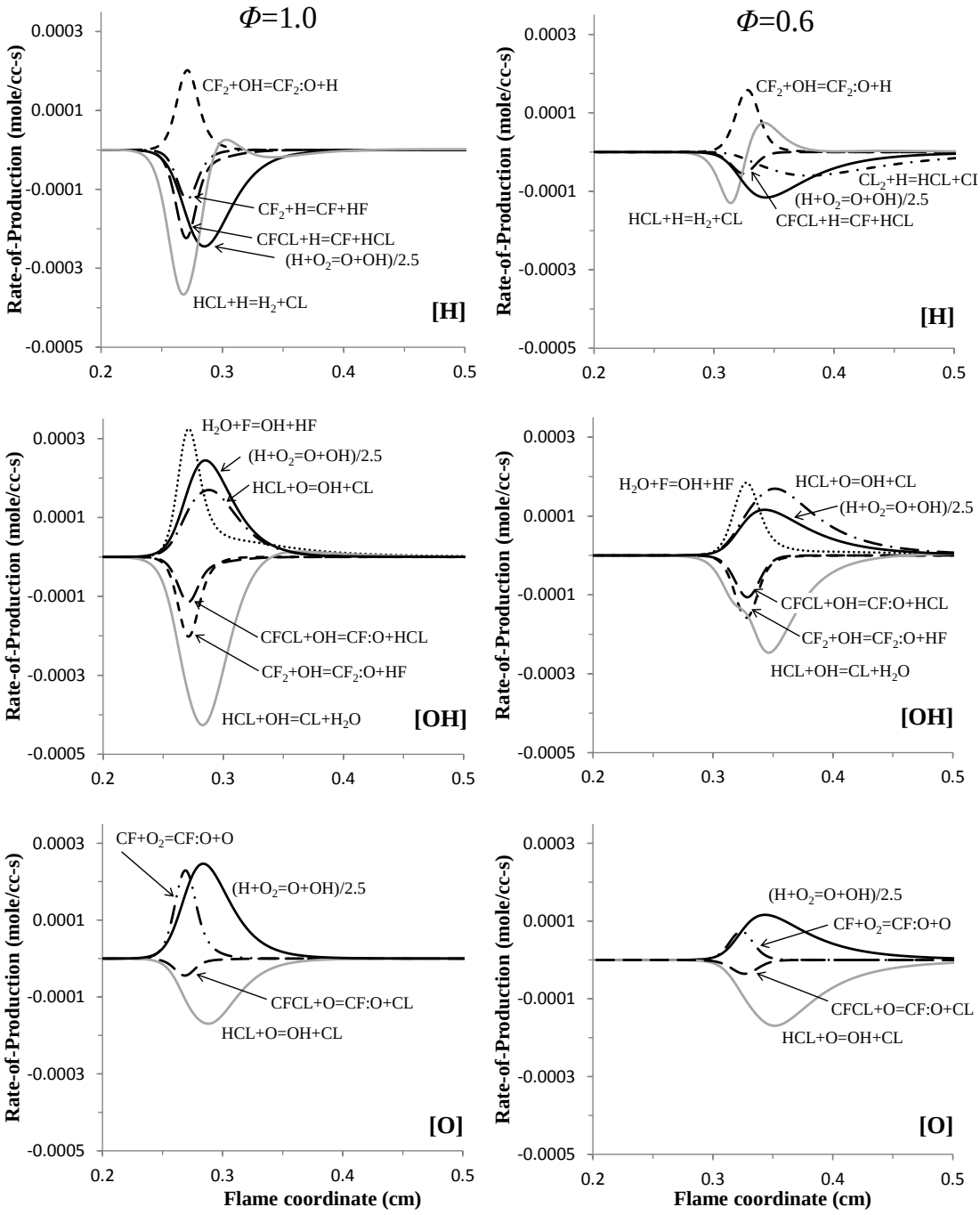

Figure 5.7: Rate of production/consumption of chain-carrier radicals ([H], top; [OH], middle; [O], bottom) in CH_4-air flames (Φ=1.0, right frames; Φ=0.6, left frames) with $C_2HF_3Cl_2$ added at X_a=0.05.

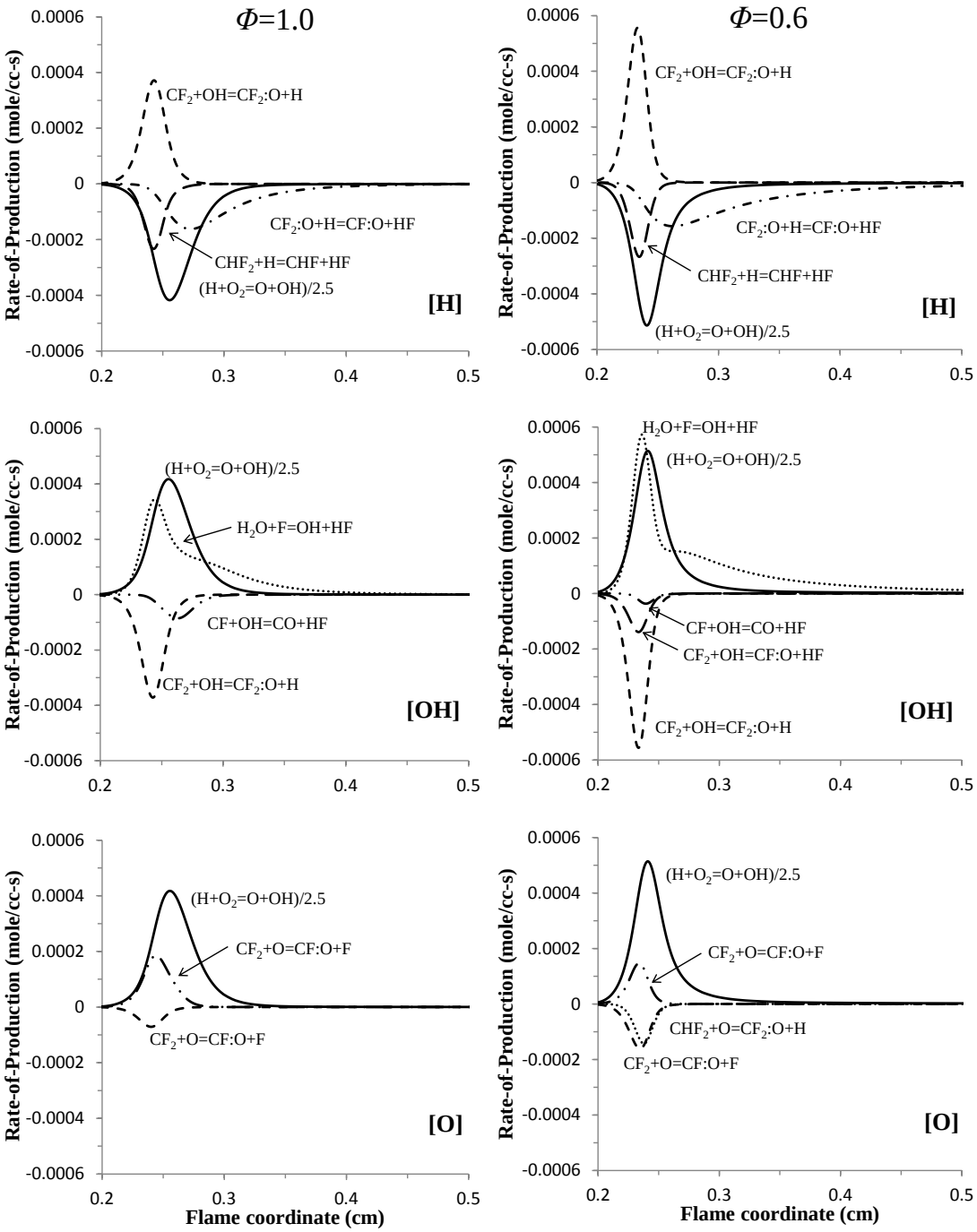

Figure 5.8: Rate of production/consumption of chain-carrier radicals ([H], top; [OH], middle; [O], bottom) in CH_4-air flames (Φ=1.0, right frames; Φ=0.6, left frames) with C_2HF_5 added at X_a=0.05.

For the lean flames (Φ=0.6), the primary production/consumption reactions are similar to those observed for the stoichiometric case, although the peak rates are lower. The reaction HCl+H=H_2+Cl, which mostly consumes H in the stoichiometric flames, behaves differently in the lean flames. There, the net effect is neutral: in the preheat zone of the flame zone the reaction consumes H atom, and then as the temperature increases, the reaction produces nearly the same amount of H atom (illustrating the shift in equilibrium with temperature for this key reaction in the Cl inhibition mechanism). Since the temperature of the lean and stoichiometric flames are about the same at X_a=0.05, the forward rate is favored in the stoichiometric flames due to the much higher [H] which also causes the peak rate of [H] consumption by HCl+H=H_2+Cl to be factor of 3 higher at stoichiometric conditions (compared to Φ=0.6). At lean conditions, the primary chlorinated reaction reducing [H] is Cl_2+H=HCl+Cl, which has broad profile that tracks [H]. Peak consumption of [H] by reaction with CFCl and CF_2 are also lower at lean conditions, with CF_2+H=CF+HF absent as a primary reaction. The reactions important for production/consumption of [OH] and [O] are similar to those for stoichiometric conditions, with consumption mainly through reactions involving HCl and CFCl and CF_2.

To quantify the overall effect of the chlorinated-species reactions vs. fluorinated-, the rates of production are integrated across the primary flame zone. The percentage of total consumption of radicals by reactions with chlorinated, fluorinated, and chlorofluorinated species are provided in Table 5.1. For $C_2HF_3Cl_2$ addition, reactions involving chlorinated species account for the largest reduction in radical concentration. Overall, reactions with halogenated species account for about 45 % of the H and OH destruction at stoichiometric and lean conditions, and 36 % and 73 % of O destruction,

for stoichiometric and lean conditions, respectively. Of these, reactions with chlorinated species are about three times more important than reactions with only fluorinated species. For C_2HF_5 addition, the halogen reactions (F species only) account for a lower fraction of the total radical consumption (roughly 20 to 40%) as compared to $C_2HF_3Cl_2$ addition, for both stoichiometric and lean conditions, which is consistent with the lower peak radical concentrations and higher burning velocity seen in Figure 5.5 and Figure 5.6 at X_a=0.05.

Table 5.1: Percentage of H, OH, and O radical consumption by reactions containing halogenated species (agent volume fraction of 0.05).

Agent	% of H Cons.		% of OH Cons.		% of O Cons.	
Rxn Group	Φ=1.0	Φ=0.6	Φ=1.0	Φ=0.6	Φ=1.0	Φ=0.6
$C_2HF_3Cl_2$						
Cl rxns	20	24	30	30	25	59
F rxns	16	13	12	13	7	9
F-Cl rxns	10	6	5	6	4	5
Halogen rxns	46	42	46	48	36	73
C_2HF_5						
F rxns	34	40	19	26	14	32

There are competing effects when a suppressant containing a hydrocarbon portion is added to a lean flame [24, 29, 71]. The suppressant can react with excess oxygen, increasing the heat release and temperature, which in turn increases the overall reactivity of the system. The suppressant simultaneously introduces halogen atoms to the flame-zone reducing chain-carrier radical concentrations through chain-terminating reactions. When adding C_2HF_5 to the lean CH_4-air flame, the increase in heat release dominates, resulting in increased peak radical concentrations and S_u seen in Figure 5.5 and Figure 5.6. At a higher temperature (resulting from exothermic reaction of the suppressant), the

main chain branching reaction, $H+O_2=OH+O$, proceeds at a higher rate, producing more chain-carrier radicals than consumed by the chain-terminating reactions involving fluorine. With $C_2HF_3Cl_2$, the improved radical recombination ability of chlorine outweighs the increased rate of chain branching caused by the additional heat release, hence the reduction in peak radical concentrations and S_u for all X_a added to the lean flame. Also, because of the formation of Cl and Cl_2 in the products, the final flame temperature of the lean flames is lower with $C_2HF_3Cl_2$ addition than with C_2HF_5 addition. Thus, the $C_2HF_3Cl_2$ inhibited flames have less heat release (i.e., enhancement) and more inhibition (due to the effectiveness of the Cl cycle), making $C_2HF_3Cl_2$ a more effective inhibitor than C_2HF_5.

5.2.5 Sensitivity Analysis

Normalized sensitivity coefficients, in the form of logarithmic derivatives ($\delta \ln S_u / \delta \ln A_i$), are determined for stoichiometric and lean (Φ=0.6) CH_4-air flames with C_2HF_5 and $C_2HF_3Cl_2$ added at X_a=0.05 (for a positive sensitivity, increasing the Arrhenius pre-exponential factor A of that reaction increases S_u). In Figure 5.9, the halogenated reactions with highest absolute sensitivities are shown (with $H+O_2=O+OH$, scaled by 2.5, included for reference) for stoichiometric (black bars) and lean (dashed bars) flames with added C_2HF_5 (left frame) and $C_2HF_3Cl_2$ (right frame). Reactions involving fluorinated species are grouped at the top of each frame, followed by reactions with chlorinated species.

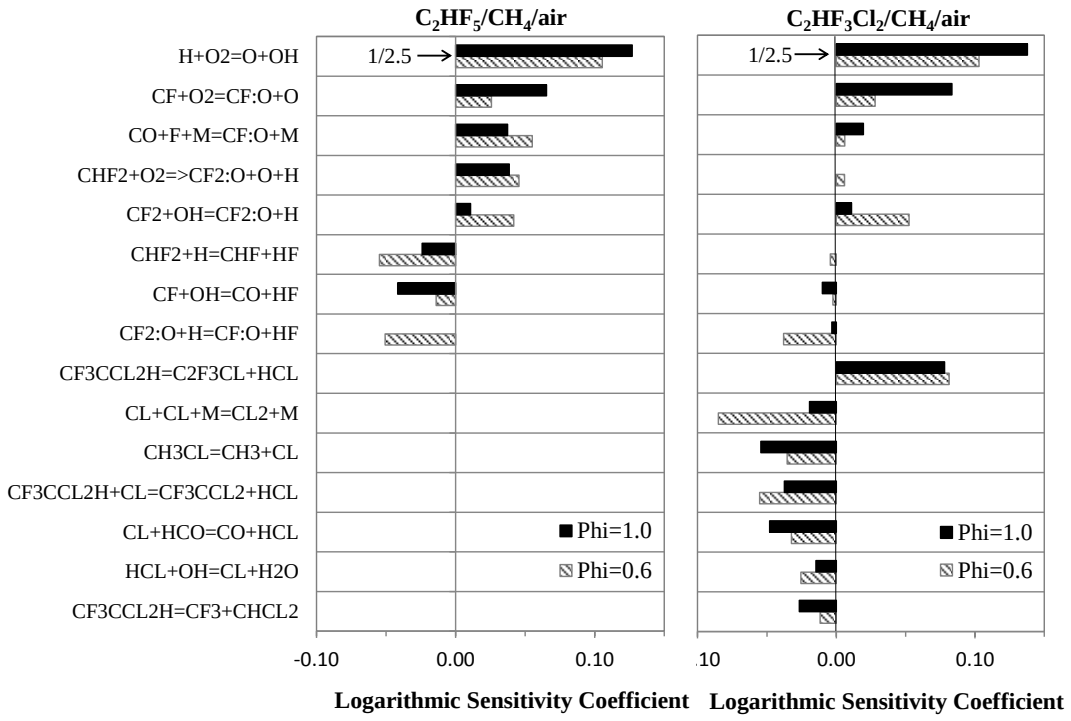

Figure 5.9: Sensitivity coefficients for stoichiometric and lean (Φ=0.6) CH_4-air flames with C_2HF_5 (left frame) and $C_2HF_3Cl_2$ (right frame) addition at a volume fraction of 5%.

With addition of C_2HF_5, S_u of the stoichiometric flame is generally increased by increasing rates of the fluorinated reactions CF+O_2=CF:O+O, CO+F+M=CF:O+M, CHF_2+O_2=CF_2O+O+H, and CF2+OH=CF_2O+H, which have comparable sensitivities, with the first the most important for stoichiometric flames, and all roughly equally important for lean. The first and third reactions are exothermic and chain-branching; the second is exothermic, and the fourth terminating but exothermic. The three fluorinated-species reactions with negative sensitivities all consume radicals (with CHF_2+H=CHF+HF and CF_2:O+H=CF:O+HF being roughly thermally neutral and CF+OH=CO+HF exothermic), and hence inhibit the flame, so increasing their rate

decreases the overall reactivity. In general, S_u of the lean CH_4-air flame is slightly more sensitive than the stoichiometric flame to reactions containing fluorinated species.

For addition of $C_2HF_3Cl_2$, Figure 5.9 (right frame) shows that the burning velocity is generally less sensitive to the fluorine-species reactions, with a few exceptions (e.g., CF+O_2=CF:O+O and CF_2+OH=CF_2:O+H have 30% higher sensitivities). Of the chlorine-species reactions, S_u is sensitive to three reactions of the initial breakdown of the inhibitor (which was not the case for C_2HF_5 addition), as well as two of the reactions in the catalytic radical recombination cycles (HCl+OH=Cl+H_2O, and Cl+HCO=CO+HCl). Conversely, the burning velocity is not sensitive to the rate of the reaction H+HCl=H_2+Cl, which is responsible for most of the H atom recombination (consistent with previous studies with CH_3Cl, CH_2Cl_2, $CHCl_3$, and CCl_4 added to CH_4-air flames [131-133]). The burning velocity of the lean (Φ=0.6) inhibited CH_4-air flame is sensitive to the important termination reaction for the catalytic cycle Cl+Cl+M=Cl_2+M; at stoichiometric conditions the sensitivity is about a factor of 4 lower. Lastly, both the lean and stoichiometric flames exhibit a negative sensitivity to the reaction CH_3Cl=CH_3+Cl (which increases [Cl] in the flame zone).

5.3 Conclusions

For reducing the undesirable heat release and over-pressure due to agent reaction in the FAA Aerosol Can Test, hydrochlorofluorocarbons (HCFCs) may have advantages over hydrofluorocarbons (HFCs) as fire suppressants. To understand the difference between these compounds, burning velocity measurements and numerical simulations with detailed chemistry were performed for CH_4-air flames with added $C_2HF_3Cl_2$ or

C_2HF_5. Comparisons of the experimental and numerical results also served as first steps in validating a newly-developed HCFC model.

Constant-volume combustion chamber experiments provided the burning velocity of CH_4-air mixtures at ambient (298 K; 1.01 bar) and compressed (400 K; 3 bar) conditions, with addition of C_2HF_5 or $C_2HF_3Cl_2$. For stoichiometric flames, both agents reduced the burning velocity by about a factor of three at an agent loading of X_a=0.05 (with somewhat faster inhibition by $C_2HF_3Cl_2$ at lower agent loadings). For lean flames (Φ=0.6) the same agent loading (X_a=0.05) had the opposite effect for the two agents: increasing S_u by about 10% for C_2HF_5, and reducing it about 10% for $C_2HF_3Cl_2$. Hence, unlike the HFC, the HCFC did not show the enhanced burning when added to the lean flame at ambient conditions.

For model validation, experiments with CH_4-air flames at equivalence ratios of 0.6, 0.9, 1.0, and 1.1 and $C_2HF_3Cl_2$ or C_2HF_5 at volume fractions up to around 5% provided data for comparison with numerical simulations. For the near-stoichiometric flames, agreement was generally very good. At lean conditions (Φ=0.6), agreement was good for $C_2HF_3Cl_2$ loading above about 2%, and C_2HF_5 loading above about 5%; while at low agent loading (and for uninhibited flames), the model over-predicted the burning velocity by about 3.5 cm/s (and the reason is believed to be radiative heat loss in the experiment, which is a higher fraction of the total heat release rate at the lean condition).

The numerical simulations provided flame structure data useful for understanding the action of the two agents. Addition of either agent to a stoichiometric flame reduced both the equilibrium and peak volume fraction of the chain-carrying radicals (H, OH, and, O), with a somewhat greater reduction in peak radical concentrations for addition of

$C_2HF_3Cl_2$ than addition of C_2HF_5). Chlorine is more effective in reducing peak H, OH, and O radical concentrations; hence, the greater reduction in burning velocity with added $C_2HF_3Cl_2$. For the lean flames at agent volume fractions below about 0.05, C_2HF_5 addition increased the peak radical volume fractions, whereas $C_2HF_3Cl_2$ reduced it, foretelling the results of the burning velocity. A reaction flux analysis highlighted the key reactions in the $C_2HF_3Cl_2$ inhibited system responsible for the greater reduction in peak [H], [OH], and [O] compared to C_2HF_5. The lower peak radical concentrations are the result of improved radical consumption by reactions containing chlorinated and chlorofluorinated species. In addition, a sensitivity analysis showed that, unlike the case for C_2HF_5 addition, the burning velocity is particularly sensitive to the rates of the initial $C_2HF_3Cl_2$ decomposition reactions.

Chapter 6: Premixed Flame Inhibition by CF_3Br and $C_3H_2F_3Br$

6.1 Introduction

Recent studies have modeled simplified flame structures with detailed chemistry to help interpret the FAA-ACT results [9, 10]. Equilibrium and perfectly-stirred reactor simulations were used to study the impact of CF_3Br, C_2HF_5, and $C_6F_{12}O$ on the total heat release and reactivity of the constant-volume system. Exothermic reaction of the alternative agents (C_2HF_5 and $C_6F_{12}O$) was found to add energy to the system, which not only increased the total heat release (and hence, the overpressure), but the reactivity as well (this was not the case with added CF_3Br). At the time of the analysis, kinetic mechanisms were available for flame inhibition by CF_3Br [32], C_2HF_5 [26], and $C_6F_{12}O$ [10] but not for $C_3H_2F_3Br$. Since then, Burgess et al. [134] developed the first kinetic mechanism describing the decomposition of $C_3H_2F_3Br$ in hydrocarbon-air systems (down to C2 bromine-containing species). During parallel work [71], the CF_3Br mechanism reported in ref. [32] was updated to include more accurate reaction rate data (Arrhenius coefficients) made available in literature since the original model was developed.

The objective of the present study is to provide experimental data for validation of the updated CF_3Br sub-model and the new $C_3H_2F_3Br$ sub-model, and to compare the inhibition performance of $C_3H_2F_3Br$ to CF_3Br for a wider range of premixed flame conditions and inhibitor concentrations than previously considered. Laminar burning velocity is selected as the validation metric because it is a fundamental property of a mixture that provides a good measure of reactivity (dependent on kinetics, thermochemistry, and transport properties). Unstretched laminar burning velocity and

flame response to stretch (characterized by the Markstein length) are determined from spherically expanding flames recorded via high-speed shadowgraph imagery. Experiments are performed with CF_3Br and $C_3H_2F_3Br$ added to premixed CH_4- and C_3H_8-air flames with initial equivalence ratios Φ of 0.6, 0.8, 1.0, and 1.2. Tests are performed with inhibitors added at volume fractions up to 3%, with reactant mixtures prepared at ambient temperature and pressure (298 K, 1 atm). Through consideration of Markstein lengths, the influence of added CF_3Br and $C_3H_2F_3Br$ on the flame response to stretch is examined. Lastly, a sensitivity analysis highlighting the reactions for which changes in the kinetic rate coefficients most strongly influence the calculated burning velocity is performed to guide future model refinement.

6.2 Results and Discussion

6.2.1 Comparing Agent Influence on Burning Velocity

Figure 0.1 presents the burning velocities (bottom curves) for premixed CH_4-air (left frames) and C_3H_8-air (right frames) flames with added CF_3Br (triangles) or $C_3H_2F_3Br$ (circles). Computed equilibrium adiabatic flame temperatures are shown by the solid and dashed lines for CF_3Br and $C_3H_2F_3Br$ respectively. The upper, middle and lower frames provide data for equivalence ratios of 1.2, 1.0 and 0.8 (based on the uninhibited mixture prior to agent addition).

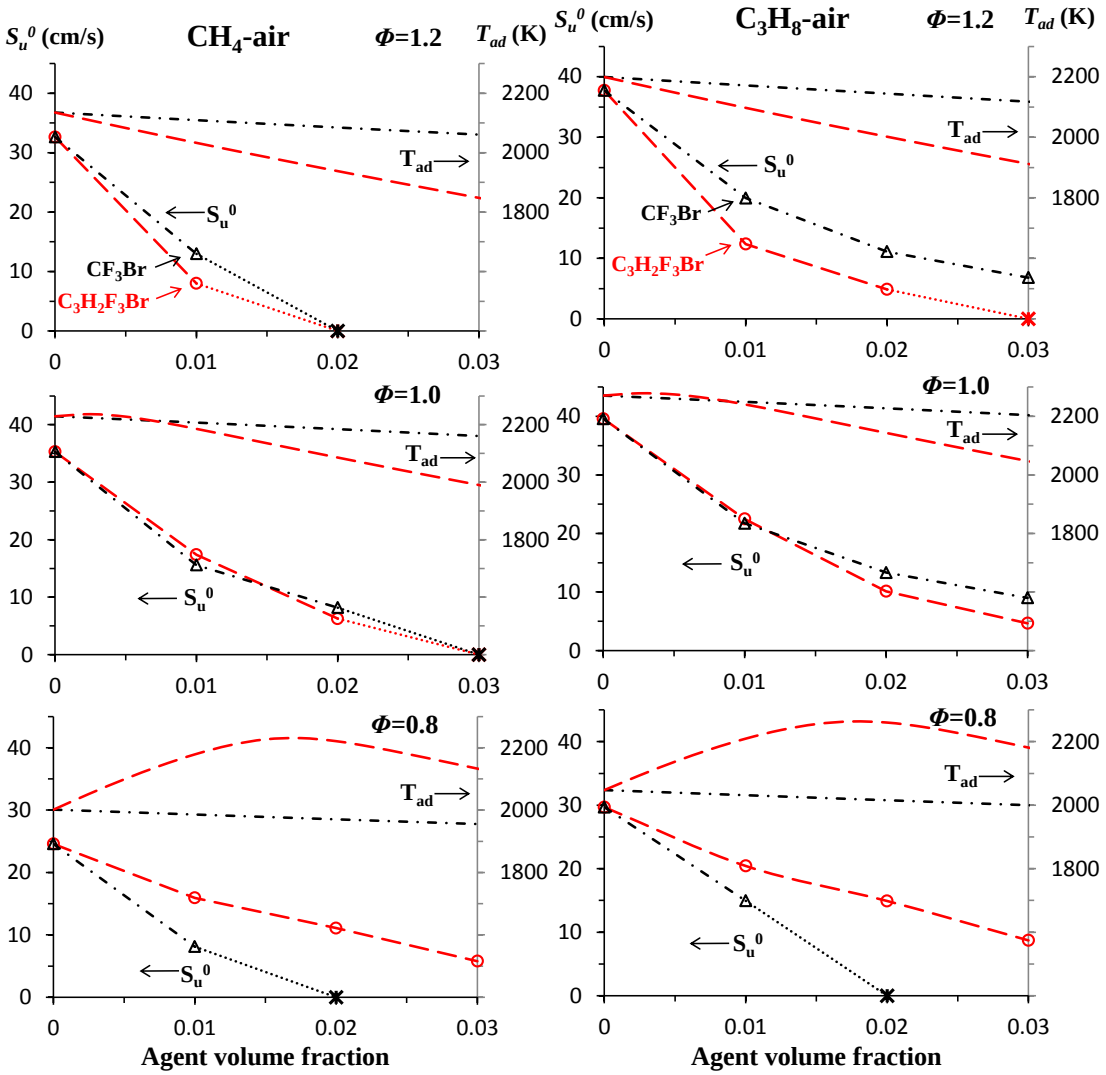

Figure 0.1: Laminar burning velocity S_u^0 (bottom curves, left axis) and adiabatic flame temperature T_{ad} (top curves, right axis) of CH_4-air (left frames) and C_3H_8-air (right frames) with added CF_3Br and $C_3H_2F_3Br$.

Rich cases (Φ = 1.2)

As shown in Figure 0.1, $C_3H_2F_3Br$ provides a larger reduction in both S_u^0 and T_{ad} as compared to CF_3Br; when added at $X_a = 0.01$ to CH_4-air mixtures, $C_3H_2F_3Br$ and CF_3Br respectively reduce S_u^0 by 75% and 60%, and T_{ad} by 4.8% and 1.2%. At $X_a = 0.02$, the computed T_{ad} for the $C_3H_2F_3Br$ inhibited mixture is 147 K lower than for the CF_3Br

case and both agents are found to prevent ignition[1]. Similar results are seen when adding the agents to the rich C_3H_8-air flames. For instance, $C_3H_2F_3Br$ lowers the burning velocity 38% and 56% more than CF_3Br at X_a = 0.01 and 0.02. For the same conditions, the reduction in T_{ad} is 74 K and 142 K larger with $C_3H_2F_3Br$. At X_a = 0.03, non-ignition occurs with $C_3H_2F_3Br$, whereas flame propagation was observed for the CF_3Br case with S_u^0 = 6.8 cm/s.

Stoichiometric cases

For the stoichiometric CH_4-air mixture, CF_3Br and $C_3H_2F_3Br$ provide similar reductions in burning velocity. While the flame adiabatic temperatures are similar for X_a < 0.01, the decrease of T_{ad} with the increase in agent volume fraction is much more pronounced in the case of $C_3H_2F_3Br$ (X_a > 0.01). For X_a = 0.03 T_{ad} is 170 K lower with $C_3H_2F_3Br$ than with CF_3Br, and both agents prevent ignition. Similar trends are again observed when adding agents to C_3H_8-air flames, although $C_3H_2F_3Br$ seems more efficient at reducing S_u^0 at higher agent loadings (X_a > 0.02).

Lean cases (Φ = 0.8)

At lean conditions, marked differences are observed in the efficiency of the two agents. CF_3Br provides a larger reduction in the burning velocity of lean flames, at all agent concentrations considered. 2% CF_3Br is found to prevent ignition of both CH_4-air and C_3H_8-air flames, whereas sustained flame propagations are still observed for 3%

[1] The phrase "prevent ignition" and term "non-ignition" are used throughout to identify conditions where a flame was either not observed or did not propagate throughout the entire viewing window when applying the maximum available ignition energy.

$C_3H_2F_3Br$, with corresponding burning velocities of 5.8 and 8.7 cm/s respectively. Note that for CF_3Br addition, the variation of T_{ad} across the X_a range is similar to those reported for the rich and stoichiometric cases (mild decrease via X_a increase). In contrast, the addition of $C_3H_2F_3Br$ has now a different effect on T_{ad}. When $C_3H_2F_3Br$ is added to either CH_4-air or C_3H_8-air, the adiabatic flame temperature increases by up to 200 K at X_a = 0.018 and further decreases at higher agent loadings.

The differences observed for CF_3Br and $C_3H_2F_3Br$ at lean and rich conditions deserve further scrutiny. It has been shown [18, 24] that the chemical inhibition by halogen-containing agents mainly proceeds through the recombination of active flame radicals (H, OH, O) by halogenated intermediates, hence lowering the overall flame reactivity. It is worth mentioning that for CF_3Br and $C_3H_2F_3Br$, molecular structures are very similar. Actual atomic concentrations of fluorine and bromine are respectively identical in inhibited systems at fixed X_a, regardless of the agent considered. Significant differences in the radical recombination processes that would explain results observed in Figure 0.1 are therefore excluded. Instead, it is thought that the additional fuel component (C_xH_y-) introduced via agent addition can explain these differences. This is further analyzed by defining an overall equivalence ratio $\Phi_{overall}$ that incorporates the agent fuel effect. $\Phi_{overall}$ is determined by writing the following balance equation for the fuel/agent/air system:

$$\rho C_aH_b + \alpha C_cH_dF_eBr_f + \gamma[0.21O_2 + 0.79N_2] = \beta CO_2 + \lambda HF + \mu H_2O + \delta Br + \eta N_2 \qquad (6.1)$$

Note that when fluorine is present, the main combustion products are dependent on the ratio of hydrogen to fluorine atoms ([F]/[H]). For the inhibited mixtures in this study, [F]/[H] is always less than unity, thus the only fluorinated species that needs to be

considered is HF (CFO_2 or CF_4 must be considered when H/F < 1). The stoichiometric proportion of air γ_{stoic} is found by performing balances on C, H, F, Br, and O atoms:

$$\gamma_{stoic} = \rho(a + b/4) + \alpha(c + d/4 - e/4) \quad (6.2)$$

$\Phi_{overall}$ is accordingly expressed as:

$$\Phi_{overall} = [(\rho + \alpha)/(\gamma_{actual})]/[(\rho + \alpha)/(\gamma_{stoic})] \quad (6.3)$$

The evolution of $\Phi_{overall}$ with agent addition ($C_3H_2F_3Br$ or CF_3Br) is provided in Figure 0.2 for C_3H_8-air and initial equivalence ratios of 0.8, 1.0 and 1.2. There is minimal change in the overall equivalence ratio when CF_3Br is added; at X_a=0.03 the overall equivalence ratio is 0.04 higher than the initial equivalence ratio. Conversely, as $C_3H_2F_3Br$ is added the overall equivalence ratio is shifted considerably toward rich conditions. For instance, the initially lean C_3H_8-air flame at Φ=0.8 reaches stoichiometry when $C_3H_2F_3Br$ is added at X_a~0.015. At X_a=0.03 overall equivalence ratios are higher than the initial equivalence ratios by 0.42. The results observed in Figure 0.2 are coherent with the inhibitor relative efficiencies inhibitors found in Figure 0.1. For the lean flame, the peak temperature with added $C_3H_2F_3Br$ occurs at the concentration corresponding to $\Phi_{overall}$=1. At lean conditions, CF_3Br increases T_{ad} as well as $\Phi_{overall}$ less than CF_3Br, and is more effective at reducing the burning velocity. At rich conditions, the higher inhibition efficiency is likely the result of the lower reactivity because of the shift in $\Phi_{overall}$ toward even richer conditions. The results shown in Figure 0.1 and Figure 0.2 illustrate the fuel effect of $C_3H_2F_3Br$ previously discussed in ref. [71].

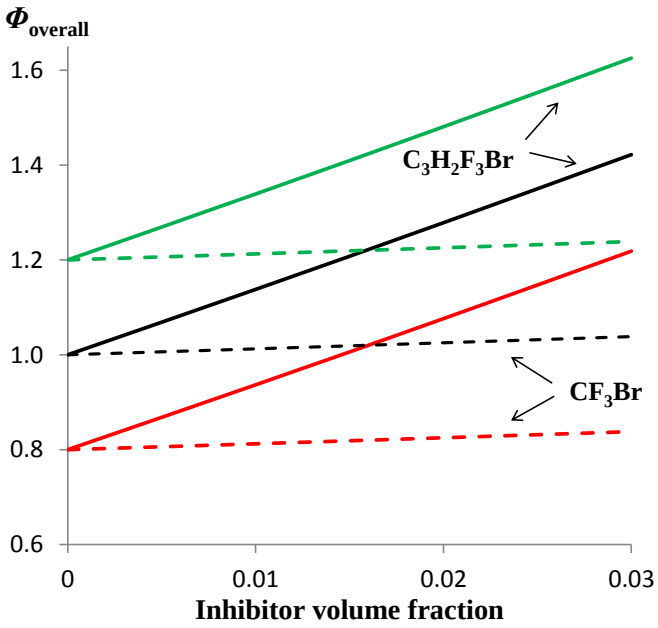

Figure 0.2: Overall equivalence ratio of C_3H_8-air flames as $C_3H_2F_3Br$ (dashed lines) or CF_3Br (solid lines) is added.

6.2.2 CF_3Br model validation

To validate the updated C1 brominated sub-mechanism, the experimentally measured burning velocities of CH_4-air (top frame) and C_3H_8-air (bottom frame) flames with added CF_3Br are compared to numerical predictions. Figure 0.3 shows the present experimental S_u^0 (symbols) together with the numerical predictions (lines), representing data at Φ = 0.6, 0.8, 1.0, and 1.2. Predictions for CH_4-air flames with added CF_3Br are in excellent agreement with the nonlinearly extracted S_u^0 data. At Φ = 0.8, 1.0, and 1.2, the predicted burning velocities are within 6%, 6.5%, and 8.5% of the measured results. Moreover, as shown in Figure 0.4, the non-linearly extracted S_u^0 for inhibited stoichiometric CH_4-air flames compare well with previously measured results [88, 150, 169], and with measurements made in the 1.85 L chamber. For C_3H_8-air flames, the

agreement between measured and predicted S_u^0 is similar to that observed for the inhibited CH_4-air flames. Numerical predictions slightly over-predict inhibition, but by less than 8% for most conditions, with the exception of Φ = 1.0 and X_a = 0.03 where the model over-predicts inhibition by 18%. When adding CF_3Br to CH_4- and C_3H_8-air flames at different equivalence ratios, the reduction in S_u^0 decreases as the agent concentration increases in both experiments and predictions, which is known as the saturation effect [34]. Although no burning velocity data could be collected for very lean (Φ = 0.6) inhibited flames, numerical predictions are provided to show the inhibition effectiveness of CF_3Br at these conditions. For both the CH_4-air and C_3H_8-air flames at Φ = 0.6, non-ignition occurred at the lowest concentration tested (X_a = 0.005).

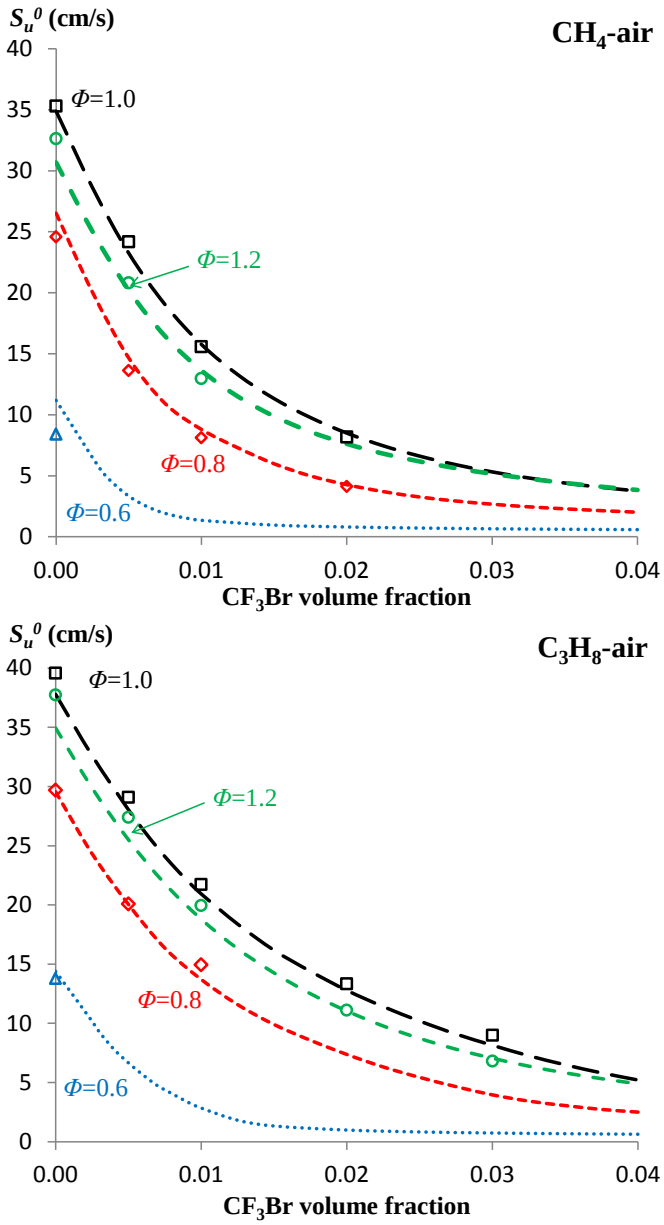

Figure 0.3: Comparison of experimental (symbols) and numerical (lines) S_u^0 for CF_3Br inhibited CH_4-air (top) and C_3H_8-air (bottom) flames at Φ = 0.6, 0.8, 1.0, and 1.2.

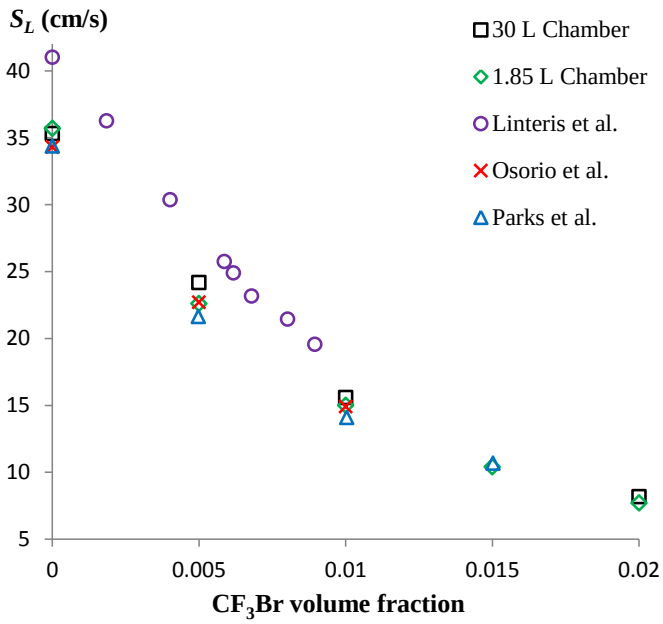

Figure 0.4: Burning velocity of stoichiometric CH_4-air with added CF_3Br, together with previously published results.

Recently, Osorio et al. [88] compared measured burning velocities of CF_3Br inhibited hydrocarbon flames with numerical predictions. Linearly extrapolated unstretched burning velocities were determined using the constant-pressure spherically expanding flame technique and predictions were made with the PREMIX code and a reaction mechanism comprised of the NUI-Galway mechanism [170] and the CF_3Br mechanism of ref. [32]. Burning velocity measurements were found to be consistently lower than predictions for CH_4-air and C_3H_8-air flames ($0.8 \leq \Phi \leq 1.2$) with CF_3Br added at X_a = 0.005 and 0.01. It was unclear whether the discrepancy was the result of inaccuracies in the original CF_3Br model [32] or bias associated with the linear method for extrapolating burning velocity to unstretched conditions (Previous studies have shown the importance of non-linear extrapolation for nonequidiffusive mixtures with Lewis numbers far from unity). Thus, to explore the source of discrepancy, the results of ref.

[88] are compared to the present results in Figure 0.5. Burning velocities as a function of equivalence ratio and agent concentration are shown for CH_4-air (left frame) and C_3H_8-air (right frame) flames with added CF_3Br. The dashed lines, open symbols, and stars show the present predictions, linearly extrapolated data, and non-linearly extrapolated data. The solid lines and closed symbols show the predictions and linearly extrapolated data from ref. [88].

As seen in Figure 0.5, the present uninhibited CH_4-air and C_3H_8-air (X_a = 0) burning velocity predictions and measurements (linear and nonlinear) are consistent with the previous work. Moreover, for the inhibited flames, the present linearly and non-linearly extracted burning velocities are similar, with the exception of the rich CH_4-air (Φ = 1.2) and lean C_3H_8-air (Φ = 0.8) flames containing 1% CF_3Br by volume. A 15% difference (~ 2 cm/s) in burning velocity is observed between the linearly and non-linearly extrapolated values. Furthermore, the linearly extrapolated results of ref. [88] agree well with the present experimental data (linear and non-linear). As shown in Figure 0.5, burning velocity measurements from both studies are much closer to the present predictions using the updated CF_3Br mechanism proposed in ref [71]. Overall, the predictions of ref. [88] are 4-28% and 13-35% higher than the present non-linearly extracted S_u^0, while the present predictions fall within a ±9% of the extracted values. Thus, the updates[2] outlined in ref. [71] have significantly improved the accuracy of the CF_3Br model. The discrepancies between measurements and calculations reported in ref.

[2] The improved performance of the updated model is the result of the inclusion of more accurate kinetic rate data made available in the literature since the original model was developed. As summarized in ref. [71], Arrhenius rate coefficient data was updated for 1/3 of the 100 reactions contained in the model.

[88] are therefore related to the lower prediction capabilities of the previous model rather than the use of the linear extrapolation methodology.

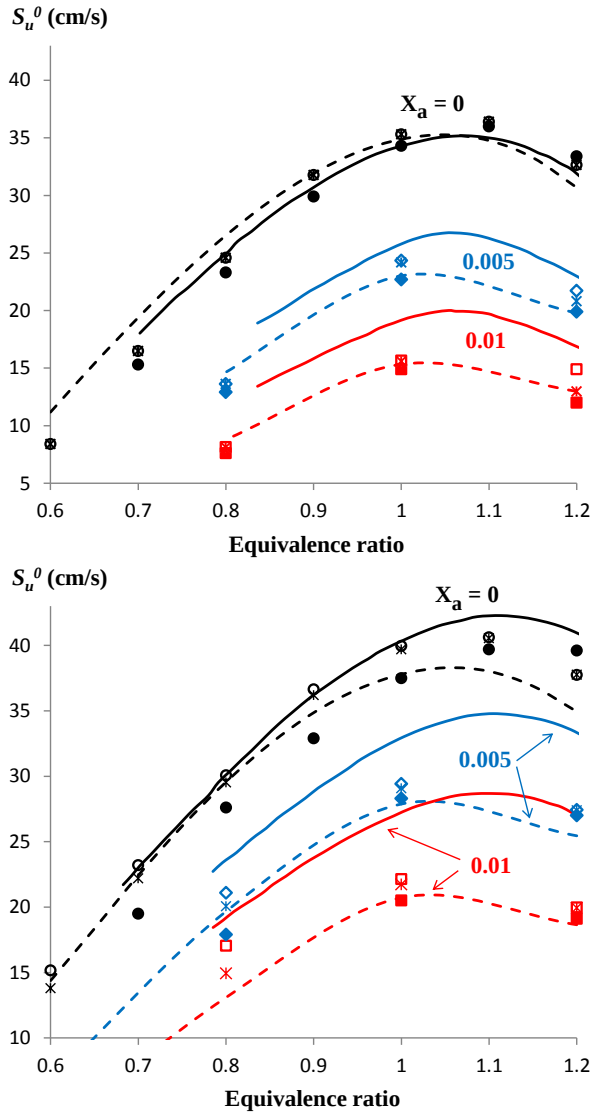

Figure 0.5: Comparison of present measured and predicted S_u^0 with those of Osorio et al. [88] for CH_4-air (top) and C_3H_8-air (bottom) flames with added CF_3Br. Open symbols and crosses represent the present linearly and non-linearly extracted S_u^0; solid lines represent the present predictions; closed symbols and dashed lines are the linearly extracted and predicted S_u^0 from ref. [88].

For certain mixtures, applying near-minimum ignition energy established a flame that extinguished soon after. When this occurred, the experiment was repeated with a higher energy until the flame successfully propagated through the entire viewing window. For other tests, such as CH_4-air at Φ = 1.2 with 2% CF_3Br, the maximum available ignition energy initiated reaction, but did not produce sustained propagation. Moreover, in contrast to the previously established rule-of-thumb that the flammability limit corresponds to a burning velocity of 5 cm/s [171, 172], non-ignition occurred for reactant mixtures with a wide range of predicted S_u^0 depending on the initial stoichiometry. (Although the predicted burning velocities at non-ignition conditions are not validated, they provide a reasonable estimate considering the agreement between experiments and predictions at near-limit conditions.) For instance, flame propagation was observed for lean CH_4-air (Φ = 0.8) with 2% CF_3Br and not for rich CH_4-air (Φ = 1.2) with 2% CF_3Br although the predicted planar burning velocities were 4.3 cm/s and 6.6 cm/s, respectively. In other words, the mixture with the lower predicted burning velocity successfully propagated through the viewing window and the mixture with the higher predicted burning velocity did not. Similar observations were made by Qiao et al. [100] when measuring burning velocities of CH_4-air flames diluted with chemically passive suppressants (N_2, Ar, CO_2, and He). For instance, successful flame propagation was observed for stoichiometric CH_4-air flames diluted with N_2, Ar, and CO_2 with predicted S_u^0 around 5 cm/s. On the contrary,, flame propagation was not observed for a He-diluted flame, even though the predicted S_u^0 was around 10 cm/s.

6.2.3 $C_3H_2F_3Br$ model validation

To validate the new $C_3H_2F_3Br$ (2-BTP) kinetic model, measured S_u^0 for CH_4- and C_3H_8-air flames with added $C_3H_2F_3Br$ are compared to predictions. For each fuel-air mixture, four different initial stoichiometries are considered (Φ = 0.6, 0.8, 1.0, and 1.2). Figure 0.6 presents the experimental S_u^0 (symbols) with the numerical predictions (lines) for CH_4-air (top frame) and C_3H_8-air (bottom frame) flames. In addition, burning velocities of $C_3H_2F_3Br$ inhibited CH_4-air flames, determined using the 1.85 L chamber, are included as crosses (Φ=1.0) and stars (Φ=0.6). At the lean (Φ=0.6) and stoichiometric condition, the present and previous measurements agree within 7% and 12% respectively. With $C_3H_2F_3Br$ added to CH_4-air, the model predictions are within 9% and 6% of the experimental results for Φ = 1.0 and 1.2 respectively. For Φ = 0.8, the inhibition performance is over-predicted in the range $0.01 \leq Xa \leq 0.03$, with measured S_u^0 higher than predictions by 6-18% (the discrepancy increases as X_a increases). At Φ = 0.6, the model over-predicts inhibition performance by 25% (which is close to the measurement accuracy of ~ 2cm/s), but captures the non-monotonic behavior as the $C_3H_2F_3Br$ concentration increases; the flame speed initially drops up to X_a = 0.01, before it increasing for $0.01 \leq X_a \leq 0.03$, and finally decreases as more $C_3H_2F_3Br$ is added. Previous work with the BTP model [71] showed that the drop in S_u^0 at low concentrations, followed by the rise at higher concentrations, was the result of the competition between radical scavenging by the halogenated species (Br and F participate in chain terminating reactions) and the additional heat release associated with the decomposition of $C_3H_2F_3Br$ in the lean CH_4-air environment.

For C_3H_8-air, burning velocity predictions are within 7% of the experimental results for the stoichiometric and rich flames with added $C_3H_2F_3Br$, with the exception of the prediction for Φ = 1.2 and X_a = 0.02 which is higher by 22% (~ 1.3 cm/s). The model once again over-predicts inhibition performance at lean conditions; at Φ = 0.8, prediction accuracy decreases as X_a increases, the relative error in S_u^0 at X_a = 0.01, 0.02, and 0.03 being about 8%, 16%, and 26% respectively. At even leaner conditions (Φ = 0.6), we were unable to measure inhibited flame burning velocities; for tests performed at X_a = 0.005-0.02, applying the maximum available spark energy did not lead to successful flame propagation.

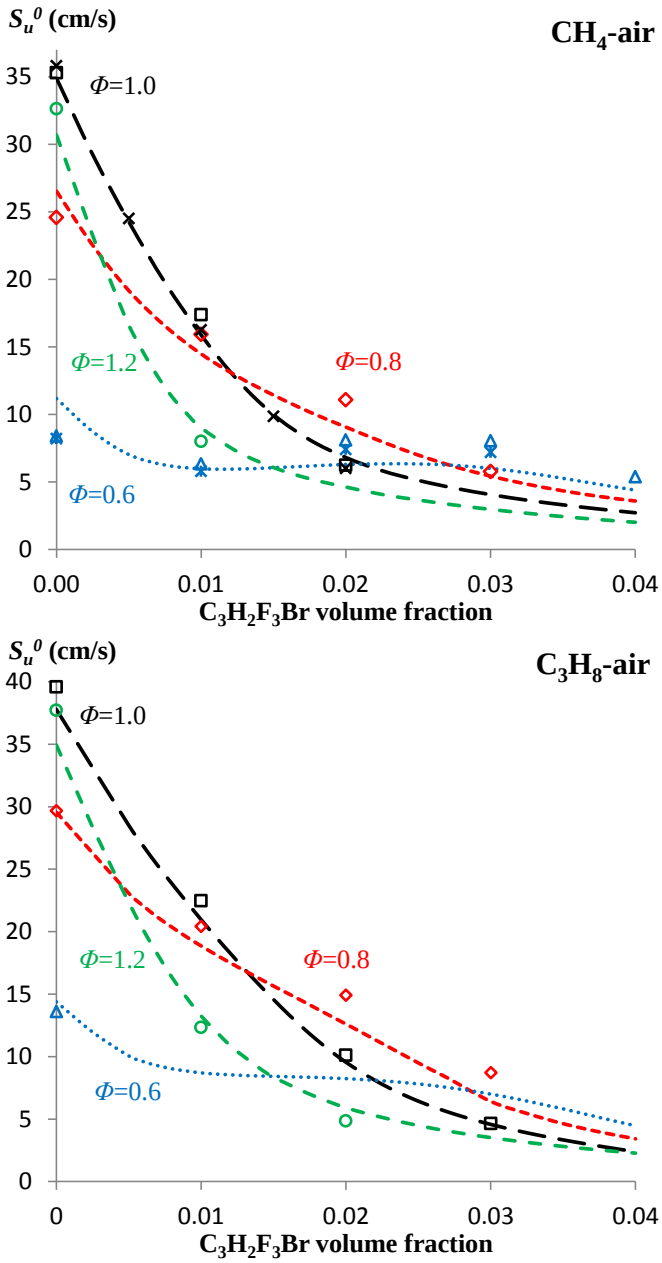

Figure 0.6: Comparison of experimental (symbols) and numerical (lines) S_u^0 for $C_3H_2F_3Br$ inhibited CH_4-air (top) and C_3H_8-air (bottom) flames at Φ = 0.6, 0.8, 1.0, and 1.2.

As previously discussed for CF_3Br, non-ignition occurred for inhibited mixtures with a range of predicted S_u^0. For inhibited C_3H_8-air at Φ = 0.6, flame propagation did not occur even though the predicted burning velocity is higher at all concentrations (Xa ≥

0.04) than for Φ = 1.0, X_a = 0.03 and Φ = 1.2, X_a = 0.02, for which flame propagation (and successful S_u^0 measurement) did occur. For certain mixtures, including inhibited lean C_3H_8-air (Φ = 0.6), the change in the response to stretch may cause stretch-induced quenching during the early stages of flame growth, as was the case in ref. [100] when adding chemically passive suppressants to stoichiometric CH_4-air flames. To interpret the influence of inhibitors on the flame response to stretch, Markstein lengths are examined in the following section.

6.2.4 Agent influence on Markstein length and stability

Figure 0.7 shows the non-linearly extracted burned gas Markstein lengths L_b for CH_4-air flames (left frames) and C_3H_8-air flames (right frames) with added CF_3Br (top) and $C_3H_2F_3Br$ (bottom). The different symbols represent data at different Φ and the Markstein lengths for each Φ are shown as a function of agent volume fraction. As observed previously in the literature, the Markstein length of uninhibited CH_4-air and C_3H_8-air increases and decreases respectively as the equivalence ratio increases. Opposite trends exist because the diffusivity of CH_4/C_3H_8 is higher/lower than the diffusivity of air [40]. Figure 0.7 shows that the influence of CF_3Br on the flame response to stretch is not only dependent on the fuel and the agent concentration, but also on the initial equivalence ratio considered. L_b increases as the concentration of CF_3Br increases in the rich CH_4-air flame (Φ = 1.2), whereas L_b decreases as the concentration of CF_3Br increases in the lean flame (Φ = 0.8); the opposite holds when added to C_3H_8-air. For the lean CH_4-air (Φ = 0.8) and the rich C_3H_8-air (Φ = 1.2) flames with X_a = 0.01, the Markstein lengths are around 3.5 mm and 4 mm, which are similar in magnitude to the Markstein lengths

measured for extremely rich ($\Phi \approx 7$) H_2-air flames [173], highlighting the strong sensitivity of the inhibited flames to stretch.

As seen in Figure 0.7, $C_3H_2F_3Br$ generally affects the Markstein length differently than CF_3Br. When added to the CH_4-air flames, $C_3H_2F_3Br$ increases the L_b of the rich and stoichiometric conditions. For the lean flames, L_b changes non-monotonically as the concentration of $C_3H_2F_3Br$ increases and seems to peak at the concentration coinciding with the maximum S_u^0. For both $\Phi = 0.6$ and $\Phi = 0.8$ the peak L_b occurs at $X_a = 0.02$ before dropping back down at higher concentrations to near the uninhibited value. Non-monotonic behavior has been observed if refs. [174-176] when adding H_2 to CH_4-air flames, and was attributed to changes in the both the mixture Lewis number and overall activation energy as the concentration of H_2 increased [175]. When added to the C_3H_8-air flames, $C_3H_2F_3Br$ reduces L_b of the rich and stoichiometric conditions, and again non-monotonically effects the Markstein length of the $\Phi = 0.8$ flame.

The influence of inhibitors on the sensitivity of the flame response to stretch explains why non-ignition occurred for inhibited mixtures with a range of predicted S_u^0. For spherically expanding flames with positive/negative burned gas Markstein lengths, the burning velocity increases/decreases toward the planer 1-D burning velocity as the stretch rate decreases (i.e. as the flame radius increases). Hence, when L_b is positive the flame propagation is slowest at small flame radii, and as L_b gets larger, a critical flame radius must be reached for sustained propagation to occur [97]. A well-established flame can form early on and then quickly extinguish because the supplied ignition energy is not sufficient to drive the flame to the critical radius. In some cases, the ignition energy was powerful enough to initiate reaction but could not drive the flame to the critical radius.

When higher ignition energies were available, the same mixture could be driven beyond the critical radius and flame propagation beyond the viewing window occurred. Partial flame propagation was observed (when applying the maximum available ignition energy) for rich CH_4-air (Φ = 1.2) and lean C_3H_8-air (Φ = 0.8) with added CF_3Br at X_a = 0.02. For these mixtures, a flame propagated roughly 1.5 cm before extinction occurred. Apparently, the critical radius for these mixtures is larger than 1.5 cm, which is roughly a factor of 3 larger the critical radius determined for rich H_2-air flames (Φ = 5.1 and P = 1 atm) in ref. [97]. As seen in Figure 0.7 for the rich CH_4-air and lean C_3H_8-air flames with added CF_3Br, L_b increases sharply as the concentration of CF_3Br increases and most likely continues to increase up to X_a=0.02, hence the large critical flame radius required and the strong influence of agent on the mixture Lewis number (as the Lewis number increases, the critical flame radius and minimum ignition energy increase significantly [177]).

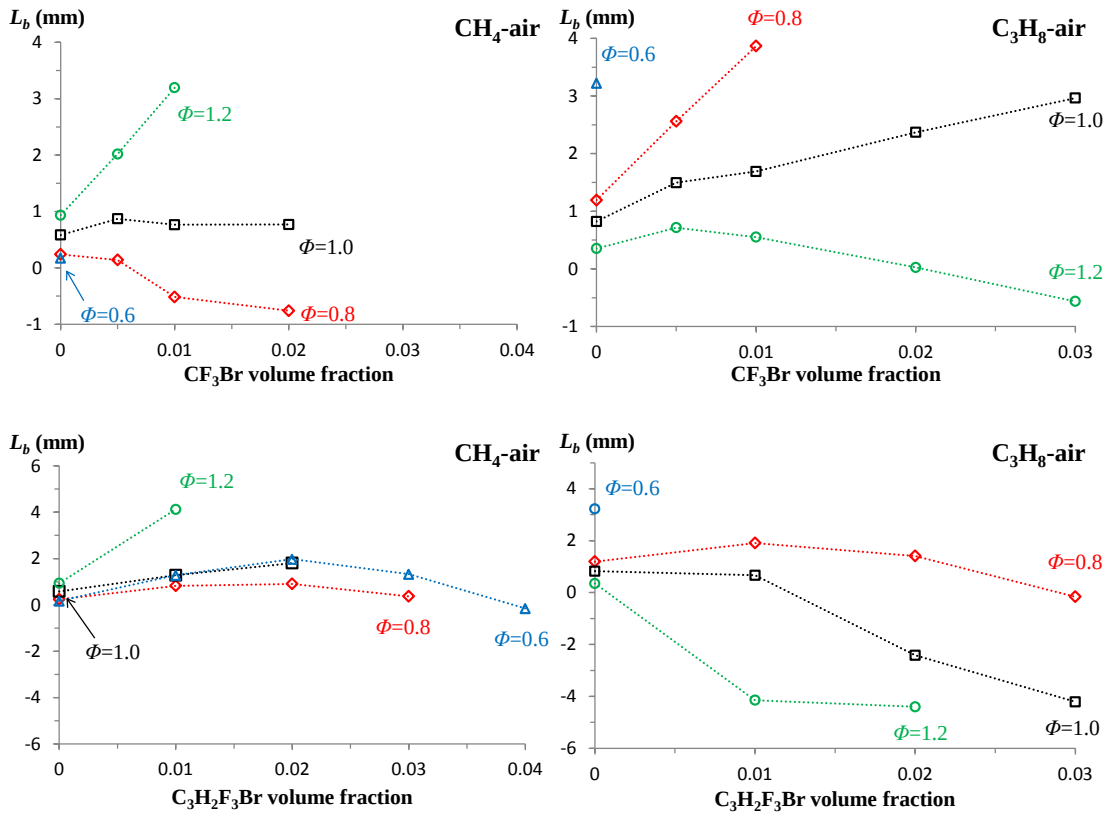

Figure 0.7: Burned gas Markstein lengths for CH_4-air (right frames) and C_3H_8-air (left frames) with added CF_3Br (top) and $C_3H_2F_3Br$ (bottom).

The burned gas Markstein length not only shows how the propagation speed changes with the stretch rate, it is also a measure of the susceptibility of a flame to diffusional-thermal instability [40]. Kim et al. [138] added CF_3Br to H_2-air flames at equivalence ratios Φ = 0.8, 1.0, and 1.8 and found that the flame stability decreased as the inhibitor concentration increased regardless of the fuel-air ratio, causing the flames to wrinkle and promoting transition from laminar to turbulent propagation. As the wrinkles grow the surface area of the flame sheet increases and the flame burning rate increases. Thus, the reduced stability resulting from agent addition is undesirable as it offsets the reduction in the flame burning rate that occurs through chemical inhibition [138].

Currently, no data are available on how chemically active suppressants influence the stability of hydrocarbon-air flames, especially with added $C_3H_2F_3Br$. As seen in Figure 0.7, adding CF_3Br or $C_3H_2F_3Br$ can increase or decrease flame stability depending on the fuel, the initial equivalence ratio, and the agent concentration (if adding an inhibitor changes the Markstein length from positive to negative it makes the flame more unstable). Adding CF_3Br decreases the stability of the lean (Φ = 0.8) CH_4-air flame and the stoichiometric and rich (Φ = 1.2) C_3H_8-air flames. At the concentrations considered, $C_3H_2F_3Br$ has minimal influence on the stability of the stoichiometric and lean CH_4-air flames. When added to the C_3H_8-air mixtures, the flame stability is expected to decrease for Φ = 1.0 and 1.2 and slightly increases for Φ=0.8 at X_a=0.01 before decreasing at higher concentrations. Thus, in contrast to what was observed in ref. [138], the Markstein lengths, and hence flame stability, are not always reduced as an inhibitor is added.

6.2.5 Sensitivity analysis

Normalized sensitivity coefficients in the form of logarithmic derivatives ($\delta \ln S_u / \delta \ln A_i$) are determined for CH_4-air flames with added CF_3Br and $C_3H_2F_3Br$. A positive normalized sensitivity coefficient indicates an increase in the Arrhenius pre-exponential factor A increases S_u^0, and vice versa. In Figure 0.8, the halogenated reactions with the highest absolute sensitivities are shown for stoichiometric CH_4-air flames with CF_3Br (grey bars) and $C_3H_2F_3Br$ (black bars) added at X_a = 0.03. Among the most sensitive reactions are those involved in the catalytic recombination cycle for H_2. Numerous reactions participating in both the recombination of H_2 and the generation of

HBr are among the most sensitive brominated reactions. In general, the CF_3Br inhibited flame is more sensitive to reactions involving brominated species. Moreover, it is more sensitive to the top three reactions because the concentration of hydrocarbon fragments that serve as alternative paths for HBr and BR_2 formation is lower than in the $C_3H_2F_3Br$ inhibited flame. As observed previously [33], Br + HCO = HBr + CO is an important reaction for the formation of HBr in both the CF_3Br and $C_3H_2F_3Br$ inhibited flames.

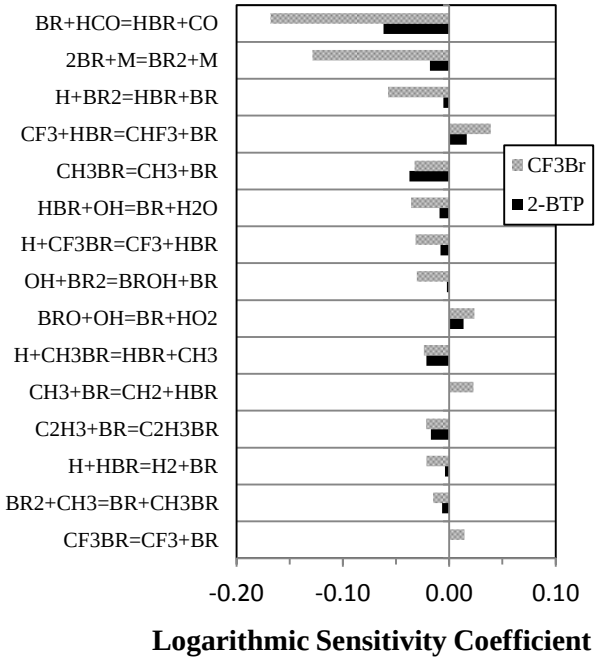

Figure 0.8: Sensitivity coefficients for stoichiometric CH_4-air flames with CF_3Br and $C_3H_2F_3Br$ addition at a volume fraction of 3%.

Figure 0.9 shows the influence of stoichiometry on the sensitivity of burning velocity to brominated reactions for CH_4-air flames with $C_3H_2F_3Br$ added at X_a = 0.03. At rich conditions, higher sensitivity is seen for the reactions involving larger hydrocarbon fragments because the concentration is higher in the rich flame compared to the stoichiometric and lean flames. Likewise the lean case is more sensitive to the 3 body

Br recombination reaction, Br + Br + M = Br_2 + M since there are less hydrocarbon fragments for Br to react with to form Br_2. Br2 is an important species that reacts with H to form HBr as part of the cycle. There is a mild positive sensitivity to the initial decomposition reaction BTP + CF_3 = CF_3CCH_2 + CF_3Br for all fuel-air ratios.

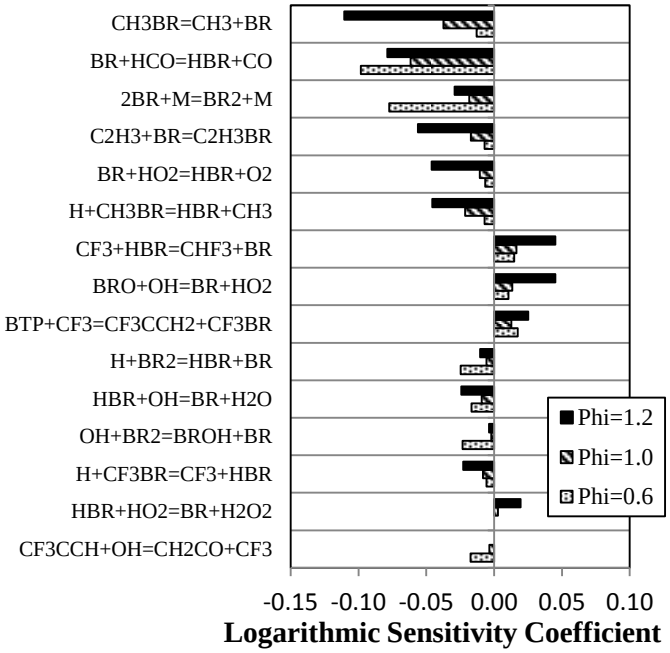

Figure 0.9: Sensitivity coefficients for CH_4-air flames varying in equivalence ratio with CF_3Br addition at a volume fraction of 3%.

6.3 Conclusions

Unexpected over-overpressures occurred in the FAA Aerosol Can Test when the fire suppressant $C_3H_2F_3Br$ (2-BTP) was added. To aid in interpretation, researchers developed a kinetic model for inhibition by $C_3H_2F_3Br$ and updated the model for CF_3Br. In the present study, burning velocity measurements and numerical simulations with detailed chemistry were performed for inhibited CH_4-air and C_3H_8-air flames as a first approach in validating the models. Comparison of the inhibited flame burning velocities

highlighted differences in performance and the conditions for which each agent was most effective. In addition, the influence of CF_3Br and $C_3H_2F_3Br$ on the flame response to stretch was elucidated.

Spherically expanding flame experiments provided the unstretched burning velocity and flame response to stretch (Markstein lengths) of premixed CH_4- and C_3H_8-air flames with addition of CF_3Br and $C_3H_2F_3Br$. For rich flames, $C_3H_2F_3Br$ more effectively reduced the unstretched burning velocity because, in addition to introducing halogenated radical scavengers, it shifts the overall equivalence ratio further away from stoichiometry (i.e. the fuel effect). At stoichiometric conditions, the inhibitors caused a similar reduction in the burning velocity on a molar basis for both the CH_4-air and C_3H_8-air flames. At lean conditions, CF_3Br was far more effective because $C_3H_2F_3Br$ shifts the overall mixture toward stoichiometric proportions and increased the adiabatic flame temperature by about 200 K, whereas the temperature remained nearly constant with added CF_3Br.

Experiments with CH_4- and C_3H_8-air flames at equivalence ratios of 0.6, 0.8, 1.0, and 1.2 with added CF_3Br or $C_3H_2F_3Br$ at volume fractions up to $X_a = 0.04$ provided data form comparison with numerical models. Excellent agreement was observed for the CF_3Br inhibited flames, highlighting the improved performance of the updated CF_3Br sub-model. Agreement was generally good for the $C_3H_2F_3Br$ inhibited flames considering the present study is the first test of the new $C_3H_2F_3Br$ sub-model. Inhibition performance was over-predicted by as much as 26% (~1.5 cm/s) at lean conditions, with improved performance observed at stoichiometric and rich conditions for both the CH_4- and C_3H_8-air flames.

The experiments provided the influence of inhibitor on the sensitivity of the flame response to stretch in terms of the burned gas Markstein length. The data showed that the influence of inhibitor the flame/stretch interaction was dependent on the inhibitor, the hydrocarbon fuel, and the initial equivalence ratio. Both CF_3Br and $C_3H_2F_3Br$ increased/decreased the Markstein length of CH_4- and C_3H_8-air flames and in some cases L_b changed non-monotonically as the concentration of $C_3H_2F_3Br$ increased. The influence of inhibitor on the flame response to stretch helped to explain the variation in the predicted S_u^0 at conditions where non-ignition occurred. In some cases, adding inhibitor made L_b so large that sustained propagation could not be achieved because of the greatly reduced flame speed at small radii. In addition, the Markstein lengths showed that adding inhibitors can increase or decrease diffusional-thermal instabilities in flames, again depending on the inhibitor, fuel, and initial stoichiometry.

Lastly, a sensitivity analysis highlighted the bromine-containing reactions for which changes in the rate coefficients most strongly influences the predicted burning velocities of inhibited CH_4-air at Φ = 1.0. The flame inhibited by CF_3Br was generally more sensitive to the brominated reactions, especially those involving the formation of HBr. The effect of equivalence ratio on the sensitivity of S_u^0 to brominated reactions was examined from CH_4-air with added $C_3H_2F_3Br$. Higher sensitivity to reactions involving hydrocarbon fragments was observed at rich conditions.

Chapter 7: Premixed Flame Inhibition by $C_6F_{12}O$ (Novec 1230)

7.1 Introduction

$C_6F_{12}O$ ($C_2F_5COC_3F_7$; FK-5-1-12; Novec 1230) is a clean agent fire suppressant (ODP=0, GWP=1) that has replaced CF_2BrCl (Halon 1211) in many total flooding applications and has potential to replace CF_3Br (Halon 1301) in the remaining critical-use applications. Currently CF_3Br is used in civilian cargo compartments, but the European Union has mandated replacement in new and existing aircraft by 2018 and 2040. Unfortunately, when tested by the Federal Aviation Administration in the Aerosol Can Test (abbreviated herein as FAA-ACT), sub-inerting concentrations of $C_6F_{12}O$ (as well as C_2HF_5 and $C_3H_2F_3Br$) caused the pressure rise to nearly double compared to the pressure rise of the base case with no added suppressant [4, 5].

A kinetic model for the decomposition of $C_6F_{12}O$ in hydrocarbon-air systems was developed [10] to help interpret the cause of over-pressures in the FAA-ACT. The model was used in conjunction with numerical simulations to examine the influence of added $C_6F_{12}O$ on the equilibrium products and the overall reaction rate of the FAA-ACT system [10]. Consistent with the large-scale results, the calculations showed that sub-inerting concentrations of $C_6F_{12}O$ increased the overall heat release. Moreover, sub-inerting concentrations reduced the overall reaction rate by several orders of magnitude compared to the uninhibited system, but apparently not enough to suppress the explosions. As a result of the unexpectedly low reactivity of the systems which managed to reach equilibrium (based on similar equilibrium and observed pressure rise), burning velocities were calculated to explore whether pure agents in air or oxygen could support

combustion [11]. The burning velocity of stoichiometric $C_6F_{12}O$-air at 400 K was calculated to be 0.367 cm/s, which was lower than the burning velocity of the three other alternative agents considered (CF_3H, C_2F_5H, C_3F_7H).

The influence of water vapor on the combustion of fluorinated compounds was examined [178], in part because of the high concentration of water vapor contained in the FAA-ACT (39% by volume of the aerosol can contents). In earlier studies, Kondo et al. [179-181] showed that, for several hydrofluorocarbon refrigerants, the flammability limits widen and the heat of combustion increases when water vapor is present in the oxidizer. The importance of the halogen to hydrogen ratio on the equilibrium products and overall reaction rate of systems containing fluorine was elucidated Thus experiments have shown enhancement and calculations have predicted increased overall reaction rates and burning velocities in the presence of water vapor but there has yet to be an experimental study explore whether water vapor increases burning velocity.

This study aims to provide validation of the $C_6F_{12}O$ kinetic sub-model; to examine the inhibition performance of $C_6F_{12}O$ when added to different hydrocarbon-air systems ranging in fuel-air equivalence ratios; and to examine the influence of water vapor on the inhibition performance of $C_6F_{12}O$ (i.e., the impact on burning velocity). To accomplish this, unstretched laminar burning velocities are determined from spherically expanding flames recorded via high speed shadowgraph imagery. Premixed flame experiments are performed with $C_6F_{12}O$ added to CH_4- and C_3H_8-air with equivalence ratios ranging from 0.6 to 1.2, and with $C_6F_{12}O$ concentrations up to 3% by volume. Tests are performed with reactant mixtures at 296 K and 1 atm and extrapolation to zero-stretch conditions is done with a non-linear method.

7.2 Results and Discussion

7.2.1 Inhibition Effectiveness Compared to CF_3Br

Laminar burning velocities of CH_4-air and C_3H_8-air flames inhibited with $C_6F_{12}O$ are compared to previously reported burning velocities for similar flames inhibited with CF_3Br [JLP BTP]. Fuel-air equivalence ratios Φ of 0.6, 0.8, 1.0, and 1.2 are considered with agents either added up to X_a=0.03 or to the concentration that prevents ignition[3]. Reported equivalence ratios are based on the uninhibited mixtures, with the fuel-air ratio is held constant as agent is added. Figure 0.1 shows the unstretched burning velocities S_u^0 and equilibrium adiabatic flame temperatures T_{ad} of CH_4-air (right frames) and C_3H_8-air (left frames) as a function of agent volume fraction. Rich flames (Φ=1.2) are shown in the top frames, with descending frames showing data at progressively leaner conditions.

Rich Flames (Φ=1.2)

For rich CH_4-air, $C_6F_{12}O$ steadily lowers T_{ad} from 2135 K (at the uninhibited conditions) to 1795 K at X_a=0.03, whereas T_{ad} is only slightly reduced to 2061 K with CF_3Br at X_a=0.03. Similarly, adding $C_6F_{12}O$ and CF_3Br at X_a=0.03 to the rich C_3H_8-air flame lowers T_{ad} from 2199 K (uninhibited) to 1860 K and 2117 K respectively. For the CH_4-air flame, the reduction in burning velocity is similar when adding either agent at X_a=0.01. At X_a=0.02, ignition is prevented with CF_3Br while flame propagation occurs

[3] As specified in Chapter 6, the phrase "prevent ignition" and term "non-ignition" are used throughout to identify conditions where a flame either did not for or did not propagate throughout the entire viewing window when the maximum available ignition energy was applied.

with $C_6F_{12}O$ with a corresponding S_u^0 of 5.8 cm/s. For the C_3H_8-air flame, the two agents provide a similar reduction in S_u^0 at all concentrations tested (X_a=0.01, 0.02, and 0.03). The larger reduction in T_{ad} with added $C_6F_{12}O$, and the comparable reduction in S_u^0 with the addition of either agent shows, the superior kinetic inhibition by CF_3Br, whereas $C_6F_{12}O$ is inhibiting thermally as a result of its higher heat capacity. Flame speed is known to correlate with chain-carrier radical concentrations [167, 168], which is a typical hydrocarbon-air system, are highly dependent on flame temperature. In the presence of halogens (particularly Br) the chain-carrier radical concentrations are reduced by the catalytic recombination cycles that take place. With added CF_3Br, the flame temperature is much higher but the chain-carrier radical concentrations are not because of the improved radical scavenging ability of CF_3Br.

Stoichiometric flames

For the inhibited stoichiometric flames, the adiabatic flame temperatures are similar up to an agent volume fraction of 0.01. At higher concentrations $C_6F_{12}O$ reduces T_{ad} more than CF_3Br and a difference in T_{ad} of 215 K is observed at X_a=0.03. For the CH_4-air flame, S_u^0 with added CF_3Br X_a=0.01 and X_a=0.02 is 30% and 35% lower than with added $C_6F_{12}O$ at the same concentration. When added to the stoichiometric C_3H_8-air flame, CF_3Br initially reduces S_u^0 4.5 cm/s and 2.4 cm/s more than $C_6F_{12}O$ at X_a=0.01 and 0.02, whereas at X_a=0.03, $C_6F_{12}O$ provides a larger reduction in the burning velocity (2.9 cm/s). The flame temperature gradually decreases at $0.01<X_a<0.025$ before the slope (dT_{ad}/dX_a) becomes steeper. At X_a=0.026 the halogen to hydrogen ratio is unity; at higher $C_6F_{12}O$ loadings, there is not enough hydrogen for all of the fluorine to form HF so other fluorinated products begin to form (COF2 and CF4), hence the change in

(dT_{ad}/dX_a). The saturation effect seems to occur (relative reduction in S_u^0 decreases as X_a increases) with added CF_3Br and not with $C_6F_{12}O$. In terms of $C_6F_{12}O$ as a CF_2BrCl replacement, Ref. [182] experimentally showed that CF_3Br and CF_2BrCl provide comparable levels of reduction in the burning velocity of premixed CH_4, C_2H_4, and C_3H_8 flames in air.

Lean flames (Φ=0.8 and 0.6)

At Φ=0.8, CF_3Br continues to slightly decrease the adiabatic flame temperature, whereas $C_6F_{12}O$ begins to affect T_{ad} differently. In contrast to when added to the rich and stoichiometric flames, $C_6F_{12}O$ increases T_{ad} of the CH_4- and C_3H_8-air flames by as much as 204 K and 197 K at X_a=0.02 and X_a=0.02 (compared to the uninhibited case) before reducing it at higher concentrations. For both hydrocarbon flames, T_{ad} begins to fall once [X]/[H]=1, as observed when adding $C_6F_{12}O$ to the stoichiometric C_3H_8-air flame (this was not observed for the stoichiometric CH_4-air flame or the rich flames because [X]/[H]=1 at X_a>0.03, which is off the figure). In terms of flame speed reduction, CF_3Br is more effective when added to either hydrocarbon-air flame at Φ=0.8. 2% CF_3Br prevents ignition of both CH_4 and C_3H_8 while at a similar $C_6F_{12}O$ loading S_u^0 is about 15 cm/s.

At the leanest conditions considered (Φ=0.6) CF_3Br continues to slightly decreases the adiabatic flame temperature of CH_4-air and C_3H_8-air while $C_6F_{12}O$ increases it by as much as 343 K and 300 K. For CH_4-air and C_3H_8-air at Φ=0.6 the [X]/[H] ratio reaches unity at X_a=0.02 and X_a=0.016 respectively. At higher $C_6F_{12}O$ concentrations T_{ad} initially drops and then increases again to near the peak temperature. 0.005% of CF_3Br prevents ignition of both the CH_4-air and C_3H_8-air flames while $C_6F_{12}O$

increases the burning velocity of the CH_4-air flame at X_a=0.01 and 0.02 and provides minimal reduction when added to the C_3H_8-air flame at X_a=0.01. The adverse effect when adding $C_6F_{12}O$ to lean flames is the result of the fuel component of the molecule. In the presence of excess oxygen, the suppressant reacts exothermically, raising the flame temperature and potentially the burning velocity if the increased chain-branching by $H+O_2=OH+O$ dominates over the chain-terminating ability of the added halogen. CF_3Br is a unique molecule that has minimal oxygen demand because there is enough oxidizer available in the H_2O that forms through hydrocarbon reaction in air [8, 9]. There is the exothermic reaction of $CF_3Br+2H_2O=CO_2+3HF+HBr$ which is outweighed by the increase in the mixture heat capacity as CF_3Br is added, hence the slight reduction in T_{ad}.

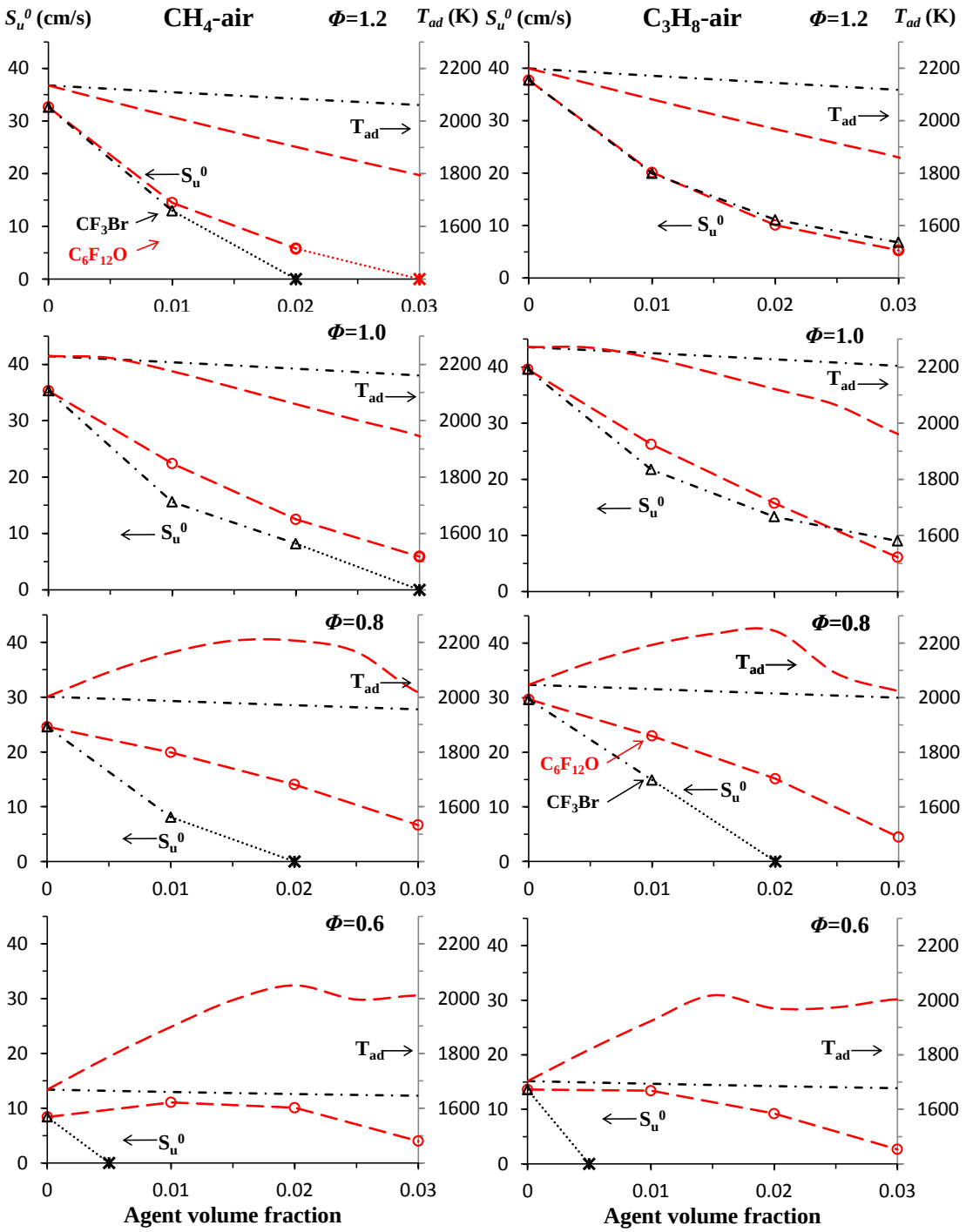

Figure 0.1: Laminar burning velocity S_u^0 (bottom curves, left axis) and adiabatic flame temperature T_{ad} (top curves, right axis) of CH_4-air (left frames) and C_3H_8-air (right frames) with added $C_6F_{12}O$ and CF3Br.

7.2.2 $C_6F_{12}O$ Model Validation

Figure 0.2 shows the measured and predicted burning velocities for CH_4-air flames at equivalence ratios Φ of 0.6, 0.8, 1.0, and 1.2 with added $C_6F_{12}O$ up to a volume faction X_a=0.03. The different symbols (measurements) and line styles (predictions) represent data at different Φ. In addition, Figure 0.3 compares the present measurements with the dataset of ref. [183], determined from the *constant volume* spherically expanding method. At lean (Φ=0.6) and stoichiometric conditions, the present and previous measurements agree within 4%, except at Φ=0.6 and X_a=0.03 where the present and previous burning velocities are 4.0 cm/s and 5.0 cm/s respectively. For the CH_4-air flames at Φ=0.8, 1.0, and 1.2, the burning velocity decreases as the concentration of $C_6F_{12}O$ increases; at 3% by volume, S_u^0 is roughly 1/2, 1/3, and 1/5 the uninhibited value for Φ=0.8, 1.0, and 1.2 respectively. For the Φ = 0.6 flame, adding $C_6F_{12}O$ at X_a=0.01 and 0.02 increases the measured S_u^0, which is successfully predicted by the kinetic model. Once X_a=0.03, both the measured and predicted burning velocities drop below the uninhibited burning velocity. Among the entire CH_4-air data set, the largest discrepancy between predictions and measurements (2.8 cm/s) occurs for the uninhibited flame at Φ=0.6. The model over-predicts burning velocity with agreement improving to 0.7 cm/s when $C_6F_{12}O$ is added at X_a=0.02. At X_a=0.03 the model once again over-predicts burning velocity by 1.6 cm/s In general, the predictions and measurements are in excellent agreement. For Φ=0.8, 1.0, and 1.2 predictions are within 8%, 11%, and 6% of the measurements for the range of $C_6F_{12}O$ concentrations considered ($X_a \leq 0.03$).

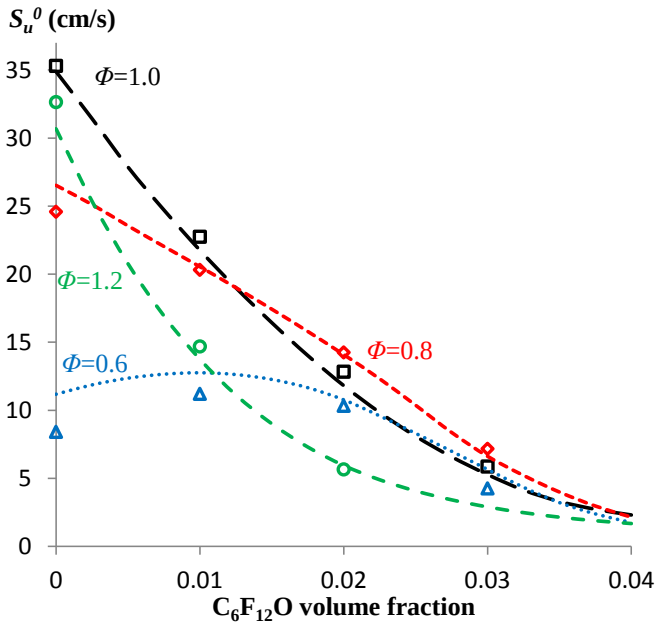

Figure 0.2: Comparison of experimental (symbols) and numerical (lines) S_u^0 for $C_6F_{12}O$ inhibited CH_4-air flames at Φ=0.6, 0.8, 1.0, and 1.2.

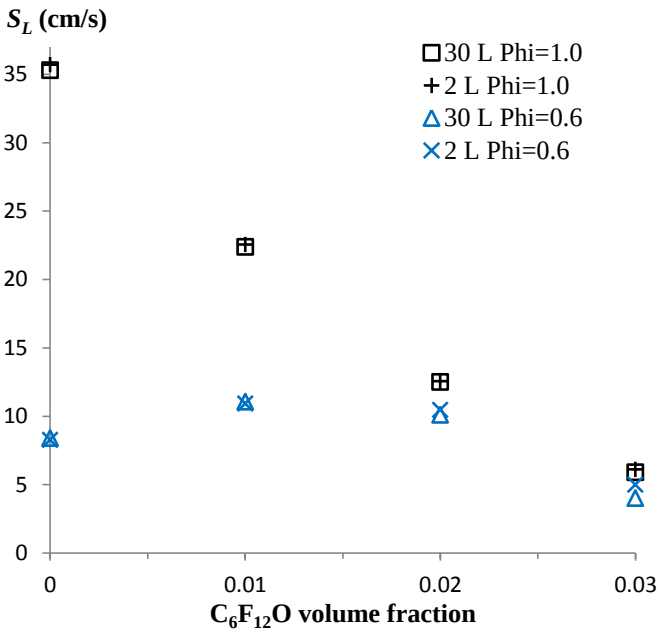

Figure 0.3: Burning velocity of stoichiometric CH_4-air with added $C_6F_{12}O$ measured in the 30 L and 1.85 L chambers.

Figure 0.4 presents the S_u^0 measurements and predictions for C_3H_8-air flames at Φ=0.6, 0.8, 1.0, and 1.2 with $C_6F_{12}O$ added up to X_a = 0.03. At Φ = 1.0 and 1.2, model predictions agree well with the measured burning velocities, with a maximum difference of ±15% between the two. For Φ=0.8, predictions are within 5% for $C_6F_{12}O$ loadings up to X_a=0.02, whereas at X_a=0.03 the predicted burning velocity is about 80% higher than the measured result (8.0 cm/s compared to 4.8 cm/s). At Φ=0.6, the uninhibited burning velocity prediction is 14.4 cm/s and compares well to the measured value of 13.6 cm/s. As $C_6F_{12}O$ is added, the model under-predicts suppression performance; predicted burning velocities are 13-130% higher for $0.01 \leq Xa \leq 0.03$, with the discrepancy increasing as the concentration increases. Comparisons between the measurements and predictions show that model performance could be improved when higher concentrations of $C_6F_{12}O$ are added to lean C_3H_8-air flames.

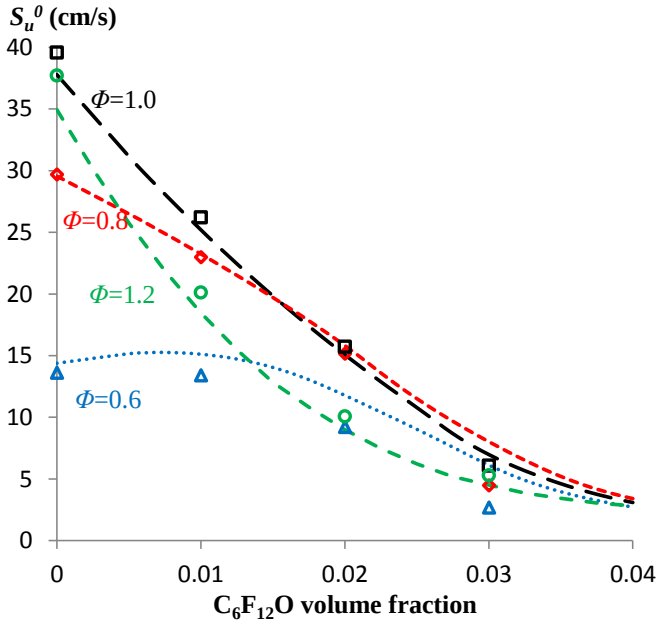

Figure 0.4: Comparison of experimental (symbols) and numerical (lines) S_u^0 for $C_6F_{12}O$ inhibited C_3H_8-air flames at Φ=0.6, 0.8, 1.0, and 1.2.

7.2.3 Influence of Water Vapor on Inhibition Effectiveness

Previous studies have shown the flammability limits of hydrofluorocarbon refrigerants to be sensitive to water vapor present in the oxidizer (i.e., the relative humidity of air) [179-181]. Furthermore, fluctuations in the relative humidity were found to impact the equilibrium pressure rise and overall reaction rate in perfectly stirred reactor calculations pertaining to the FAA-ACT [8-10]. Motivated by the previously mentioned findings, ref. [178] modeled CH_4-air flames inhibited with C_2HF_5 and found the burning velocity to increase/decrease with added water vapor depending on the [F]/[H] ratio [178]. In addition to the known influence of water on fluorinated combustion, the FAA-ACT presents a unique fire scenario in the sense that the fuel is comprised of 39% liquid water by volume (5.87 moles of ethanol, 2.05 moles of propane,

and 5 moles of liquid water). To explore whether the presence of water vapor may be effecting the inhibition performance of $C_6F_{12}O$ when added to hydrocarbon-air flames, burning velocities are measured and calculated for lean C_3H_8 flames (Φ=0.6) in air at a relative humidity of 0 and 1 (at 23 °C) and with $C_6F_{12}O$ added up to X_a=0.03. The lean flame is considered because it is consistent with the conditions occurring in the FAA-ACT [10] and because test mixtures containing with a [F]/[H]>1 are still flammable.

Figure 0.5 presents burning velocity measurements (symbols) and predictions (lines), along with equilibrium adiabatic flame temperatures (dashed lines) for C_3H_8 flames at Φ=0.6 in saturated and dry air as a function of $C_6F_{12}O$ concentration. The dotted vertical line represents the $C_6F_{12}O$ concentration for which the [F]/[H] ratio of the dry flame is unity (X_a=0.016). For both the wet and dry cases, the burning velocity predictions are consistently higher than the measurements (0.8-3.5 cm/s), but the two exhibit similar trends as the concentration of $C_6F_{12}O$ increases. When the $C_6F_{12}O$ concentration is less than 0.013 ([F]/[H]<0.8), H_2O acts as a suppressant; for these conditions, T_{ad} of the wet flame is consistently lower by 8-10 K. For the uninhibited case (X_a=0.0), the predicted and measured burning velocities of the wet flame are 0.7 cm/s 1.0 cm/s lower than for the dry flame. At X_a=0.01 ([F]/[H]=0.62) the measured S_u^0 is similar for the two cases (~13.3 cm/s) and the prediction for the dry flame is slightly faster. When X_a=0.013 and [F]/[H]=0.8 the model predicts similar burning velocities (~14.6 cm/s). At higher $C_6F_{12}O$ concentrations when [F]/[H]>0.8, the water in the oxidizer begins to enhance the burning velocity. As observed in ref. [178], the enhancement occurs when the [F]/[H] ratio is slightly less than unity. At higher concentrations (Xa≥0.013) the model predicts faster burning velocities for the wet case, with S_u^0 9% and

32% higher at X_a=0.02 and 0.03. As seen in Figure 0.5, the measured burning velocities at X_a=0.02 and 0.03 are about 2.1 cm/s higher for the wet case. The model slightly under-predicts the enhancement by H_2O at X_a=0.02, but nevertheless predicts faster burning velocities for the saturated mixture when $C_6F_{12}O$ is added at X_a>0.013 and the [F]/[H] is greater than 0.8. It is interesting to note that the T_{ad} of the wet flame is only higher than that of the dry flame for a narrow range of $C_6F_{12}O$ loading ($0.016 \leq X_a \leq 0.034$). Although at higher X_a the adiabatic flame temperatures are similar, the model continues to predict a higher burning velocity for the wet case. As shown in ref. [178], the reaction $H_2O+F=HF+OH$ is not only highly exothermic (increasing the flame temperature), OH is formed as result, which is among the most active chain-carrier radicals. The additional pathway for the formation of OH is likely the cause of the increased burning velocity when the $C_6F_{12}O$ concentration is larger than X_a~0.03.

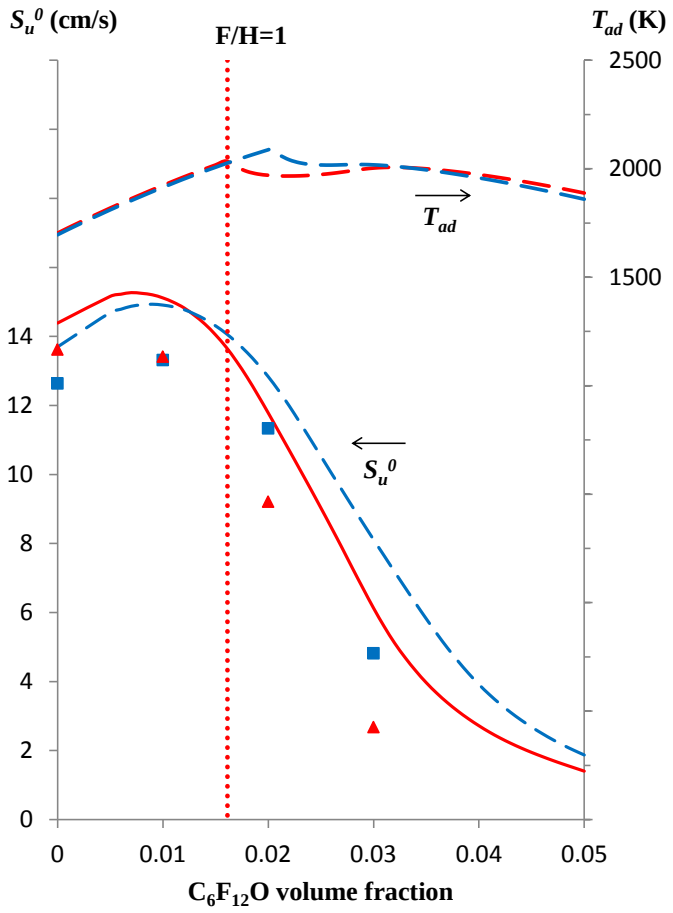

Figure 0.5: Burning velocities (lower curves, left axis) and equilibrium adiabatic flame temperatures (top curves, right axis) for C_3H_8-air at Φ=0.8 in dry and wet air as a function of added $C_6F_{12}O$ concentration.

7.3 Conclusions

$C_6F_{12}O$ is a clean fire suppressant that has replaced Halon 1211 in many total flooding applications and may have potential to replace Halon 1301 in a number of the remaining critical-use applications. The inhibition effectiveness of $C_6F_{12}O$ has been analyzed in typical experiments used to gauge efficacy (e.g. cup burner tests), but its performance in premixed hydrocarbon-air systems has not been well established. In addition, a kinetic model describing the decomposition of $C_6F_{12}O$ in hydrocarbon-air

systems was developed but has yet to be tested against experimental data. Thus, unstretched laminar burning velocities were determined from spherical expanding flames and extrapolation to zero-stretch conditions using non-linear methods. Burning velocities were measured for CH_4-air and C_3H_8-air flames over a range of equivalence ratios with $C_6F_{12}O$ added up to a concentration X_a=0.03. Tests were performed at 296 K and 1 atm, and in some cases, the relative humidity of the air was varied.

The inhibition effectiveness of $C_6F_{12}O$ was studied when added to premixed hydrocarbon-air flames by examining the impact on burning velocity. Equilibrium adiabatic flame temperature calculations complemented the burning velocity measurements and provided additional insight regarding the inhibition mechanism of $C_6F_{12}O$. By comparing the burning velocity of hydrocarbon-air flames inhibited with $C_6F_{12}O$ and CF_3Br, the conditions for which $C_6F_{12}O$ work as a CF_3Br replacement have been highlighted. In addition, the present results are consistent with the FAA-ACT results, in which added $C_6F_{12}O$ to the lean system enhanced the heat release and reactivity. $C_6F_{12}O$ provided greater reduction in burning velocity (compared to CF_3Br) when added to rich flames, whereas CF_3Br provided greater reduction when added to lean flames.

Measured burning velocities were compared to model predictions using the newly assembled kinetic mechanism for $C_6F_{12}O$ decomposition. Considering the small number of reaction pathways considered in the mechanism, the model predicted burning velocities that were in good agreement with the measurements. Predictions were better when adding $C_6F_{12}O$ to CH_4-air flames as opposed to C_3H_8-air flames. Improvements to

the model may be necessary to eliminate the discrepancy between predictions and measurements when adding higher concentrations of $C_6F_{12}O$ to lean C3H-air flames.

Experiments and calculations were performed to explore the influence of water vapor on the inhibition effectiveness of $C_6F_{12}O$. For lean C_3H_8-air (Φ=0.8) with added $C_6F_{12}O$, water vapor in the oxidizer both suppressed and enhanced the burning velocity depending on the ratio of fluorine to hydrogen present in the system. When there was less fluorine than hydrogen ([F]/[H]<1) the added water vapor acts as a diluent. When the system contains more fluorine than hydrogen (i.e., at higher $C_6F_{12}O$ concentrations), the water vapor is no longer inert and reacts with fluorine to form HF and OH. The formation of additional OH through reaction with water is primarily responsible for the enhanced burning velocities as at higher $C_6F_{12}O$ concentrations as the presence of water has minimal influence on the flame temperature (and hence the chain-branching reaction $H+O_2=OH+O$).

Chapter 8: Summary and Recommendations

8.1 Summary

Apparent combustion enhancement by proposed halon replacement fire suppressants (for use in aircraft cargo bays) has been observed in full-scale, constant-volume tests at the FAA. The present study was motivated by the unsatisfactory performance of the proposed replacements and was performed to:

1. Test the concepts previously developed via numerical simulations and analysis of the FAA tests.
2. Reproduce the phenomena observed in the complex full-scale FAA experiments in controlled, well characterized small-scale tests.
3. Explore laboratory-scale experiments as a screening tool for cargo bay halon replacements
4. Examine the performance of potential replacements that were not tested by the FAA.
5. Provide preliminary validation of recently developed and updated kinetic mechanisms.

To accomplish the outlined objectives, small-scale experimental capabilities were first developed and documented. A 1.85 L spherical chamber was instrumented with measurement devices; an experimental procedure was developed; a LabVIEW VI was created to operate the experiment; and data reduction techniques were implemented and automated using Matlab. All facets of the experimental development were based on previous work detailed in literature. The experiment was capable of providing

flammability limits, explosion pressure (constant-volume), and rate of pressure rise; further processing of the latter was used to obtain the laminar burning velocity using the constant-volume method outlined in Chapter 3. The experiment was then validated against burning velocities of frequently studied hydrocarbon fuels in air. Measurement uncertainty was estimated by considering how the perturbations in the measured variables influenced the output variables.

The constant-pressure method for determining unstretched laminar burning velocities was also reproduced. A 30 L spherical chamber with optical access was instrumented with pressure and temperature sensors and a high speed shadowgraph system to film flame propagation. A LabVIEW VI was creased to operate the experiment and post-processing techniques were developed to track the flame edge, reduce the data, and extrapolate the data to zero-stretch conditions using linear and non-linear methods described in literature. As done for the 1.85 L experiment, the experimental facility and post-processing procedures were validated by comparing hydrocarbon-air burning velocities to data in literature. Measurement uncertainty was estimated using the root-sum-of-squares method and by examining the repeatability of a tests.

In order to explore the overpressure phenomena observed in the full-scale FAA tests, experiments were performed in the 1.85 L chamber. The maximum explosion pressure and burning velocity were measured for CH_4-air flames with added CF_3Br (Halon 1301), $C_6F_{12}O$ (Novec 1230), $C_3H_2F_3Br$ (2-BTP), and C_2HF_5 (HFC-125) and reported in Chapter 4. The explosion pressure, for initially stoichiometric flames, was increased mildly (up to 11% and 6%) with $C_6F_{12}O$ and C_2HF_5 added at low concentrations, while at lean conditions (Φ=0.6), it was increased about 50% for added

$C_6F_{12}O$, $C_3H_2F_3Br$, or C_2HF_5, at agent volume fractions X_a=0.02, 0.03, and 0.06. The burning velocity for initially stoichiometric flames was always decreased with addition of any of the agents, whereas, for the lean conditions, it increased with added $C_6F_{12}O$ or C_2HF_5 (32% and 14%, at X_a=0.01 and 0.03). Burning velocities at higher initial pressure (3 bar) and temperature (400 K) showed lower inhibition effectiveness (than at ambient conditions) for the stoichiometric flames, and larger enhancement for the lean flames (and the effect was due primarily to the temperature increase). CF_3Br did not increase the explosion pressure or burning velocity for any of the tested conditions. Equilibrium calculations were used to interpret the experiments. The present work is consistent with the FAA results and previous analysis of the full-scale tests.

In Chapter 5, the inhibition effectiveness of $C_2HF_3Cl_2$ (a potential alternative not considered in the FAA tests) was examined by measuring the laminar burning velocities of CH_4-air flames with added $C_2HF_3Cl_2$ in the 1.85 L chamber, with experiments performed over a range of inhibitor concentration and fuel-air equivalence ratio Φ. Burning velocities at ambient (T=298 K; P=1.01 bar) and elevated (T=400 K; P=3 bar) conditions were compared to numerical predictions obtained using a newly-developed kinetic mechanism describing the decomposition of hydrochlorofluorocarbons (HCFCs) in hydrocarbon-air systems. Excellent agreement was demonstrated, considering the model was not adjusted and the present study was the first to test the mechanism against experimental data of a two-carbon HCFC. In addition to providing model validation, the effectiveness of $C_2HF_3Cl_2$ was compared to the analogous HFC compound C_2HF_5 to explore the advantages of Cl substitution for F. Experimental measurements of agent influence on burning velocity and numerical modeling of premixed flame structures

demonstrated that $C_2F_3Cl_2H$ is a more effective flame inhibitor than C_2F_5H, particularly for very lean CH_4-air mixtures. Reaction pathway and sensitivity were analyzed to interpret the differences in the inhibition mechanisms of C_2F_5H and $C_2HF_3Cl_2$ and to prioritize elementary reactions for further study.

Reported in Chapter 6 are the first experimental stretch-corrected burning velocities and Markstein lengths of premixed hydrocarbon-air flames inhibited with $C_3H_2F_3Br$ (2-BTP), in addition to data on flames inhibited by CF_3Br. Spherically expanding flame experiments were performed for inhibited CH_4-air and C_3H_8-air flames with a range of fuel-air equivalence ratios. Comparisons of the experimental data highlighted the conditions for which each inhibitor exhibited superior performance. $C_3H_2F_3Br$ performed better when added to rich flames, similar performance was observed for stoichiometric flames, and CF_3Br performed better when added to lean flames. In addition, the experimental burning velocities provided the first validation of newly developed and updated kinetic mechanisms for the decomposition of brominated compounds in hydrocarbon-air systems. Predictions with the updated CF_3Br mechanism were in excellent agreement with the experiments over the full range of fuel-air equivalence ratios considered. Agreement between predictions with the 2-BTP mechanism and measurements was less satisfactory, although still good considering the model is new and untested. The influence of inhibitors on the flame response to stretch and susceptibility to instabilities was examined through consideration of the measured burned gas Markstein lengths. Stretch interactions were found to be responsible for non-ignition occurring over a range of predicted burning velocities (~7.5-2.5 cm/s). Moreover, the influence of inhibitor on flame stability was dependent on several factors,

including the inhibitor type, fuel type, and fuel-air equivalence ratio, and inhibitor concentration. Stabilization and destabilization were both observed when adding either CF_3Br or $C_3H_2F_3Br$. Lastly, a sensitivity analysis highlighted the brominated reactions for which changes in the rate coefficients most strongly influence the predicted burning velocities.

In Chapter 7 are the first reported experimental stretch-corrected burning velocities of CH_4-air and C_3H_8-air flames inhibited by $C_6F_{12}O$ (Novec 1230). In addition, it is the first to *experimentally* show the presence of water vapor to increase the burning velocity of halogenated flames. Spherically expanding flames were recorded via high-speed shadowgraphy and the raw data was extrapolated to zero-stretch conditions using a non-linear method. Burning velocities of premixed CH_4-air and C_3H_8-air flames inhibited by $C_6F_{12}O$ are reported and compared to similar flames inhibited with CF_3Br and to numerical predictions with a kinetic model that has yet to be tested. Burning velocities were measured for inhibited flames with a range of fuel-air equivalence ratios and with $C_6F_{12}O$ added up to 3% by volume. When comparing the inhibition effectiveness of $C_6F_{12}O$ to that of CF_3Br, $C_6F_{12}O$ provided greater reduction in the adiabatic flame temperature of the rich flame, but CF_3Br provided greater reduction in the burning velocity. At lean conditions, $C_6F_{12}O$ increased the adiabatic flame temperature and was far less effective than CF_3Br at reducing the burning velocity. In terms of model validation, burning velocity measurements were in excellent agreement with predictions for most cases; with the exception for C_3H_8-air at Φ=0.8 X_a=0.03 and Φ=0.6 X_a=0.03 where the model under-predicted performance by ~ 3.5 cm/s. Furthermore, tests were performed to examine the influence of water vapor on the burning velocity of a C_3H_8-air.

For $C_6F_{12}O$ concentrations resulting in a halogen to hydrogen ratio greater than unity, the presence of water vapor increased the burning velocity of a lean C_3H_8-air inhibited with $C_6F_{12}O$ by as much as 23% (2.1 cm/s).

8.2 Recommendations for Future Work

Experimental improvements include further automation of the test procedure. Currently, about 75% of the time required to run a test is spent purging the chamber (of the product gases from the previous test) and preparing the reactant mixture. To thoroughly remove the product gases, the chamber must be repeatedly purged with air and subject to vacuum. Moreover, mixture preparation involves the tedious task of opening and closing valves until the desired amount of each successively added reactant is achieved (determined using the method of partial pressures).

Automation of the two procedures could be accomplished by incorporating additional solenoid valves, a switch to control the vacuum pump, and an additional input signal to the data acquisition system that provides the chamber pressure during mixing. The bulk of the work required for automation will involve updating the LabVIEW VIs. Chamber purging with require new output signals to open/close valves and to turn on/off the vacuum pump at specified time intervals. Mixture preparation will require a more sophisticated algorithm that can open a valve to add a reactant, check the resulting chamber pressure, then add more reactant until the desired partial pressure (i.e., volume fraction) is met. The algorithm will need to be iterative as the chamber pressure settles slightly each time after a reactant is added. The gas handling system may also require upgrades so that the VI can control the gas that is introduced through the inlet valve

(there is one inlet valve with a five-way valve upstream that sets the reactant to be added). In addition, a syringe pump will need to be incorporated to automate injection liquid reactant injection.

In regards to numerical work, spherically propagating flame predictions would be of great value. In the present work, only 1-D planar flame simulations were performed and compared to unstretched burning velocities extrapolated from the experimental data. Currently, only a select number of analytical relationships describing the flame response to stretch are available in literature, and each was derived with a unique set of assumptions. Thus, considerable extrapolation uncertainty exists for certain reactant mixtures with Lewis numbers far from unity. As discussed in refs. [37, 45], modeling stretched spherically propagating flames eliminates the extrapolation uncertainty, enabling improved kinetic model validation. In addition, direct comparison eliminates inaccuracies from error in the expansion ratio calculation (ratio of unburned and burned gas densities), which can be effected by radiation. In order to model spherically propagating flames, a code such as COSILAB (other non-commercial codes exist) must be acquired and some level of familiarity by the user must be established. The flame radius as a function of time can then be directly compared to visual imaging captured in the 30 L chamber to provide improved validation using the existing experimental data.

As far as new experimental conditions to consider, additional inhibitors should be tested to aid in the selection of agents to use in the next round of FAA tests. Blends of chemically active/passive suppressants should be considered. More experiments could be performed to understand how the relative humidity of air influences the inhibition performance of different halogenated compounds. Elevated temperatures and pressures

could be varied to explore performance under different conditions representative of other potential fire scenarios.

Bibliography

1. *The Montreal Protocol on Substances that Deplete the Ozone Layer as Adjusted and/or Amended in Loundon 1990, Copenhagen 1992, Vienna 1995, Montreal 1997, Beijing 1999*, UNEP, Editor.
2. *Revised Guidance Notes for Ozone Depleting Substances, Halon Phase-Out.*, E.P. Agency, Editor. 2008: United States.
3. J. Reinhardt, D. Blake, and T. Marker, *Development of a Minimum Performance Standard for Aircraft Cargo Compartment Gaseous Fire Suppression Systems*, FAA, Editor. 2000.
4. J. Reinhardt.*International Aircraft Systems Fire Protection Working Group, Federal Avaition Administration*. 2006
5. J. Reinhardt, *Behavior of Bromotrifuoropropene and Pentafluoroethane When Subjected to a Simulated Aerosol Can Explosion*, FAA, Editor. 2004.
6. M.L. Robin, Proc. Safety Prog. 19 (2000) 107-111.
7. G.T. Linteris, J.A. Manion, and D.R. Burgess, *Understanding unwanted combustion enhancement by potential halon replacements*. 2010, National Institute of Standards and Technology.
8. G. Linteris, F. Takahashi, V. Katta, H. Chelliah, and O. Meier.*IAFSS*. 2011
9. G.T. Linteris, D.R. Burgess, F. Takahashi, V.R. Katta, H.K. Chelliah, and O. Meier, Combust. Flame 159 (2012) 1016-1025.
10. G.T. Linteris, V.I. Babushok, P.B. Sunderland, F. Takahashi, V.R. Katta, and O. Meier, Proc. Combust. Inst. 34 (2013) 2683-2690.
11. V.I. Babushok, G.T. Linteris, and O.C. Meier, Combust. Flame 159 (2012) 3569-3575.
12. F. Takahashi, V.R. Katta, G.T. Linteris, and O.C. Meier, Proc. Combust. Inst. 34 (2013) 2707-2717.
13. F. Takahashi, V.R. Katta, G.T. Linteris, V. Babushok, and P.T. Baker, Proc. Combust. Inst. (2014)
14. F.H. Garner, R. Long, J. Graham, and A. Badakhshan, Proc. Combust. Inst. 6 (1957) 802-806.
15. W.A. Rosser, H. Wise, and J. Miller, Proc. Combust. Inst. 7 (1958) 175-182.
16. A. Levy, J.W. Droege, J.J. Tighe, and J.F. Foster, Proc. Combust. Inst. 8 (1961) 524-533.
17. M.J. Day, D.V. Stamp, K. Thompson, and G. Dixon-Lewis, Proc. Combust. Inst. 13 (1971) 705-712.
18. G. Dixon-Lewis and R.J. Simpson, Proc. Combust. Inst. 16 (1977) 1111-1119.
19. J.C. Biordi, C.P. Lazzara, and J.F. Papp, Proc. Combust. Inst. 14 (1973) 367-381.
20. J.C. Biordi, C.P. Lazzara, and J.F. Papp, Proc. Combust. Inst. 15 (1975) 917-932.
21. J.C. Biordi, C.P. Lazzara, and J.F. Papp, J of Phys. Chem. 81 (1977) 1139-1145.
22. J.C. Biordi, C.P. Lazzara, and J.F. Papp, J of Phys. Chem. 82 (1978) 125-132.
23. C.K. Westbrook, Combust. Sci. Technol. 23 (1980) 191-202.
24. C.K. Westbrook, Nineteenth Symposium on Combustion (1982) 127-141.

25. R.E. Tapscott and J.D. Mather, Journal of Fluorine Chemistry 101 (2000) 209-213.
26. D. Burgess, M. Zachariah, and P. Westmoreland, Prog. in Energy and Combust. Sci. 21 (1996) 453-529.
27. D. Burgess, M.R. Zachariah, W. Tsang, and P.R. Westmoreland, *Thermochemical and Chemical Kinetic Data for Fluorinated Hydrocarbons*, in *NIST Technical Note 1412*. 1995, National Institute of Standards and Technology.
28. G.T. Linteris and L. Truett, Combust. Flame 105 (1996) 15-27.
29. G.T. Linteris, D.R. Burgess, V. Babushok, M. Zachariah, W. Tsang, and P. Westmoreland, Combust. Flame 113 (1998) 164-180.
30. Y. Saso, D.L. Zhu, H. Wang, C.K. Law, and N. Saito, Combust. Flame 114 (1998) 457-468.
31. D.M. L'Esperance, B.A. Williams, and J.W. Fleming, Combust. Flame 117 (1999) 709-731.
32. V. Babushok, T. Noto, D.R.F. Burgess, A. Hamins, and W. Tsang, Combust. Flame 107 (1996) 351-367.
33. T. Noto, V. Babushok, D.R. Burgess JR., A. Hamins, and W. Tsang, Twenty-Sixth Symposium on Combustion (1996) 1377-1383.
34. T. Noto, V. Babushok, A. Hamins, and W. Tsang, Combust. Flame 112 (1998) 147-160.
35. V. Babushok and W. Tsang, Combust. Flame 123 (2000) 488-506.
36. S.R. Turns, *An Introduction to Combustion*. Vol. 499. 1996, New York: McGraw-Hill.
37. F.N. Egolfopoulos, N. Hansen, Y. Ju, K. Kohse-Höinghaus, C.K. Law, and F. Qi, Progress in Energy and Combustion Science 43 (2014) 36-67.
38. G.E. Andrews and D. Bradley, Combust. Flame 18 (1972) 133-153.
39. C.J. Rallis and A.M. Garforth, Prog. in Energy and Combust. Sci. 6 (1980) 303-329.
40. C.K. Law, *Combustion physics*. 2006: Cambridge University Press.
41. C.K. Law and C.J. Sung, Prog. in Energy and Combust. Sci. 26 (2000) 459-505.
42. C.K. Law, Twenty-Second Symposium on Combustion (1988) 1381-1402.
43. M. Matalon, Combust. Sci. Technol. 31 (1983) 169-181.
44. J. Jayachandran, R. Zhao, and F.N. Egolfopoulos, Combustion and Flame 161 (2014) 2305-2316.
45. J. Jayachandran, A. Lefebvre, R. Zhao, F. Halter, E. Varea, B. Renou, and F.N. Egolfopoulos, Proceedings of the Combustion Institute (2014)
46. Z. Chen, M.P. Burke, and Y. Ju, Combust. Theory and Modelling 13 (2009) 343-364.
47. K. Takizawa, A. Takahashi, K. Tokuhashi, S. Kondo, and A. Sekiya, Combust. Flame 141 (2005) 298-307.
48. M. Metghalchi and J.C. Keck, Combust. Flame 38 (1980) 143-154.
49. R. Stone, A. Clarke, and P. Beckwith, Combust. Flame 114 (1998) 546-555.
50. T. Iijima and T. Takeno, Combust. Flame 65 (1986) 35-43.
51. J.E. Shephard, J.C. Krok, and J.J. Lee, *Spark Ignition Energy Measurements in Jet A*, in *Explos. Dyn. Lab. Rep. FM 99e7*. 1999, Calif. Inst. Tech.

52. I. Glassman, *Combustion*. 1997: Academic Press.
53. S.P. Marshall, S. Taylor, C.R. Stone, T.J. Davies, and R.F. Cracknell, Combust. Flame 158 (2011) 1920-1932.
54. K. Eisazadeh-Far, F. Parsinejad, H. Metghalchi, and J.C. Keck, Combust. Flame 157 (2010) 2211-2221.
55. B. Lewis and G. Von Elbe, Journal of Chemical Physics 2 (1934) 283-290.
56. B. Lewis and G. von Elbe, *Combustion, Flames, and Explosions of Gases*. 1961.
57. J. Manton, G. von Elbe, and B. Lewis, Proc. Combust. Inst. 4 (1953) 358-363.
58. M. Metghalchi and J.C. Keck, Combust. Flame 48 (1982) 191-210.
59. P.G. Hill and J. Hung, Combust. Sci. Technol. 60 (1988) 7-30.
60. A.E. Dahoe and L.P.H. de Goey, Journal of Loss Prevention in the Process Industries 16 (2003) 457-478.
61. A.S. Huzayyin, H.A. Moneib, M.S. Shehatta, and A.M.A. Attia, Fuel 87 (2008) 39-57.
62. K. Saeed and C.R. Stone, Combust. Theory and Modelling 8 (2004) 721-743.
63. F. Rahim, K. Eisazadeh-Far, F. Parsinejad, J. Andrews, and H. Metghalchi, International Journal of Thermodynamics 11 (2008) 151-160.
64. K. Eisazadeh-Far, A. Moghaddas, J. Al-Mulki, and H. Metghalchi, Proc. Combust. Inst. 33 (2011) 1021-1027.
65. A. Moghaddas, K. Eisazadeh-Far, and H. Metghalchi, Combust. Flame 159 (2012) 1437-1443.
66. G.P. Smith, D.M. Golden, M. Frenklach, N.W. Moriarty, B. Eiteneer, C. Mikhail Goldenberg, T. Bowman, R.K. Hanson, S. Song, J. William C. Gardiner, V.V. Lissianski, and Z. Qin. *http://www.me.berkeley.edu/gri_mech/*.
67. V.I. Babushok, D.R.F. Burgess, W. Tsang, and A.W. Miziolek, *in: Halon Replacements*. 1995.
68. Burcat, Alexander, and Ruscic, *Third millenium ideal gas and condensed phase thermochemical database for combustion with updates from active thermochemical tables*. 2005, Argonne, IL: Argonne National Laboratory.
69. S. Gordon and B.J. McBride, *Computer program for calculation of complex chemical equilibrium compositions and applications*, N.R.P. 1311, Editor. 1996, NASA Glenn Research Center: Cleveland, OH.
70. V.I. Babushok, G.T. Linteris, O.C. Meier, and J.L. Pagliaro, Combust. Sci. Technol. 186 (2014) 792-814.
71. V. Babushok, D.R. Burgess JR., G.T. Linteris, and O. Meier, Combust. Flame 162 (2015) 1104-1112.
72. Hopkinson, (1906)
73. K.H. O'Donovan and R.C. J., Combust. Flame 3 (1959) 201-214.
74. K. Saeed and C.R. Stone, Combust. Flame 139 (2004) 152-166.
75. C.C.M. Luijten, E. Doosje, J.A. van Oijen, and L.P.H. de Goey, International Journal of Thermal Sciences 48 (2009) 1206-1212.
76. M. Elia, M. Ulinski, and M. Metghalchi, Journal of Engineering for Gas Turbines and Power 123 (2001) 190.

77. A. Clarke, *Measurement of laminar burning velocity of air/fuel/diluent mixures in zero gravity*, in *University of Oxford. Mathematical and Physical Sciences Division*. 1994, University of Oxford.
78. W.C. Reynolds, *Stanjan: Chemical Equilibrium Solver* 1987, Mechanical Engineering Department, Stanford University: Stanford, CA.
79. C.C.M. Luijten, E. Doosje, and L.P.H. de Goey, International Journal of Thermal Sciences 48 (2009) 1213-1222.
80. F.A. Williams.*AGARD Conference Proceeding*. 1975
81. D. Razus, V. Brinzea, M. Mitu, C. Movileanu, and D. Oancea, Energy & Fuels 26 (2012) 901-909.
82. D.R. Dowdy, D.B. Smith, and S.C. Taylor, Twenty-Third Symposium on Combustion (1990) 325-332.
83. L.K. Tseng, M.A. Ismail, and G. Faeth, Combustion and Flame 95 (1993) 410-426.
84. U.J. Pfahl, M.C. Ross, and J.E. Shephard, Combust. Flame 123 (2000) 140-158.
85. B.N. Taylor and C.E. Kuyatt, *Guidelines for Evaluating and Expressing the Uncertainty of NIST Measurement Results*, N.I.o.S.a. Technology, Editor. 1994.
86. M.I. Hassan, K.T. Aung, and G.M. Faeth, Combust. Flame 112 (1998) 539-550.
87. G. Rozenchan, D.L. Zhu, C.K. Law, and S.D. Tse, Proc. Combust. Inst. 20 (2002) 1461-1469.
88. C.H. Osorio, A.J. Vissotski, E.L. Petersen, and M.S. Mannan, Combust. Flame 160 (2013) 1044-1059.
89. O. Park, P.S. Veloo, N. Liu, and F.N. Egolfopoulos, Proc. Combust. Inst. 33 (2011) 887-894.
90. C.M. Vagelopoulos and F.N. Egolfopoulos, Twenty-Seventh Symposium on Combustion (1998)
91. M.I. Hassan, K.T. Aung, O.C. Kwon, and G.M. Faeth, Journal of Propulsion and Power 14 (1998) 479-488.
92. G. Jomaas, X.L. Zheng, D.L. Zhu, and C.K. Law, Proc. Combust. Inst. 30 (2005) 193-200.
93. L.K. Tseng, M.A. Ismail, and G.M. Faeth, Combust. Flame 95 (1993) 410-426.
94. S. Kwon, L.K. Tseng, and G.M. Faeth, Combust. Flame 90 (1992) 230-246.
95. L. Qiao, C. Kim, and G. Faeth, Combust. Flame 143 (2005) 79-96.
96. T. Tahtouh, F. Halter, and C. Mounaïm-Rousselle, Combust. Flame 156 (2009) 1735-1743.
97. A.P. Kelley, G. Jomaas, and C.K. Law, Combust. Flame 156 (2009) 1006-1013.
98. G.S. Settles, *Schlieren and Shadowgraph Techniques: Visualizing Phenomena in Transparent Media.* 2001, Berlin: Springer.
99. L. Qiao, Y. Gu, W.J.A. Dahm, E.S. Oran, and G.M. Faeth, Proc. Combust. Inst. 31 (2007) 2701-2709.
100. L. Qiao, Y. Gan, T. Nishiie, W.J.A. Dahm, and E.S. Oran, Combust. Flame 157 (2010) 1446-1455.
101. H. Yu, W. Han, J. Santner, X. Gou, C.H. Sohn, Y. Ju, and Z. Chen, Combustion and Flame (2014)
102. Z. Chen, Combust. Flame 162 (2015) 2442-2453.

103. S.P. Fuss and A. Hamins, Journal of Heat Transfer 124 (2002) 26.
104. D. Bradley, P.H. Gaskell, and X.J. Gu, Combust. Flame 104 (1996) 176-198.
105. F. Halter, T. Tahtouh, and C. Mounaïm-Rousselle, Combust. Flame 157 (2010) 1825-1832.
106. Z. Chen, M.P. Burke, and Y. Ju, Proc. Combust. Inst. 32 (2009) 1253-1260.
107. G.H. Markstein, *Non-Steady Flame Propagation*. 1964, New York Pergamon.
108. P. Clavin, Prog. in Energy and Combust. Sci. 11 (1985) 1-59.
109. N. Bouvet, F. Halter, C. Chauveau, and Y. Yoon, International Journal of Hydrogen Energy 38 (2013) 5949-5960.
110. P.D. Ronney and G.I. Sivashinsky, J. Appl. Math. 49 (1989) 1029-1046.
111. A.P. Kelley, J.K. Bechtold, and C.K. Law, Journal of Fluid Mechanics 691 (2011) 26-51.
112. A.P. Kelley and C.K. Law, Combust. Flame 156 (2009) 1844-1851.
113. Z. Chen, Combust. Flame 158 (2011) 291-300.
114. F. Wu, W. Liang, Z. Chen, Y. Ju, and C.K. Law, Proceedings of the Combustion Institute 35 (2015) 663-670.
115. W. Lowry, J. de Vries, M. Krejci, E. Petersen, Z. Serinyel, W. Metcalfe, H. Curran, and G. Bourque, Journal of Engineering for Gas Turbines and Power 133 (2011) 091501.
116. X.J. Gu, M.Z. Haq, M. Lawes, and R. Woolley, Combust. Flame 121 (2000) 41-58.
117. H. Wang, X. You, A.V. Joshi, S.G. Davis, A. Laskin, F. Egolfopoulos, and C.K. Law. *USC Mech Version II. High -Temperature Combustion Reaction Model of H2/CO/C1-C4 Compounds*. 2007; Available from: http://ignis.usc.edu/USC_Mech_II.htm.
118. Z. Chen, Combust. Flame 157 (2010) 2267-2276.
119. F.N. Egolfopoulos, D.L. Zhu, and C.K. Law, Proc. Combust. Inst. 23 (1991) 471-478.
120. K.J. Bosschaart and L.P.H. de Goey, Combust. Flame 136 (2004) 261-269.
121. E. Varea, V. Modica, A. Vandel, and B. Renou, Combust. Flame 159 (2012) 577-590.
122. S. Balusamy, A. Cessou, and B. Lecordier, Experiments in Fluids 50 (2010) 1109-1121.
123. C. Tang, Z. Huang, C. Jin, J. He, J. Wang, X. Wang, and H. Miao, International Journal of Hydrogen Energy 33 (2008) 4906-4914.
124. E. Varea, *Experimental analysis of laminar spherically expanding flames*, in *Physics*. 2013, Institut National des Sciences Appliquees de Rouen.
125. C.J. Sun, C.J. Sung, L. He, and C.K. Law, Combust Flame 118 (1999) 108-128.
126. R.J. Kee, J.A. Miller, and T.H. Jefferson, *Report, 1980, SAND80-8003.*, S.N. Laboratories, Editor. 1980.
127. R.J. Kee, J. Wamatz, and J.A. Miller, *Report, 1983, SAND83-8209.*, S.N. Laboratories, Editor. 1983.
128. R.J. Kee, J.F. Grcar, M. Smooke, J. Miller, and E. Meeks, Sandia National Laboratories Report (1985)

129. Y. Xin, W. Liang, W. Liu, T. Lu, and C.K. Law, Combust. Flame 162 (2015) 68-74.
130. B.A. Williams, D.M. L'Esperance, and J.W. Fleming, Combust. Flame 120 (2000) 160-172.
131. J.C. Leylegian, D.L. Zhu, C.K. Law, and H. Wang, Combust. Flame 114 (1998) 285-293.
132. J.C. Leylegian, C.K. Law, and H. Wang, Proc. Combust. Inst. 27 (1998) 529-536.
133. H. Wang, T.O. Hahn, C.J. Sung, and C.K. Law, Combust. Flame 105 (1996) 291-307.
134. D.R. Burgess, V.I. Babushok, G.T. Linteris, and J.A. Manion, (2014)
135. G.T. Linteris, V.I. Babushok, D.R. Burgess, J.A. Manion, F. Takahashi, V. Katta, and P.T. Baker, Proc. Combust. Inst. 35 (2014)
136. Y.N. Shebeko, V.V. Azatyan, I.A. Bolodian, V.Y. Navzenya, S.N. Kopylov, D.Y. Shebeko, and E.D. Zamishevski, Combust. Flame 121 (2000) 542-547.
137. S. Kondo, K. Takizawa, A. Takahashi, K. Tokuhashi, and A. Sekiya, Fire Safety Journal 44 (2009) 192-197.
138. C.H. Kim, O.C. Kwon, and G.M. Faeth, Journal of Propulsion and Power 18 (2002) 1059-1067.
139. X. Ni and W.K. Chow, Applied Thermal Engineering 31 (2011) 3864-3870.
140. J. Grigg and A. Chattaway.*12th Proceedings of Halon Options Technical Working Conference (HOTWC)*. 2002.1-10.
141. Y. Zou, N. Vahdat, and M. Collins, Industrial & Engineering Chemistry Research 40 (2001) 4649-4653.
142. B.P. Carnazza, J.G. Owens, P.E. Rivers, and J.S. Schmeer.*Halon Options Technical Working Conferences (HOTWC)*. 2004
143. G. Lask and H.G. Wagner, Proc. Combust. Inst. 8 (1961) 432-438.
144. D. Razus, C. Movileanu, V. Brinzea, and D. Oancea, J Hazard Mater 135 (2006) 58-65.
145. K.L. Cashdollar, I.A. Zlochower, G.M. Green, R.A. Thomas, and M. Hertzberg, Journal of Loss Prevention in the Process Industries 13 (2000) 327-340.
146. G.F.P. Harris, Combust. Flame 11 (1967) 17-25.
147. H.C. Hottel and A.F. Sarofim, *Radiative Transfer*. 1967: McGraw-Hill.
148. S.S. Penner, Journal of Applied Physics 21 (1950) 685.
149. G.T. Linteris.*Halon Replacements*. 1995
150. G.T. Linteris, M.D. Rumminger, V. Babushok, and W. Tsang, Proc. Combust. Inst. 28 (2000) 2965-2972.
151. T.A. Moore, C.A. Weitz, and R.E. Tapscott.*Papers from 1991-2006 Halon Options Technical Working Conferences (HOTWC), CD-ROM, NIST SP 984-4*. 2001.551-564.
152. B.P. Carnazza, J.G. Owens, P.E. Rivers, and J.S. Schmeer.*Papers from 1991-2006 Halon Options Technical Working Conferences (HOTWC), CD-ROM, NIST SP 984-4*.
153. G.T. Linteris, M.D. Rumminger, V.I. Babushok, and W. Tsang, Proceedings of the Combustion Institute 28 (2000) 2965-2972.

154. V. Babushok, G.T. Linteris, D.R. Burgess Jr, and P.T. Baker, Combustion and Flame (2014) to be submitted.
155. G.T. Linteris.*International Aircraft Systems Fire Protection Working Group Meeting*. 2013
156. T.A. Moore, C.A. Weitz, and R.E. Tapscott.*Halon Options Technical Working Conference*. 1996.7-9.
157. A. Hamins, D. Trees, K. Seshardri, and H.K. Chelliah, Combust. Flame 99 (1994) 221-230.
158. W.L. Grosshandler, R.G. Gann, and W.M. Pitts, *Evaluation of alternative in-flight fire suppressants for full-scale testing in simulated aircraft engine nacelles and dry bays*, NIST, Editor. 1994.
159. G. Holmstedt, P. Andersson, and J. Andersson, Fire Safety Science - Proc. of the Fourth Int. Symp. (1994) 853-864.
160. F.N. Dacruz, J. Vandooren, and P. Vantiggelen, BULLETIN DES SOCIETES CHIMIQUES BELGES 97 (1988) 1011-1030.
161. R.G. Hynes, J.C. Mackie, and A.R. Masri, Combust. Flame 113 (1998) 554-565.
162. O. Sanogo, *Etude Experimentale et Modelization de la Structure de Flammes: Applications a la Recherche de Substitute aux Halons*. 1993, Orleans University.
163. C.H. Osorio, A. Morones, D. Plichta, E. Petersen, and S. Mannan.*8th U.S. National Combustion Meeting*. 2013
164. P.D. Ronney and H.Y. Wachman, Combust. Flame 62 (1985)
165. S. Wang, H. Zhang, J. Jarosinski, A. Gorczakowski, and J. Podfilipski, Combust. Flame 157 (2010) 667-675.
166. K. Takizawa, S. Takagi, K. Tokuhashi, S. Kondo, M. Mamiya, and H. Nagai, ASHRAE Transactions 119 (2013) 243-254.
167. C. Tanford and R.N. Pease, The Journal of Chemical Physics 15 (1947) 431-433.
168. C. Tanford and R.N. Pease, The Journal of Chemical Physics 15 (1947) 861-865.
169. D.J. Parks, N.J. Alvares, and D.G. Beason, Fire Safety Journal 2 (1980) 237-247.
170. N. Donato, C. Aul, E. Petersen, C. Zinner, H. Curran, and G. Bourque, J. Eng. Gas Turb. Power 132 (2010) 051502.
171. C.K. Westbrook, Combust. Sci. Technol. 34 (1983) 201-225.
172. A. Egerton and S. Thabet, Proceedings of the Royal Society of London. Series A. Mathematical and Physical Sciences 211 (1952) 445-471.
173. V.V. Zamashchikov, V.A. Alekseev, and A.A. Konnov, International Journal of Hydrogen Energy 39 (2014) 1874-1881.
174. C.K. Law and O.C. Kwon, International Journal of Hydrogen Energy 29 (2004) 867-879.
175. R. Sankaran and H.G. Im, Combust. Sci. Technol. 178 (2006) 1585-1611.
176. Z. Chen, International Journal of Hydrogen Energy 34 (2009) 6558-6567.
177. Z. Chen, M.P. Burke, and Y. Ju, Proc. Combust. Inst. 33 (2011) 1219-1226.
178. V.I. Babushok, G.T. Linteris, and P.T. Baker, Combustion and Flame 162 (2015) 2307-2310.
179. S. Kondo, K. Takizawa, and K. Tokuhashi, Journal of Fluorine Chemistry 144 (2012) 130-136.

180. S. Kondo, K. Takizawa, and K. Tokuhashi, Journal of Fluorine Chemistry 161 (2014) 29-33.
181. S. Kondo, Y. Urano, K. Takizawa, A. Takahashi, K. Tokuhashi, and A. Sekiya, Fire Safety Journal 41 (2006) 46-56.
182. O. Mathieu, C. Keesee, C. Gregoire, and E.L. Petersen, J Phys Chem A (2015)
183. J.L. Pagliaro, G.T. Linteris, P.B. Sunderland, and P.T. Baker, Combust. Flame 162 (2015) 41-49.